November 2016

Chasing New Physics: From Electroweak Baryogenesis to Dark Matter

Huaike Guo

Recommended Citation

Guo, Huaike, "Chasing New Physics: From Electroweak Baryogenesis to Dark Matter" (2016). *Doctoral Dissertations*. 837.
https://scholarworks.umass.edu/dissertations_2/837

CHASING NEW PHYSICS: FROM ELECTROWEAK BARYOGENESIS TO DARK MATTER

A Dissertation Presented

by

HUAIKE GUO

Submitted to the Graduate School of the
University of Massachusetts Amherst in partial fulfillment
of the requirements for the degree of

DOCTOR OF PHILOSOPHY

September 2016

Department of Physics

CHASING NEW PHYSICS: FROM ELECTROWEAK BARYOGENESIS TO DARK MATTER

A Dissertation Presented

by

HUAIKE GUO

Approved as to style and content by:

Michael J. Ramsey-Musolf, Chair

John Donoghue, Member

David Kawall, Member

Tom Braden, Member

Rory Miskimen, Department Chair
Department of Physics

DEDICATION

This thesis is dedicated to my family.

ACKNOWLEDGMENTS

I would like to express my sincere appreciation and gratitude to my advisor Professor Michael J. Ramsey-Musolf whom has been a great mentor for me during the past five years. I would like to thank you for being patient of explaining everything in detail for me, showing me the right way of doing physics and also for giving me great help when I was in trouble. I would also like to thank the committee members, professor John Donoghue, professor David Kawall and professor Tom Braden for being great members and for your valuable suggestions and corrections on my presentation and thesis. I also thank my collaborators and friends Sky Bauman, Wei Chao, Yu Du, Pei-Si Huang, Ying-Ying Li, Tao Liu, Hao-Lin Li, Grigory Ovanesyan, Tao Peng, Chien Yeah Seng, Fang Ye, Peter Winslow, John F. H. Shiu, Jing Shu, Jiang-Hao Yu. I have benefited a lot working and discussing with you all. I also want to thank the people in the physics department who gave me help and guide in the past few years, thanks to Jane Knapp, Ingrid Pollard, Alan McConkey and Joseph Babcock. Finally I specially thank my family for supporting me all the way from when I was young.

ABSTRACT

CHASING NEW PHYSICS: FROM ELECTROWEAK BARYOGENESIS TO DARK MATTER

SEPTEMBER 2016

HUAIKE GUO

B.S., SHANDONG NORMAL UNIVERSITY

M.S., PEKING UNIVERSITY

Ph.D., UNIVERSITY OF MASSACHUSETTS AMHERST

Directed by: Professor Michael J. Ramsey-Musolf

The origin of the baryon asymmetry in the universe and the nature of the dark matter remain mysteries and addressing these cosmological puzzles requires physics beyond the standard model. Electroweak baryogenesis remains a highly testable framework for explaining the baryon asymmetry and is employed in this work to study the capability of baryon generation for beyond standard model physics models and to explore new physics discovery potential in high energy and precision frontier. Weakly interacting massive particles as cold dark matter are also studied in this work featuring loop induced direct detection signals and novel nuclear responses within the recently developed non-relativistic effective field theory framework.

TABLE OF CONTENTS

Page

CHAPTER

LIST OF TABLES

LIST OF FIGURES

Figure **Page**

INTRODUCTION

The standard model(SM) of particle physics provides an unified theoretical framework for describing subatomic particles and their interactions. Its predictions are found overall agreement with experimental measurements in high energy and precision frontier and this framework is further solidified by the discovery [3, 78] of the last missing piece, the Higgs boson which is the key particle responsible for the spontaneous symmetry breaking of the theory to give mass to the other particles. The SM however is not perfect since it is infeasible to explain the observed cosmological baryon asymmetry in the universe and also does not provides a candidate for the dark matter.

Precise cosmological measurements have determined that about 84.5% of the universe matter content is dark matter while only 15.5% is attributed to ordinary baryonic matter [14] from a collective fit of parameters of the standard cosmological Lambda Cold Dark Matter model(ΛCDM) to various observations. On one hand, the origin of the predominance of baryonic matter over anti-matter is still mysterious from the SM point of view since particle and anti-particle are naturally symmetric in this framework. On the other hand, the incapability of the SM to incorporate the dark matter has triggered intensive theoretical efforts resorting to new physics for understanding the nature of the dark matter and numerous experimental searches directly or indirectly for the dark matter.

According to Sakharov [201], three conditions are required to generate a net baryon abundance, that is, baryon number violation, C and CP violation(CPV) and out of equilibrium conditions(assuming CPT conservation). All mechanisms of baryogenesis thus need to satisfy above three conditions. The mechanisms that work at

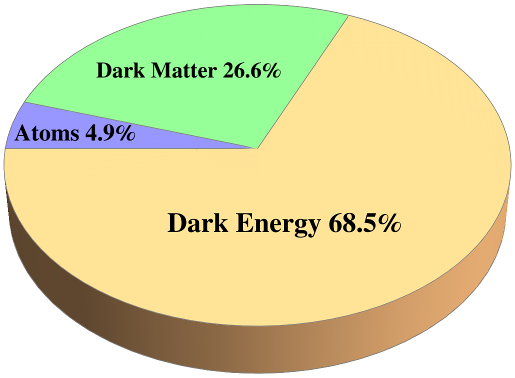

The energy budget of the universe. Plotted using the Planck 2015 results [14].

the grand unified theory scale at approximately 10^{16}GeV generally involve decays of some heavy particle which violates baryon number conservation. The Affleck-Dine mechanism [15, 104, 105] has its motivations in the supersymmetry theories. Also since a lepton asymmetry can be transferred into a baryon asymmetry through the electroweak Sphaleron process, a leptogenesis [124, 62] scenario can also serve as a baryogenesis scenario. Furthermore since the expansion of the universe actually violate time reversal invariance and thus CPT invariance, baryon asymmetry can be generated in equilibrium conditions which generally involve adding CP-violating interactions to the Lagrangian with the baryonic current coupled to a vector current. The most interesting mechanism is the electroweak baryogenesis(EWBG) [171, 207, 208] (See [192] for a recent review) in which the baryon asymmetry is generated duing duing the electroweak phase transition(EWPT) when the universe went through a first order phase transition from the electroweak symmetric phase to a phase where this symmetry is broken by a non-zero Higgs vev. This corresponds to approximately 100GeV and thus can be probed at current high energy collider laboratories. The following baryogenesis scenarios are set in this framework. In this picture the Higgs vacuum decay happens by nucleation of bubbles in the symmetric environment within which Higgs has a non zero vev. The bubbles expand, collide and merge with each other and when the phase transition is over, the universe is in the broken phase. In this picture, the turbulent bubble wall provides a non-equilibrium environment as required by the Sakharov condition. Even though the standard model(SM) does provide baryon number violation through weak Sphaleron interactions [182, 168], it falls short in the following aspects to generate the observed BAU: the magnitude of the CPV [127, 144, 128] is too tiny for BAU, the EWPT [54, 158] is a smooth cross over and not a first order EWPT for a 125GeV Higgs [6] from lattice simulations(See [192] for a catalog of these results) and thus physics beyond the SM is required with new sources of CPV and with strongly first order EWPT. The purpose of this work is partly dedicated to constructing and exploring new physics models which include these ingredients and within which the observed BAU can be generated.

Much effort has also been devoted to understanding the nature of dark matter and to interpreting its possible signals (See Ref. [209] for a review.). Among the various dark matter candidates that have been explored in the literature, the weakly interacting massive particle(WIMP) stands out as an highly interesting scenario. However the nature of dark matter and the way it interacts with the ordinary matter are still mysteries.

Dark matter is searched conventionally in two ways either directly by observing possible scintillations from the energy released when dark matter recoils off nucleus in deep underground detectors or indirectly by tracing annihilations products to dark matter through discovery of anomalous flux of cosmic rays such as anti-particles and gamma rays. Experimental searches are complimented by theoretical explorations of numerous dark matter models and by advances in more precise understanding of the dark matter nucleus interactions. The traditional direct detection limits are set assuming spin-independent(SI or Fermi) or spin-dependent(SD or Gamow-Teller) dark matter nucleon interactions. In very recent years, a systematic non-relativistic effective field theory(EFT) framework for describing dark matter nucleus interactions was developed [120, 24] following earlier work in Ref. [115]. This framework is based on the fact that the dark matter nucleus interaction picture is essentially non-relativistic and instead of working with relativistically covariant formalism a full set of non-relativistic operators is constructed in accordance with the underlying Galilean invariance. A detailed partial wave analysis enables the elastic scattering cross section of dark matter off finite-sized nucleus to be expressed as a factorized form with model dependent part encapsulated as coefficients of six model independent nuclear responses. These nuclear responses correspond to the previously adopted form factors for finite momentum transfer or finite-sized nucleus. Thus the various new physics model explorations is separated from the nuclear calculations of the universal nuclear responses with a theoretically well founded basis. This also drives current direct detection experimental searches and theoretical analysis to be interpreted on these full set of non-relativistic operators [203, 72, 26] rather than the previously used incomplete SI and SD interactions.

These new nuclear responses are generally involved when loop level dark matter quark interactions are considered such as when dark matter electric dipole moment(EDM), magnetic dipole moment(MDM), charge radius, axial charge radius, etc. contribute at leading order. Such loop induced dark matter quark interactions are gaining more attention [145, 141, 76] since they generally contribute less to direct detection cross sections in accordance with the currently null search results from direct detection measurements while still maintaining the right amount of relic abundance. In this work several models where these novel nuclear responses show up are explored and their phenomenological roles in this non-relativistic EFT framework are studied.

The following chapters are organized as follows. In chapter 1, an introduction to various aspects of the EWBG framework is given and the discussion of dark matter calculations is presented in chapter 2. Since most of the projects is set in the two Higgs doublet model, a brief discussion of it is given in 3. Pragmatic utilizations of above frameworks in calculations of BAU and dark matter properties follows. Specificially, a quark-flavored EWBG scenario set in the “b-s” quark sector is studied in chapter 4 and a lepton-flavored EWBG scenario set in the “$\mu - \tau$” is given in chapter 5. In chapter 6, a model with tau flavored dark matter is studied and in the following chapter 7, an analysis of a Higgs portal dark matter scenario set in the two Higgs doublet model is studied in detail.

CHAPTER 1

THE ELECTROWEAK BARYOGENESIS FRAMEWORK

In the framework of the Electroweak Baryogenesis(EWBG), the baryon asymmetry is generated duing the Electroweak phase transition(EWPT) at around $T = 100\text{GeV}$. Compared with other high scale mechanisms, EWBG remains an experimentally probable mechanism and can be tested at the energy frontier. In this chapter we first give a brief introduction and then review the various ingredients in this picture and finally show how the baryon asymmetry is calculated.

At high temperatures, the full electroweak symmetry $SU(2)_L \times U(1)_Y$ is manifest and as temperature drops when the universe expands, the universe went through a phase transition from this electroweak symmetric phase to the phase where the symmetry is broken to the subgroup $U(1)_{\text{EM}}$ by a non-zero Higgs vacuum expectation value(vev) as we feel today. This phase transition proceeds through the nucleation of electroweak bubbles of the broken phase within the environment where the electroweak symmetry is still unbroken(symmetric phase). This transition has to be first order to provide a non-equilibrium environment as required by the Sakharov conditions, otherwise all physical quantities will continuously transform as the temperature drops. The turbulent phase boundaries(bubble wall) provide this non-equilibrium environment within which the CP-violating interactions of particle scatterings will create a net chiral flux. This chiral flux is injected into the electroweak symmetric phase where the baryon number violating electroweak Sphaleron [183, 168] process convert this chiral asymmetry into a net baryon density which is then later captured by the expanding bubble wall. Inside the bubble wall, the Sphaleron process has to be suppressed to avoid the wiping out the captured baryon asymmetry.

In this picture, the diffusion of the chiral flux in front of the bubble wall provides an enhancement [98] of the efficiency for baryon generation compared with the earlier local EWBG mechanism where both the CP-violating process and the electroweak Sphaleron process have to be inside the narrow bubble wall thus significantly suppressing the baryon generation. Thus this mechanism is essentially non-local EWBG. Historically, the non-local EWBG further distinguishes two regimes. One regime is the thin wall case [152, 96, 97] where the particle can move across the bubble wall without significant scattering with the wall and thus is simpler to deal with. The other case is the thick wall regime [155, 98] where particle scatterings with the bubble wall have to be considered.

Furthermore it is discovered that the Non-Markovian nature of scattering(1998) using Closed Time Path(CTP) formulation of non-equilibrium Quantum Field Theory(QFT) is important [200](See Ref. [174] for a pedagogical description.). The observation is that transport properties in the plasma is non-Markovian, so one should use the CTP formalism to write down quantum Boltzmann equations(QBE) for particle densities in the plasma. These equations would involve integral over past time signifying its non-Markovian nature and this memory effect included by integrating over past history may lead to significant resonant enhancements of the sources. In this framework, the local and non-local, thin wall and thick wall are all unified in a systematic framework allowing for a more precise description of the baryon generation.

In the following, we will discuss various aspects entering above picture. We first introduce the non-trivial vacua structure of the electroweak theory and discuss details of the barrier between these adjacent vacua state, the electroweak Sphaleron. The following section explores the CPV invariants in the SM and the 2HDM. After that,

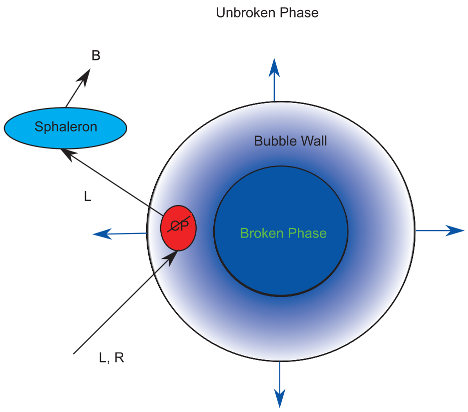

Figure 1.1: An illustrative picture of the baryon generation during the first order electroweak phase transition with a single electroweak bubble nucleated. The gradient of the blue color within the bubble wall represents a increasing Higgs vev from zero outside across the bubble wall into the bubble where the full finite temperature vev is developed. Note the generated B outside the bubble is later captured by the expanding bubble and kept inside the bubble. When all the space is turned into the broken phase, these generated B will become the baryon source for the nucleosynthesis.

the various aspects of the EWPT picture is discussed briefly including the details of the electroweak bubble, the rate of the baryon number violating process and the Sphaleron decoupling condition for the preservation of the generated baryons inside the bubbles. Finally in the last section, we illustrate how the baryon density is calculated within the CTP formalism.

1.1 Baryon Number Violation

1.1.1 The Anomalous Baryonic Current

Despite the conservation at the classical level, the $U(1)$ baryonic and leptonic currents are indeed violated in the SM by non-perturbative effects [212] due to anomalies of the theory. For n_f quark or lepton families, these anomalous fermionic currents are [216, 93]

$$\partial_\mu j_B^\mu = \partial_\mu j_l^\mu = n_f \left[\frac{g^2}{32\pi^2} W_{\mu\nu} \widetilde{W}^{a\mu\nu} - \frac{g'^2}{32\pi^2} F_{\mu\nu} \widetilde{F}^{\mu\nu} \right], \tag{1.1}$$

where $W^{a\mu\nu}$ and $F^{\mu\nu}$ are respectively the field strength tensor for the gauge fields associated with the local $SU(2)_L$ and $U(1)_Y$ symmetries. $\widetilde{W}^{a\mu\nu} \equiv \frac{1}{2}\epsilon^{\mu\nu\rho\sigma} W_{a\rho\sigma}$ and with similar definition for $\widetilde{F}^{\mu\nu}$. From this relation, we can see the change of the baryonic number as time evolves depends on the spatial integral over the r.h.s of above equation.

$$\begin{aligned} Q_B(t_f) - Q_B(t_i) &= \int_{t_i}^{t_f} dt \int d^3x \partial_t j_B^0, \\ &= \int_{t_i}^{t_f} \int d^3x \left[\vec{\nabla} \cdot \vec{j}_B + n_f \frac{g^2}{32\pi^2} W_{\mu\nu} \widetilde{W}^{a\mu\nu} \right], \end{aligned} \tag{1.2}$$

Since the $U(1)_Y$ field is not relevant [168], we neglected it in above expression. Furthermore $\vec{j}_B$ vanishes at spatial infinity and the first term on the r.h.s wont contribute. For the second part, the spatial integral over the gauge fields is actually a Chern-Simons number N_{CS} and if the initial and final gauge configurations are topologically distinct pure gauges, then their difference is an integer, that is,

$$\Delta Q_B = n_f [N_{CS}(t_f) - N_{CS}(t_i)], \tag{1.3}$$

where there are three color states for each generation with a total of $3 \times \frac{1}{3} \times n_f$ baryon number change for each unit of Chern-Simons number change. The reason why we have integer changes over integration of the gauge fields is rooted in the non-trivial topological structures of the electroweak theory from the requirement that the energy in Eucliden spacetime is finite.

1.1.2 The Degenerate Electroweak Vacua

The EW theory possesses degenerate vacua structures [149] and in this section we see how the EW vacua configurations are and introduce the Sphaleron later on. We start from the energy functional for static field configurations in the EW theory

$$E(\Phi, \vec{A}) = \int d^3\vec{x} \left[\frac{1}{4} F_{ij} F_{ij} + (D_i\Phi)^\dagger (D_i\Phi) + \lambda(\Phi^\dagger\Phi - \frac{v^2}{2})^2 \right], \tag{1.4}$$

and the vacua corresponds to $E(\Phi, \vec{A}) = 0$. Field configurations with finite energy need to satisfy $\Phi^\dagger\Phi = \frac{v^2}{2}$ at spatial infinity corresponding $|\vec{x}| \to \infty$. The trivial vacuum configuration we can immediate find is

$$\Phi = \begin{pmatrix} 0 \\ \frac{v}{\sqrt{2}} \end{pmatrix}, \quad A_i = 0, \tag{1.5}$$

and others can be obtained through a gauge transformation

$$\begin{aligned} \Phi' &= U\Phi, \\ A_i'^{\ a} t^a &= -ig^{-1}(\partial_i U)U^{-1}, \end{aligned} \tag{1.6}$$

where $U \in \mathrm{SU}(2)$ and can be parametrized following Manton [183] by

$$U(\theta, \phi, \mu) = \begin{pmatrix} (\cos\mu - i\sin\mu\cos\theta)e^{i\mu} & \sin\mu\sin\theta e^{i\varphi} \\ -\sin\mu\sin\theta e^{-i\varphi} & (\cos\mu + i\sin\mu\cos\theta)e^{-i\mu} \end{pmatrix}. \tag{1.7}$$

This is related to the standard parametrization of $SU(2)$ element by

$$U(\theta, \phi, \mu) = \begin{pmatrix} e^{i\frac{\mu}{2}} & 0 \\ 0 & e^{-i\frac{\mu}{2}} \end{pmatrix} \mathcal{U}\left[\vec{n}(\theta, -\phi - \frac{\pi}{2}), 2\mu\right] \begin{pmatrix} e^{i\frac{\mu}{2}} & 0 \\ 0 & e^{-i\frac{\mu}{2}} \end{pmatrix}, \tag{1.8}$$

where

$$\mathcal{U}(\vec{n}, w) = \exp(-i\frac{w}{2}\vec{n}\cdot\vec{\sigma}), \qquad 0 \le w \le 2\pi, \tag{1.9}$$

These pure gauge configurations have zero energy and furthermore these configurations can be classified according to the topological group they reside in which can

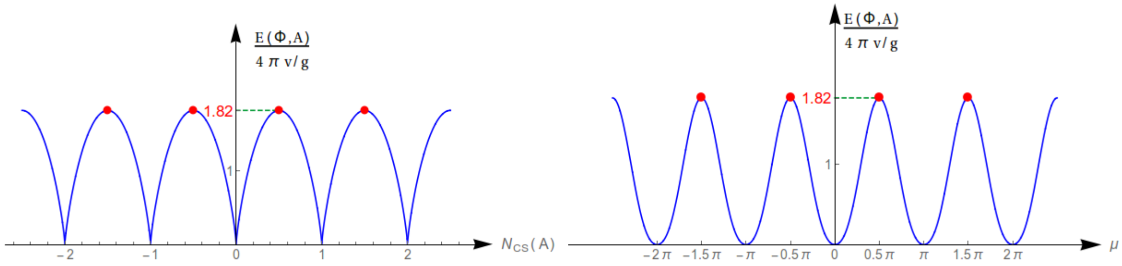

Figure 1.2: The Electroweak vacua periodic structure and the Electroweak Sphalerons from numerical calculations. The left plot is as a function of Chern-Simons number and the right plot as a function of μ. The lowest points with vanishing energy are the electroweak vacua and each highest red point in the barrier between two adjacent vacua corresponds to a Sphaleron solution. The energy value is normalized by $\frac{4\pi v}{g}$ and the numerical calculation uses the Higgs boson mass 125GeV as input to define the quartic coupling λ.

be characterized by the integer values of the Chern-Simons numbers. For generic such numbers, its relation with μ is $N_{\text{CS}} = \frac{2\mu - \sin(2\mu)}{2\pi}$ [214]. Note these integral values of topological charges can be generally expressed in terms of Cartan-Maurer integral invariants(See sec 23.4 in Ref. [216]). Thus these vacua states have a periodic structure as a function of the Chern-Simons number. This periodic structure of the EW vacua is shown in Fig. 1.2 as a function of Chern-Simons number(left) and as a function of μ(right) from numerically minimizing the energy functional for generic non-pure-gauge configurations as discussed later. The lowest points are the vacua states. Note that the left figure has a non-zero yet finite slope at each integer values of the Chern-Simons number while the right figure smoothly approach zero. This is in accordance with that in Ref. [214].

1.1.3 The Electroweak Sphalerons

The Electroweak Sphalerons correspond to the field configurations that have the minimum energy among those that sit at the top of the barrier in all the path connecting two neighboring vacua and thus they are saddle points of the energy functional and unstable. In fact, the word “Sphaleron” coined by N.S.Manton and F.R.Klinkhamer in their 1984 paper [168] is based on the Greek adjective “$\sigma\varphi\alpha\lambda\epsilon\rho os$” which means “ready to fall” signifying its unstable nature. In this section, we will review the calculations of Sphaleron profiles in the Electroweak theory following closely the discussions in the original papers [168, 182] and study its properties to be equipped for beyond SM Sphaleron studies.

The Higgs field at the spatial infinity which corresponds to a gauge rotation of the trivial vacuum and gives zero energy in Eq. 1.6 is written explicitly here as

$$\Phi^{\infty}(\theta,\varphi;\mu) = \frac{v}{\sqrt{2}}\begin{bmatrix} \sin\mu\sin\theta e^{i\varphi} \\ e^{-i\mu}(\cos\mu + i\sin\mu\cos\theta) \end{bmatrix},$$

To define the fields across $\mathcal{R}^3$, we follow the spherical symmetric ansatz,

$$\begin{aligned} \Phi(r,\theta,\varphi;\mu) &= (1-h(r))\begin{bmatrix} 0 \\ \frac{v}{\sqrt{2}}e^{-i\mu}\cos\mu \end{bmatrix} + h(r)\Phi^{\infty}(\theta,\varphi;\mu), \\ \vec{A}^a(\theta,\phi;\mu)t^a &= -if(r)g^{-1}(\vec{\nabla}U^{\infty})U^{\infty\ -1}, \end{aligned} \tag{1.10}$$

The energy of the Sphaleron as a function of the Higgs coupling λ/g^2 is spherically symmetric and is given by

$$\begin{aligned} E &= \frac{4\pi v}{g}\int_0^{\infty} d\xi\xi^2\Big\{\frac{4}{\xi^2}\left[(\frac{df}{d\xi})^2\sin^2\mu + \frac{2}{\xi^2}f^2(1-f)^2\sin^4\mu\right] \\ &\quad \frac{1}{2}(\frac{dh}{d\xi})^2\sin^2\mu + \frac{1}{\xi^2}\sin^2\mu\left[h^2(1-f)^2 - 2fh(1-f)(1-h)\cos^2\mu + f^2(1-h)^2\cos^2\mu\right] \\ &\quad +\frac{1}{4}\frac{\lambda}{g^2}(1-h^2)^2\sin^4\mu\Big\}, \end{aligned} \tag{1.11}$$

where the contributions in the first line comes from the gauge kinetic term, the second line from the Higgs kinetic term and the last line from the Higgs potential.

Note to easily derive above expression, one should use the spherical decomposition of the gauge fields. Also it should be remembered that above parametrization of the path from one vacuum to the adjacent one is not unique, a more generic spherical symmetric parametrization like the one in Ref. [21] wound involve more form factors like f, h here and change the energy slightly(see for example Ref. [214]) for field configurations except for that of the vacua and of the Sphaleron states whose energy is guaranteed to be unique by definition.

Finally the Sphaleorn profiles can be solved by minimizing the energy functional with respect to f and h for each fixed μ and we have

$$\begin{aligned}
\frac{d^2f}{d\xi^2} &= \frac{2}{\xi^2}f(1-f)(1-2f)\sin^2\mu \\
&\quad +\frac{1}{8}[2h^2(f-1)-2h(1-h)(1-2f)\cos^2\mu+2f(1-h)^2\cos^2\mu], \\
\frac{d}{d\xi}\left[\xi^2\frac{dh}{d\xi}\right] &= 2h(1-f)^2-2f(1-f)(1-2h)\cos^2\mu-2f^2(1-h)\cos^2\mu \\
&\quad +\frac{\lambda}{g^2}\xi^2h(h^2-1)\sin^2\mu, \qquad (1.12)
\end{aligned}$$

with here f and h subjected to the boundary conditions

$$\begin{aligned}
&f(0)=0, \qquad h(0)=0, \qquad f(\infty)=1, \qquad h(\infty)=1, \\
&f(0)=0, \qquad h(0)=0, \qquad f(\infty)=1, \qquad h(\infty)=1. \qquad (1.13)
\end{aligned}$$

Then the profiles f and h can be solved as a function of ξ for each μ from above two set of equations. It is not possible to seek exact anaytical solutions to these non-linear coupled equations and numerical method has to be used to precisely determine the profiles of f and h. In Fig. 1.3, we show the numerically solved f, h, $\frac{df}{d\xi}$ and $\frac{dh}{d\xi}$ profiles when $\frac{\lambda}{g^2}=0$. We can see all these four functions approach $\xi\to\infty$ with zero slope while at $\xi=0$, only f has a zero slope and h has a non-zero yet finite slope. The asymptotic behavior of these functions near either infinity or zero can be studied directly from Eq. 1.12.

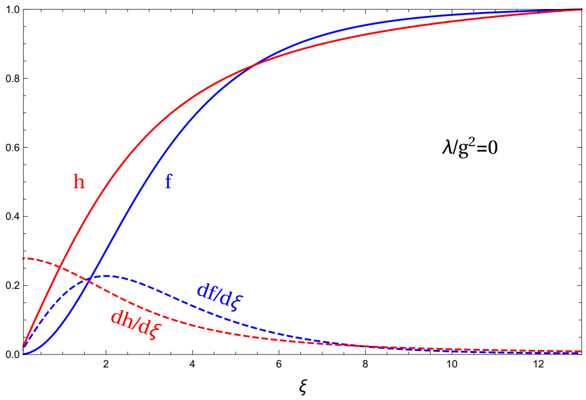

Figure 1.3: Numerically solved Sphaleron($\mu = \frac{\pi}{2}$) profiles of f, h and their derivatives as a function of the dimensionless quantity ξ. The Higgs quartic coupling is set to be zero in this plot.

In Fig. 1.4, we show more profiles of f and h as function of ξ for different choices of $\frac{\lambda}{g^2}$ in the range 0 to 1000. It is observed from this figure that for increased $\frac{\lambda}{g^2}$, f and h will both be larger with h having more notiable change of profiles.

With $f(\xi)$ and $h(\xi)$ solved, the energy of the Sphelerons can now be readily obtained from Eq. 1.11 and in Fig. 1.5 the energies as a function of $\frac{\lambda}{g^2}$ is shown. The Sphaleron energy curve as a function of the Higgs quartic coupling has a kink-type profile with small $\frac{\lambda}{g^2}$ approaching ≈ 1.6 asymptotically and with large $\frac{\lambda}{g^2}$ approaching ≈ 2.7. For a 125GeV SM Higgs, $\lambda = \frac{e^2 m_H^2}{8 m_W^2 s_W^2}$, we have $E \approx 1.82 \times \frac{4\pi v}{g} \approx 9$TeV.

Fixing the Higgs quartic coupling to be the one corresponding a 125GeV Higgs boson, we show the energies along the path $0 \leq \mu \leq \pi$ which connects two adjacent Electroweak vacua in Fig. 1.2. There the Sphalerons on top of the barrier is shown with a red dot and has energy 1.82 in unit $\frac{4\pi v}{g}$. Note that there are other [21] definitions of the path connecting the different vacua and the obtained energy profiles might differ slightly from the one shown in Fig. 1.5 but the value of the Sphaleron energies are all the same.

It should noted that the periodicity of the energy functional in Fig. 1.5 is an essential feature of the studies in solid state physics on material with Bravais lattice

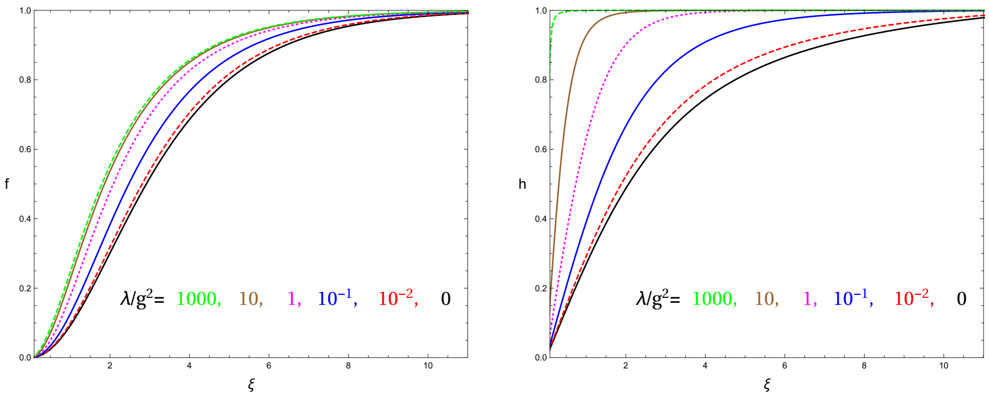

Figure 1.4: More Sphaleron($\mu = \frac{\pi}{2}$) profiles of f(left) and h(right) as functions of ξ for different choices $\frac{\lambda}{g^2}$ in the range from 0 to 1000 with 0(black solid), 10^{-2}(red dashed), 10^{-1}(blue solid), 1(pink dotted), 10(brown solid), 1000(green dashed).

structures. It is well known that the solution is Bloch waves if here the horizontal axis variable is replaced by spatial coordinates. This has motivated Ref. [214] to treat N_{CS} as a dynamical variable replacing the role of x in Schrodinger equations and found interesting properties of resulting Sphalerons. Following this analysis, Ref. [113, 113] studied the discovery prospect of the modified Sphalerons at colliders and in IceCube. This also trigged the study of band structures in Yang-Mills theories in Ref. [30].

1.2 CP-Violation

1.2.1 CPV in the SM and Jarlskog Invariant

In the SM, the only one CP violating complex phase comes from CKM matrix and the extra spurious phases of a general 3 × 3 unitary matrix are all removed by rephasing of quark fields. All CP violating physical observables should be invariant under rephasing of quark fields, that is , they should be able to expressed in terms of moduli of CKM matrix elements or quartets defined as

$$Q_{\alpha i\beta j} = V_{\alpha i}V_{\beta j}V^*_{\alpha j}V^*_{\beta i}. \tag{1.14}$$

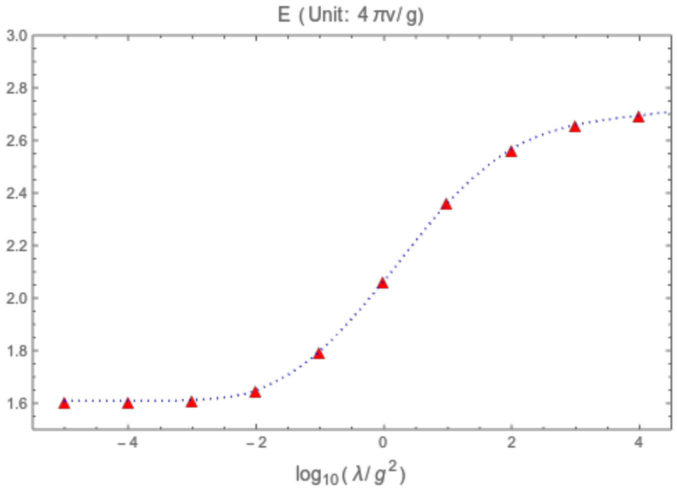

Figure 1.5: Sphaleron energy in unit of $\frac{4\pi v}{g}$ with $\frac{\lambda}{g^2}$ varying between a large range of values. The red triangle is the numerically calculated Sphaleron energy for discrete values of $\frac{\lambda}{g^2}$ and the dotted line is the corresponding fitted curve joining these discrete points.

All higher orders of CKM matrix elements could be expressed in terms of these moduli and quartets. Also, due to unitariry of CKM matrix, imaginary parts of all $Q_{\alpha i\beta j}$ are equal up to a sign difference. Thus we can use

$$J = \mathrm{Im} Q_{1122} \tag{1.15}$$

as the unique measure of CPV in the SM.

This term also follows from a more systematic way of considering rephasing invariants Suppose in SM, the Yukawa coupling matrices M_U, M_D are rotated to be Hermitian. (For example, start with physical mass matrix and rotate it with some unitary matrix. But this is not the basis transformation in our discussion. Generally, this will change gauge-kinetic terms of quarks.) Then the quantity $\det[M_U, M_D]$ is a more comprehensive way of characterizing presence or absence of CP violation [151, 111], since

$$\begin{aligned}
& \det[M_U, M_D] \\
= \;& \det[V^\dagger m_U V, m_D] \\
= \;& 2i\text{Im } \text{tr}(m_D^2 V^\dagger m_U V m_D V^\dagger m_U^2 V) \\
= \;& 2i(m_t - m_u)(m_t - m_c)(m_c - m_u)(m_b - m_d)(m_b - m_s)(m_s - m_d)J, \quad (1.16)
\end{aligned}$$

with here $m_{U/D}$ physical mass matrices. Then it follows that in order to have CPV in the SM, we need not only J to be non-vanishing but also non-zero and non-degenerate quark masses. However even though this determinant is rephasing invariant, it is not invariant under weak basis transformation.

Another way [60, 129] of getting this kind of relations is through considering general CP transformation properties of quark fields and invariance of SM under those transformations would give another measure of CP violation, $\text{tr}([H_U, H_D]^3)$ where $H_U \equiv M_U M_U^\dagger$ and also the same kind of definition for H_D.

$$\begin{aligned}
& \text{tr}([H_U, H_D]^3) \\
= \;& 6i\text{Im } \text{tr}(H_U^2 H_D^2 H_U H_D) \\
= \;& 6i\text{Im } \text{tr}(m_D^4 V^\dagger m_U^2 V m_D^2 V^\dagger m_U^4 V) \\
= \;& 6i(m_t^2 - m_u^2)(m_t^2 - m_c^2)(m_c^2 - m_u^2)(m_b^2 - m_d^2)(m_b^2 - m_s^2)(m_s^2 - m_d^2)J. (1.17)
\end{aligned}$$

Comparing this with the formulation in Eq. 1.16, we can see aside from the extra overall factor of 3 here, the only major difference is the quark masses in Eq. 1.16 are replaced by squares here. Actually the trace here can also be expressed in terms of a determinant as in Eq. 1.16 from the following identity for a generic $n \times n$ matrix A,

$$\det(A) = \sum_{k_1, k_2, \cdots, k_n} \prod_{l=1}^{n} \frac{(-1)^{k_l+1}}{l^{k_l} k_l!} \text{tr}(A^l)^{k_l}, \tag{1.18}$$

subject to constraint for the summation over k_l and l,

$$\sum_{l=1}^{n} l \cdot k_l = n. \tag{1.19}$$

For a 3 × 3 matrix as in the SM, this gives

$$\det(A) = \frac{1}{6}[(trA)^3 - 3tr(A)tr(A^2) + 2tr(A^3)]. \tag{1.20}$$

Here A is a commutator, so $tr(A) = 0$ and $\det(A) = \frac{1}{3}\mathrm{tr}(A^3)$, that is,

$$\mathrm{tr}([H_U, H_D]^3) = 3 \det([H_U, H_D]). \tag{1.21}$$

This relation can be used in organizing the expansion of the L.H.S of Eq. 1.16 into a form proportional to J which is quite easier than dealing with the products of six CKM matrix elements if one were to use the determinant.

From experimental measurements of the quark masses and the CKM matrix elements, we can readily evaluate the CPV invariant using a specific parametrization of the CKM matrix to have a sense of its magnitude. Since this invariant is of dimension 12, a dimensionless measure should be used at $T = 100\text{GeV}$ and this can be chosen as [93]

$$\frac{\mathrm{tr}([H_U, H_D])^3}{6i(100\text{GeV})^{12}} \approx 10^{-20}, \tag{1.22}$$

and it is generally argued on this basis that the CPV in the SM is too small to account for the observed baryon asymmetry.

1.2.2 CPV Invariants in 2HDM

In chapter 4 and chapter 5, we are going to exploit the relatively large CPV in the 2HDM to study whether or not it is possible to generate the BAU. More details of the 2HDM will be presented in chapter 3 to fix our conventions and here we focus on listing the set of CPV invariants in this model as a preparation for later studies. Even though in this study we only work with serveral CPV invariants, we list here a more complete set of such invariants from group theoretical considerations following existing studies in the references and use this chapter as a basis for future more thorough analysis of the CPV effects in the 2HDM.

In the 2HDM, there is now an extra symmetry, the $U(2)$ Higgs basis transformation and there are possibly many sources of CPV. Thus a clear identification and formulation of a Jarlskog-like invariant for CPV in 2HDM is highly important to sort out the different origins of the CPV in such invariant way for phenomenological analysis.

The procedure for finding such invariants in the 2HDM was introduced in Ref. [57] and here we give a review and summary of the invariants in the 2HDM even though the following chapters actually studied only one of the invariants. The basic procedures for finding these CPV invariants is to firstly list all the symmetries of the theory , identify the transformation properties of the fields and construct quantities that are invariant under these transformations by taking traces of the products. The imaginary part of such invariants can then serve as a proper invariant formulation of CPV.

1.2.2.1 Fermion and Higgs Basis Transformations

In this section we list the symmetries of the 2HDM and transformation properties of the fields and couplings. The Fermionic kinetic sector of the Lagrangian is defined with the convention

$$\mathscr{L}_{\text{Kinetic}} = \sum_{i=1}^{3} \left[\bar{Q_i}^{L} i\not{D} Q_i^L + \bar{U}_i^R i\not{D} U_i^R + \bar{D}_i^R i\not{D} D_i^R + \bar{E}_i^L i\not{D} E_i^L + \bar{e}_i^R i\not{D} e_i^R \right], \quad (1.23)$$

with here i, j being the quark and lepton family indices. The generic type III Yuakawa interactions are defined in its most generic way as

$$\mathscr{L}_{\text{Yukawa}} = -\overline{Q_L}\left[\sum_{j=1}^{2}\widetilde{\Phi_j}Y_j^U\right]U_R - \overline{Q_L}\left[\sum_{j=1}^{2}\Phi_j Y_j^D\right]D_R - \overline{E_L}\left[\sum_{j=1}^{2}\Phi_j Y_j^E\right]e_R + h.c, \tag{1.24}$$

For Higgs potential, it is convenient to work with the following notations to study basis transformation and invariants [57, 59],

$$\mathscr{L}_{\text{H}} = \sum_{a,b=1}^{2}\mu_{ab}\Phi_a^\dagger\Phi_b + \frac{1}{2}\sum_{a,b,c,d=1}^{2}\lambda_{ab,cd}(\Phi_a^\dagger\Phi_b)(\Phi_c^\dagger\Phi_d), \tag{1.25}$$

with $\lambda_{ab,cd} = \lambda_{cd,ab}$ and Hermiticity imposes the following conditions

$$\mu^\dagger = \mu, \quad \lambda_{ab,cd} = \lambda^*_{ba,dc}, \tag{1.26}$$

and vacuum minimization conditions lead to the following constraints,

$$\sum_a\left[\mu_{ab} + \frac{1}{2}\sum_{cd}\lambda_{ab,cd}v_c^* v_d\right]v_b = 0. \tag{1.27}$$

With now the definitions given for the kinetic, Yukawa and potential interactions, we can identify the following transformations that leaves the fermion and scalar kinetic interactions invariant,

- Flavor symmetries [101, 59]

$$U(3)_{Q_L}\otimes U(3)_{U_R}\otimes U(3)_{D_R}\otimes U(3)_{L_L}\otimes U(3)_{L_R} \tag{1.28}$$

  which leaves fermionic gauge-kinetic terms in Eq. 1.23 invariant. Explicitly, they are

$$\begin{aligned} U_R' &= D(U_R)U_R, \quad D_R' = D(D_R)D_R, \quad Q_L' = D(Q_L)Q_L, \\ e_R' &= D(e_R)e_R, \qquad E_L' = D(E_L)E_L. \end{aligned} \tag{1.29}$$

- Higgs basis transformation: $\Phi'_a = \sum_{b=1}^{2} U_{ab}\Phi_b$ which leaves Higgs gauge-kinetic terms invariant.

To make sure gauge-kinetic term does not change we assume all transformations above are *space time independent*. Above transformations are called basis transformations. The model parameters in the new basis will have a different form but they are related with the original parameters through

$$\begin{aligned} Y_a^{U\prime} &= D(Q_L)Y_b^U D^\dagger(U_R)U_{ab}, \\ Y_a^{D\prime} &= D(Q_L)Y_b^D D^\dagger(D_R)U^*_{ab}, \\ Y_a^{E\prime} &= D(E_L)Y_b^E D^\dagger(e_R)U^*_{ab}, \end{aligned} \tag{1.30}$$

for Yukawa couplings and for potential parameters,

$$\begin{aligned} \mu' &= U\mu U^\dagger, \\ \widetilde{V}' &= U\tilde{V}U^\dagger, \\ \lambda'_{ab,cd} &= U_{ae}U_{cg}U^*_{bf}U^*_{dh}\lambda_{ef,gh} \end{aligned} \tag{1.31}$$

with $\widetilde{V}_{ab} \equiv v_a v_b^*$ being a tensor under Higgs basis transformation [57]. The fermion indices associated with $Y_a^{U,D,E}$ and the Higgs basis indices of $\mu, \widetilde{V}$ are implicit in above writing.

If CP exsits, they should be independent on above choices of the basis for fermions and for the two Higgs doublets. Therefore they should exist through quantities which are invariant under above transoformations. The procedure of constructing such invariants is first construct invariants under fermion family transformations. The resulting quantites are tensors under Higgs basis transformations which needs to be combined in all possible ways to construct further Higgs basis invariants.

1.2.2.2 Fermion Family Invariants and Higgs Basis Tensor

Now we write down the quantites which are invairant under fermion family transofrmations but are tensors under Higgs basis transformation with the definition $Y_a^{\mathcal{D}} = Y_a^{D*}$, $Y_a^{\mathcal{E}} = Y_a^{E*}$ to make them have the same properties properties under Higgs basis transformtions

$$T_{ab}^{U} = \mathrm{tr}(Y_a^{U} Y_b^{U\dagger}), \qquad T_{ab}^{\mathcal{D}} = \mathrm{tr}(Y_a^{\mathcal{D}} Y_b^{\mathcal{D}\dagger}), \qquad T_{ab}^{\mathcal{E}} = \mathrm{tr}(Y_a^{\mathcal{E}} Y_b^{\mathcal{E}\dagger}), \tag{1.32}$$

where 'tr" acts on fermion family indices making $T_{ab}^{U,\mathcal{D},\mathcal{E}}$ invariant under the corresponding transformations while the subscripts "a,b" signify that they are still tensors under Higgs basis transformations,

$$T^{U\prime} = U T^{U} U^{\dagger}, \qquad T^{\mathcal{D}\prime} = U T^{\mathcal{D}} U^{\dagger}, \qquad T^{\mathcal{E}\prime} = U T^{\mathcal{E}} U^{\dagger}. \tag{1.33}$$

Now we can combine $T^{U,\mathcal{D},\mathcal{E}}, \mu, \tilde{V}, \lambda$ to make invariants also under Higgs basis transformations.

One thing to point out is that, aside from these basis transformations, there could also be rephasing of left and right handed quark fields equally to eliminate the unphysical phases in CKM matrix. But these could not be incorporated in above transformations because they act differently on upper and lower component of Q_L.

1.2.2.3 CP Invariant Yukawa Sector

The invariants that is nontrivial, simplest and involve Yukawa matrices are [57]

$$J_a = \mathrm{Im}\ \mathrm{tr}(\tilde{V} \mu T^{D}), \tag{1.34}$$

$$J_b = \mathrm{Im}\ \mathrm{tr}(\tilde{V} \mu T^{U}), \tag{1.35}$$

$$J_{\mathcal{E}} = \mathrm{Im}\ \mathrm{tr}(\tilde{V} \mu T^{\mathcal{E}}), \tag{1.36}$$

while quantities like Im tr$(A^n B^m)$ vanish for Hermitian A and B. Other kinds of invariants are at higher orders of $\tilde{V}, T, \mu$.

1.2.2.4 Explicit CPV in Potential

Theorem 1 of Ref. [139] states that the Higgs potential is explicitly CP conserving if and only if a basis exists in which all potential parameters are real. Otherwise, CP is explicitly violated. Theorem 2 [139] states that the necessary and sufficient conditions for explicitly CP-conserving 2HDM scalar potential is the simultaneous vanishing of the imaginary part of the four *I-invariants* (The name has been changed according the conventions here.),

$$I_{\mu 3\lambda} = \mathrm{Im}(\lambda^{(1)}_{ac}\lambda^{(1)}_{eb}\lambda_{becd}\mu_{da}), \tag{1.37}$$

$$I_{2\mu 2\lambda} = \mathrm{Im}(\mu_{ab}\mu_{cd}\lambda_{badf}\lambda^{(1)}_{fc}), \tag{1.38}$$

$$I_{6\lambda} = \mathrm{Im}(\lambda_{abcd}\lambda^{(1)}_{bf}\lambda^{(1)}_{dh}\lambda_{fajk}\lambda_{kjmn}\lambda_{nmhc}), \tag{1.39}$$

$$I_{3\mu 3\lambda} = \mathrm{Im}(\lambda_{acbd}\lambda_{cedg}\lambda_{ehfq}\mu_{ga}\mu_{hb}\mu_{qf}), \tag{1.40}$$

where $\lambda^{(1)}_{ad} = \sum_{b,c}\delta_{bc}\lambda_{ab,cd}$.

1.2.2.5 Spontaneous CPV from Complex Vacuum

The necessary and sufficient condition for the absence of spontaneous CPV from a complex Higgs vev was stated in Theorem 3 and Theorem 4 in Ref. [139] and corresponds to the vanishing of the *I-invariants* in Sec. 1.2.2.4 also the vanishing of the following three invariants.

$$J_1 = -2v^{-4}\widetilde{V}_{da}\mu_{ab}\lambda^{(1)}_{bd}, \tag{1.41}$$

$$J_2 = 4v^{-8}\widetilde{V}_{ab}\widetilde{V}_{dc}\mu_{be}\mu_{cf}\lambda_{eafd}, \tag{1.42}$$

$$J_3 = v^{-4}\widetilde{V}_{ab}\widetilde{V}_{dc}\lambda^{(1)}_{be}\lambda^{(1)}_{cf}\lambda_{eafd}, \tag{1.43}$$

or using the minimization conditions in Eq. 1.27,

$$J_1 = v^{-4}\widetilde{V}_{da}\widetilde{V}_{fe}\lambda^{(1)}_{bd}\lambda_{abef}, \tag{1.44}$$

$$J_2 = v^{-8}\widetilde{V}_{ab}\widetilde{V}_{dc}\widetilde{V}_{hg}\widetilde{V}_{rp}\lambda_{begh}\lambda_{cfpr}\lambda_{eafd}, \tag{1.45}$$

$J_{1,3}$ are also defined in Ref. [57] but with a different form,

$$J_1 = \mathrm{Im}(v_i^* v_j^* \mu_{i\alpha}\mu_{j\beta}\lambda_{\alpha k,\beta l}v_k v_l), \tag{1.46}$$

$$J_3 = \mathrm{Im}(v_i^* \mu_{ij}\lambda_{jk,kl}v_l), \tag{1.47}$$

we need to find the relation between these two sets of $J_{1,2}$.

For general 2HDM potential,

$$J_1 = \frac{1}{4}v^8 \mathrm{Im}(\bar{\lambda}_6^2\bar{\lambda}_5^*), \tag{1.48}$$

$$J_3 = -\frac{1}{2}v^4 \mathrm{Im}(\bar{\lambda}_6\bar{\lambda}_7^*), \tag{1.49}$$

where relations from minization conditions of potential

$$\bar{\mu}_{11} = -\frac{1}{2}\bar{\lambda}_1 v^2, \qquad \bar{\mu}_{12} = \frac{1}{2}\bar{\lambda}_6 v^2, \tag{1.50}$$

were used.

Note that above invariants are all non-zero for the most general type 2HDM with no restricted form and assumptions of the reality of its parameters. In each specific model of 2HDM, generally more simpler forms of the model will be defined and assumptions made to make most parameters real and in such cases, many of the above invariants will vanish.

1.3 Electroweak Phase Transition

Sometime in the early universe at $T \approx 100\text{GeV}$, there should be a phase transition from the electroweak symmetric phase to the broken phase from which all the particles in the SM obtain their mass. This EWPT provides one of the three Sakharov conditions that is the out-of-equilibrium condition for baryon asymmetry generation. The phase transition starts through formulation of broken phase bubbles in the environment of the symmetric phase. These bubbles expand and collide with each other leaving eventually the universe in the electroweak broken phase. To ensure that the generated baryon in the broken phase not to be wiped out, the Sphaleron process has to be suppressed in the broken phase. This requires the EWPT to be strongly first order and poses strong constraints on the potential.

In this section, a brief introduction of various concepts in this picture is discussed including a discussion of the finite temperature effective potential, an illustration of the dynamics of the bubble generation for calculating the nucleation temperature, nucleation rate, bubble wall profiles. Also the vacuum transition rate, also called the Sphaleron rate is reviewed briefly.

1.3.1 Electroweak Bubble Nucleation

Below the critical temperature T_c, the bubble of the true vacua will develop. The picture of this bubble formation is similar to that in inflation. In this picture, small bubbles are disfavored and only those larger bubble can furture expand. The minimal energy correspond to the critical bubble which is actually a spherically symmetric bounce solution minimizing the action

$$S_b(T) = \int d^3x \left[\frac{1}{2}(\vec{\nabla}\phi_b)^2 + V(\phi_b, T)\right] = 4\pi \int r^2 dr \left[\frac{1}{2}\left(\frac{d\phi_b(r)}{dr}\right)^2 + V(\phi_b, T)\right], \tag{1.51}$$

and thus can be solved from the following equation of motion,

$$\frac{d^2\phi_b}{dr^2} + \frac{2}{r}\frac{d\phi_b}{dr} - \frac{\partial V(\phi_b, T)}{\partial \phi_b} = 0. \tag{1.52}$$

with boundary conditions

$$\frac{d\phi_b}{dr}\bigg|_{r=0} = 0, \quad \phi_b\bigg|_{r\to\infty} = 0. \tag{1.53}$$

It is due to this type of boundary condition that its solution is called a bounce solution(See Ref. [216] for an introduction). If it is not for the boundary condition, we can see there are trivial solutions that satisfy the above equation, that is, when ϕ are constants taking values of the ϕ corresponding to the extremum of the potential. In particular the trivial solution $\phi = 0$ satisfies the above boundary condition but it is not the bounce solution. The bounce solution requires the value of ϕ at the origin to take the value of the field standing at the lower minimum of potential energy and thus the bounce solutions interpolate between those two minima of the potential. These two fields are topologically distinct from each other since one can not be deformed continuously to the other through due to the different fixed boundary values.

This equation is generally a nonlinear ordinary differential equation and numerical solutions are needed to get a precise solution. Since this bounce solution is important in many aspects of baryogenesis calculations, we briefly discuss how this kinds of ordinary differential equations can be solved numerically. By a trivial operation, this equation can be written as

$$\frac{d^2\phi_b}{dr^2} = \frac{\partial V(\phi_b, T)}{\partial \phi_b} - \frac{2}{r}\frac{d\phi_b}{dr}. \tag{1.54}$$

If we make the understanding that ϕ_b is position x and r as time, then the first term on the r.h.s represents a force from potential $-V(\phi)$ shown in Fig. 1.6 and the second term acts like a friction force. So the particle moves at $t = 0$ from the potential maximum at $\phi = \phi_2$ and reach $\phi = \phi_0$ at $t = \infty$. This forms the

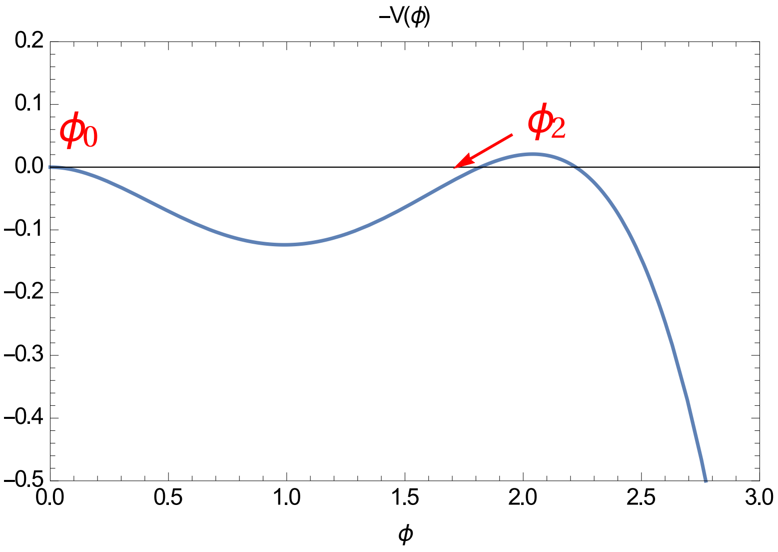

Figure 1.6: Illustrative understanding of the bounce solution of Eq. 1.52 as a particle rolls from one maximum to the lower one at origin under potential $-V(\phi)$.

basis of the undershooting-overshooting method as used in CosmoTransitions [**?**] and many other literatures. Note the relaxation method can also be used for this kind of problems [125, 126] as discussed in the appendix.

As a specific example, we consider the following simple scalar potential taken from Ref. [112],

$$V(\phi) = \frac{1}{2}\phi^2 - \frac{1}{2}\phi^3 + \frac{\alpha}{8}\phi^4, \qquad \alpha > 0. \tag{1.55}$$

For $\alpha < 1$, this potential has two minima $\phi_1 = 0$ and $\phi_2 = \frac{3}{2\alpha}[1 + \sqrt{1 - \frac{8}{9}\alpha}]$ and for $\alpha = 1$ these two are degenerate. The bounce solution has at its origin $\phi = \phi_2$ and at infinity $\phi = 0$. As $\alpha \to 1$ from below, the solution becomes more thin-walled. This can be seen from Fig. 1.7 where the solutions are obtained numerically using CosmoTransitions and agree very well with Fig.3 in Ref. [112]. The intercept with the vertical axis in this figure should correspond to the lower minimum ϕ_2 and these values have been tabulated in Table. 1.1 in the right column to be compared with the values direct calcualted from above formula given in the middle column. Note

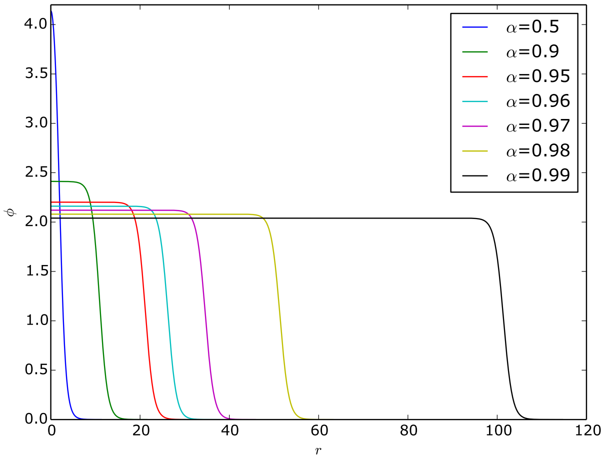

Figure 1.7: Numerically solved Bounce solutions corresponding to the topy model in Eq. 1.55.

that for thin-walled cases the agreement is very good while for the thick wall case like $\alpha = 0.5$, there is a noticeable difference between these two values. This discrepancy has also been observed in Fig.3 of Ref. [112].

It is worth to mention that the shape of the bounce solution looks like that of the Kink solution in one dimension of a scalar ϕ^4 theory [183]. They both interpolate two different minima of the potential but the two minima in the Kink solution originates from the degenerate vacua which have the same potential energy while the bounce solution describes a tunneling from the higher meta-stable minimum to the more stable lower minimum. Despite this, due the similarities of the two kinds of solutions, the Kink solutions are also used in the literature [123] as an approximation to describe the bubble profiles corresponding to the bounce solution which will be discussed in the next section.

Once solved, the bounce solutions provide important input for calculations in EWBG. These include finding out the nucleation temperature($T_{\rm nucl}$) as well as nucleation rate, determining the bubble wall profiles which are essential for baryogenesis calculations and they also can be used to study the gravitational waves generated

α	ϕ_2	Fig. 1.7
0.50	5.2360679775	4.13871154238
0.90	2.41202265917	2.41187160571
0.95	2.20169260875	2.20169259815
0.96	2.16089194235	2.16089194226
0.97	2.12038807864	2.12038807864
0.98	2.08011885787	2.08011885787
0.99	2.04001539623	2.04001539623

Table 1.1: The ϕ that gives the lower minimum in the toy model in Eq. 1.55 for different values of α approaching the ideal thin wall limit $\alpha = 1$. The middle column is the theoretical values directly calculated from the potential and the right column shows the corresponding values(the left end of lines in Fig. 1.7) from numerically solving the bounce solutions using CosmoTransitions.

from the bubble collision. In the remaining part of this section, we will discuss how T_{nucl} and the nucleation rate can be determined from the bounce solutions, the more detailed discussions of the bubble wall profiles will be discussed in the next section while a brief discussion of the calculations of gravitation waves will be deferred to a later section.

The nucleation rate per unit volume per unit time has the same form as the Sphaleron rate in Eq. 1.63,

$$\frac{\Gamma}{V} = I_0 T^4 \exp(-\frac{S_{\text{b}}}{T}). \tag{1.56}$$

The prefactor like the case of Sphaleron corresponds to integrating over the fluctuations around the bounce solution and are fluctuation determinants which need to be evaluated numerically. The exponential is just the action corresponding to the stationary point: the bounce solution and can be straightforwardly calculated once the bounce profile ϕ_b is solved. For bubbles expanding at the velocity v_w, the fraction of space that is still occupied by the symmetric phase is [189]

$$f_{\text{symmetric}} = \exp\left[-\int_{-\infty}^{t} \frac{4\pi}{3} v_w^3 (t-t')^3 I_0 T^4 e^{-S_b/T} dt'\right], \tag{1.57}$$

where both S_b and T are functions of t'. Accordingly the fraction of space corresponding to broken phase that is occupied by nucleated bubbles is $f_{\text{broken}} = 1 - f_{\text{symmetric}}$. The nucleation temperature is then defined by the condition that the integral in above exponential is 1, explicitly,

$$\int_{-\infty}^{t} \frac{4\pi}{3} v_w^3 (t-t')^3 I_0 T^4 e^{-S_b/T} dt' \equiv \Delta(t) = 1. \tag{1.58}$$

and the T_{nucl} can be determined implicitly by the following equation,

$$e^{S_b(T_{\text{nucl}})/T} = \frac{8\pi v_w^3 I_0}{(HTdS/dT)^4}, \tag{1.59}$$

The nucleation temperature solved this way will be changed through the release of latent heat and more details on corrections due to this effect as well as more detailed illustration of above discussions can be found in Ref. [189].

1.3.2 Electroweak Bubble Profiles

In this section, we will discuss more about the bounce solutions focusing on the aspect of wall profile determination. The profile of the Electroweak bubble is an important concept for the Baryon asymmetry calculations since this is where the CP-violating interactions generate left-handed charge asymmetries and thus the place where the CP-violating source terms that enter the Boltzmann equations are generated. Since there might be multiple scalar fields that couple to the gauge fields, there will then be correspondingly several coupled set of bounce solutions and we denote these solutions by $v_i(z)$. These solutions can be modeled roughly by the bubble-wall width(L_w), wall velocity(v_w) and ratios of the vevs such as $\beta(z)$ in 2HDM and supersymmetric theories both of which have two Higgs doublets. L_w and β can be determined right from above calculations of the bounce solutions as was done in MSSM [191] and in 2HDM [125, 126]. Rather than using a perturbative Higgs effective potential, these quantites have also been calculated on the lattice [100].

On the other hand, calculations of the wall vellcity v_w are more difficult and are missing in various studies on phenomenology in the literature. This needs a more detailed study of the dynamics and transport properties of the Higgs condensate in the plasma [188, 184]. Starting from the classical equation of motion of the Higgs background fields, the dynamics of the Higgs field can be derived

$$\Box\phi + V_T'(\phi) + \sum \frac{dm^2}{d\phi^2} \int \frac{d^3p}{(2\pi)^3 2E} \delta f(p, x) = 0, \tag{1.60}$$

where $V_T(\phi)$ is the finite temperature effective potential, m is the field dependent particle mass and $\delta f \equiv f - f_0$ characterizes the deviation from the equilibrium distribution f_0. The main difficulty lies in determining δf which should be solved from the Boltzmann equation,

$$\partial_t f + \frac{p_z}{E}\partial_z f + \dot{p}_z \partial_{p_z} f = -C[f], \tag{1.61}$$

where the collision term on the r.h.s of above equation needs to include all possible scattering processes affecting the distribution f. Ref. [188, 184] used a simpler three parameter fluid ansatz for the form of f and obtained a set of coupled transport equations for these quantities including also ϕ which they solved numerically. Values of v_w in the literature range from ≈ 0.01 to ≈ 0.6 [184] depending on the details of the model. From these we note that the value of v_w constitutes a large uncertainties in the EWBG calculations on phenomenological studies.

1.3.3 Vacuum Transition Rate

At zero temperature, the transition between two topologically different Electroweak vacua happens through tunnelling over the barrier between adjacent vacua. The rate of this process is characterized by instantons [211, 46] which interpolate these two vacua with a rate roughly equals $\exp(-\frac{8\pi^2}{g^2}) \approx 10^{-162}$ [216] and thus infeasible for generating enough baryons. However when temperature is high enough to surpass the Sphaleron barrier, this transition can happen classically by hopping over the barrier instead of tunnelling through it. The rate that this hopping process happens can be defined classically [27, 28]

$$\Gamma = \langle \delta(x) p \theta(p) \rangle, \tag{1.62}$$

and is found to be [27, 28]

$$\frac{\Gamma}{V} = \text{const} \left(\frac{E_{\text{sph}}}{T} \right)^3 \left(\frac{m_W(T)}{T} \right)^4 T^4 e^{-E_{\text{sph}}/T}, \tag{1.63}$$

where $\frac{E_{\text{Sph}}}{T} \approx A * \frac{4\pi}{g} \frac{v(T)}{T}$ with A corresponding the quantity plotted in Fig. 1.5 but at finite T and taking the value of approximately 2. Note that the validity of above expression is when above discussions of the Sphaleron is valid, that is, when the Higgs takes a vev lower than the trivial vacuum. The temperature at which the newly developed vacuum is dengerate with the trivial one is the critical temperature(T_c) of the Electroweak phase transition and will be discussed in following sections. For $T < T_c$, the new vacuum is lower than the trivial one and a Sphaleron solution can be found following discussions in previous sections and the rate takes the form as in above equation. However when $T > T_c$, the Higgs only has the trivial vacuum and there is no Sphaleron solution and no energy barrier at all. The rate that the vacua transition happens in these two different eras take different forms. Calculations above the critical temperature is plagued by non-perturbative infrared effects and generally lattice simulations [106, 107, 190] is needed with the rate defined by

$$\Gamma' = \lim_{V \to \infty} \lim_{t \to \infty} \frac{\langle [N_{CS}(t) - N_{CS}(0)]^2 \rangle}{Vt}. \tag{1.64}$$

Note that even though there is no Sphaleron solution in this case, the above vacua transition rate is still call the Sphaleron rate due to historical reasons. Also the rate in this regime is much faster than that in the broken phase [107].

1.3.4 Sphaleron Decoupling Condition

To maintain the created baryon asymmetry within the broken phase, the Sphaleron rate has to be suppressed in this phase. This condition is called the Sphaleron decoupling condition or Sphaleron bound [207, 208]. A naive way of estimating this bound is to require that the Sphaleron rate be less than the rate of the expansion of the universe, that is, $\Gamma_{\rm sph} < H$. Using Eq. 1.63, this translates into a lower bound on the Sphaleron energy at finite temperature. From previous calculations of the Sphaleron energy, we know that the Sphaleron energy is $A(T)\frac{4\pi v(T)}{g} = A(T)(\frac{4\pi}{\alpha_w})^{1/2}v(T)$ with the prefactor $A(T)$ varying between roughly 1.6 and 2.7, so the bound on Sphaleron energy can be expressed as a lower bound on the quantity $v(T)/T$ at a temperature below the critical temperature. Since this temperature is quite close to the critical temperature T_c, a further estimation is generally made by setting the lower bound as [208, 207]

$$v_c/T_c \gtrsim 1. \tag{1.65}$$

Care should be taken when using this criteria due to the following reasons. Firstly this inequality is actually not a gauge invariant condition in the sense of Ref. [195] and readers are referred to above reference for procedures of implementing a gauge invariant Sphaleron decoupling condition. Secondly, this generally adopted criteria for Sphaleron decoupling in the Electroweak broken phase is actually not universal and it applies to only the standard Electroweak baryogenesis mechanism with a strong first oder EWPT. This relation might be changed with modifications of the Electroweak baryogensis mechanism. For example in a scenario with swifter expansion of the universe through a non-standard cosmology such as with the kinetic energy domination of a scalar field over that from radiation until before the nucleosynthesis era [154, 153], the above bounds on Sphaleron energy as well as on v_c/T_c can be relaxed. A more precise estimation of the Sphaleron decoupling condition can also be found by analyzing in more details the dynamics of the bubbles at the phase transition [154, 189].

1.4 Transport Equations

Having discussed the basic ingredients of the EWBG mechanism, we now gather these altogether in a set of Boltzmann equations to solve for the baryon asymmetry governed by [174]

$$\frac{\partial n_B(\bar{z})}{\partial t} - D\nabla^2 n_B(\bar{z}) = \Theta(-\bar{z}) n_L \Gamma_{ws} n_L + \Theta(-\bar{z}) R\, n_B, \tag{1.66}$$

Here $n_L = \sum_i n_i^L$ is the sum of the left-handed doublet densities in the plasma and serves as the source of the baryon number through the weak Sphaleron interactions whose rate Γ_{ws} is discussed in previous sections. The factor D is the diffusion constant and R characterizes decays of the generated baryon density through the weak Sphaleron process. Note the Sphaleron process is switched on only in the electroweak symmetric phase due to the assumption of a suppressed weak Sphaleron rate in the broken phase given a strongly first order EWPT. The derivative with respect to time can be substituted as that for $\bar{z}$, $\frac{\partial}{\partial_t} = v_w \frac{\partial}{\partial_{\bar{z}}}$. So this equation becomes a second order ordinary differential equations with a constant D and Γ_{ws} which can readily be solved analytically given n_L with n_B a constant in the broken phase,

$$n_B(\bar{z})|_{\bar{z}>0} = \frac{n_L \Gamma_{ws}}{D\lambda_+} \int_0^{-\infty} n_L(x) e^{-\lambda_- x} dx, \tag{1.67}$$

where $\lambda_\pm = \frac{v_w \pm \sqrt{v_w^2 + 4DR}}{2D}$. The only unknown quantity here is the source n_L and requires to write down the transport equations governing all the particle densities in the plasma. Note that these particle densities can be solved together with Eq. 1.67 as a single set of coupled transport equations from which n_B can be directly obtained.

The way that we solve n_L first and then use above equation to solve for n_B is due to the slow rate of weak Sphaleron process.

1.4.1 Closed Time Path Formalism

As mentioned briefly in the beginning of this chapter, the use of CTP formalism leads to resonant enhancement of the CP-violating source terms as well as the relaxation rates. So in this section, we are going to discuss how these terms are calculated in this framework. After all the relevant source terms and relaxation rates are calculated, the resulting coupled transport equations can be solved fully numerically or in some cases analytically and this will be discussed later.

The non-equilibrium nature of the bubble wall expansion picture makes it inappropriate to use equilibrium QFT in solving the particle densities and one need to resort to non-equilibrium QFT which can be described with the real time formalism. Among the several formulations of the real time formalism, we follow closely here the treatment in Ref. [200, 174] by adopting the commonly used closed time path formalism [204, 179, 34, 35, 160, 86, 102]. In this formalism the time is integrated in the complex t plane along the contour from $-\infty$ to $+\infty(\equiv C_+)$, from $+\infty$ back to $-\infty(\equiv C_-)$ and along the negative imarinary time axis. The last segment turns to be irrevelant and thus can be ignored. The resulting integration over time thus takes the form of a closed path and the time ordering in the zero temperature QFT is replaced by a path ordering along this contour. Fields defined along this contour are labelled by a "+" sign when it is on C_+ and a "-" sign if on C_-. Due to this distinction, the Greens function needs four correlators of fields and can be organized in a 2×2 matrix form,

$$G(x,y) = \begin{bmatrix} G_{++}(x,y) & -G^{<}(x,y) \\ G^{>}(x,y) & G_{--}(x,y) \end{bmatrix}. \tag{1.68}$$

This Greens function satisfy the Schwinger-Dyson equatons [174],

$$\begin{aligned} G(x,y) &= G^0(x,y) + \int d^4w d^4z G^0(x,w)\Sigma(w,z)G(x,z), \\ G(x,y) &= G^0(x,y) + \int d^4w d^4z G(x,w)\Sigma(w,z)G(x,z)^0, \end{aligned} \tag{1.69}$$

where G^0 denotes the non-interacting Greens function and Σ is the full interacting self-energy. Note both G^0 and Σ are 2×2 matrices. The transport equations can be derived by applying the Klein-Gordon operator on the $(1,2)$ component of above two equations at spacetime x and y respectively, take the difference and use the limit

$$(\partial^x_\mu - \partial^x_\mu)G^<(x,y)|_{x=y} = -ij_\mu(x), \tag{1.70}$$

which then gives for scalar fields

$$\begin{aligned} \frac{\partial n}{\partial x_0} + \nabla \cdot \vec{j}(x) &= \int d^3z \int_{-\infty}^{x_0} dz_0 [\Sigma^>(x,z)G^<(z,x) - G^>(x,z)\Sigma^<(z,x) \\ &\quad + G^<(x,z)\Sigma^>(z,x) - \Sigma^<(x,z)G^>(z,x)], \end{aligned} \tag{1.71}$$

and similarly for fermionic fields,

$$\begin{aligned} \frac{\partial n}{\partial x_0} + \nabla \cdot \vec{j}(x) &= -\int d^3z \int_{-\infty}^{x_0} dz_0 \mathrm{Tr}[\Sigma^>(x,z)S^<(z,x) - S^>(x,z)\Sigma^<(z,x) \\ &\quad + S^<(x,z)\Sigma^>(z,x) - \Sigma^<(x,z)S^>(z,x)]. \end{aligned} \tag{1.72}$$

where S is similar Greens function defined for fermionic fields.

Outside the electroweak bubble, the Higgs field has no vev and deep inside the bubble, the full Higgs vev at finite temperature T is developed. Across the bubble wall, the Higgs field interpolates between these two phases smoothly. This poses a problem for calculations since for each step closer into the electroweak bubble, the mass eigenstate of various fields at the initial step would no longer be the mass eigenstate at the coordinate with increased vev. One approximation method is to start with the fields in the unbroken phase and incorporate the effect of the increasing Higgs vev perturbatively, known as the vev insertion approximation [200]. Of course, this approximation works well if the Higgs vev is small and slowly varying. To futher reduce the uncertainties introduced in this treatment, one need to perform improvement like the resummation method proposed in Ref [70, 197, 198].

The resulting equations governing the diffusion and scattering of the various particle species can generally be put into this form [88]

$$\partial_\mu j_i^\mu = -\frac{T^2}{6}\sum_X \Gamma_X(\mu_i + \mu_j + \cdots - \mu_k - \mu_l - \cdots) + S_i^{\cancel{CP}}, \tag{1.73}$$

where j_i^μ is the charge current density for particle species "i", Γ_X describes the rate of the scattering process

$$i + j + \cdots \leftrightarrow k + l + \cdots \tag{1.74}$$

and $S_i^{\cancel{CP}}$ is the CP-violating source term that generate the various charge asymmetries in the plasma. We use the diffusion approximation $\vec{j}_i \approx -D_i \vec{\nabla} n_i$, then $\partial_\mu j_i^\mu = \frac{\partial n_i}{\partial t} + \vec{\nabla} \cdot \vec{j}_i = \frac{\partial n_i}{\partial t} - D_i \nabla^2 n_i$ and the diffusion constant D_i can be calculated as in Ref. [156]. Assuming local thermal equilibrium then the number density n_i can be related to the corresponding chemical potential μ_i approximately by a linear relation,

$$\begin{aligned} n_i &= g_i \int_{-\infty}^{+\infty} \frac{d^3\vec{p}}{(2\pi)^3}\left[\frac{1}{\exp(\omega_p - \mu_i) \mp 1} - \frac{1}{\exp(\omega_p - \mu_i) \mp 1}\right], \\ &= \frac{k_i(m_i/T)}{6} T^2 \mu_i + \mathcal{O}(\frac{\mu_i}{T})^3, \end{aligned} \tag{1.75}$$

where "+" and "-" is for boson and Fermion respectively, g_i is the number of internal degrees of freedom of particle species "i", μ_i is its chemical potential, $\omega_p^2 = \vec{p}^2 + m_i^2$ with m_i being the effective mass at temperature T and the statistical factor k_i is given by factor

$$k(m_i/T) = g_i \frac{6}{\pi^2} \int_{m_i/T}^{\infty} dx \frac{x e^x}{(e^x \mp 1)^2} \sqrt{x^2 - m_i^2/T^2}, \tag{1.76}$$

which equals approximatley 1 for fermions and 2 for bosons in the massless limit.

So what remains to calculate is the diffusion constants for various particle species D_i, all relevant rates Γ_X in the plasma and the sources $S_i^{C\!\!\!/P\!\!\!/}$. The diffusion constants can be calculated following the method in Ref. [156, 157] and the calculation of the relaxation rates and CP-violating source terms will be discussed in the following part of this section.

1.4.2 Relaxation and CP-violating Source terms

We consider a generic example with Lagrangian

$$\Delta\mathcal{L} - \bar{\psi}_f \left[g_L(x) P_L + g_R(x) P_R \right] \psi_h + h.c., \tag{1.77}$$

Then

$$\partial_\mu f^\mu = - \int d^3 z \int_{-\infty}^{x_0} \\ \mathrm{Tr} \left\{ \Sigma_f^{>}(x,z) S_f^{<}(z,x) - S_f^{>}(x,z) \Sigma_f^{<}(z,x) + S_f^{<}(x,z) \Sigma_f^{>}(z,x) - \Sigma_f^{<}(x,z) S_f^{>}(x,z) \right\}, \tag{1.78}$$

where the self-energy term is given by

$$\tilde{\Sigma}_f(x,y) = -[g_L(x) P_L + g_R(x) P_R] \hat{S}_h(x,y) [g_L^*(y) P_L + g_R^*(y) P_R], \tag{1.79}$$

Using this in Eq. 1.78, it gives

$$\begin{aligned}\partial_\mu f^\mu &= \int d^3z \int_{-\infty}^{x_0} \sum_{j=A,B} \\ &\left\{[g_j(x,z)+g_j(z,x)]\mathrm{ReTr}[S_h^>(x,z)S_f^<(z,x)-S_h^<(x,z)S_f^>(z,x)]_j\right\} \\ &+i\left\{[g_j(x,z)-g_j(z,x)]\mathrm{ImTr}[S_h^>(x,z)S_f^<(z,x)-S_h^<(x,z)S_f^>(z,x)]_j\right\} \end{aligned} \quad (1.80)$$

where the real part of the trace corresponds to the CP-conserving contribution and gives the relaxation rates while the imaginary part is CP-violating source term. The subscripts "A" and "B" denotes the two different parts in taking the trace. For example, for two generic momenta k, q with the following trace,

$$\mathrm{Tr}[(\not{k}+m_1)(\not{q}+m_2)]_A = 4k\cdot q, \quad (1.81)$$

$$\mathrm{Tr}[(\not{k}+m_1)(\not{q}+m_2)]_B = 4m_1m_2. \quad (1.82)$$

For these two terms, the factor $g_j(x,y)$ is defined as

$$g_A(x,y) = \frac{1}{2}[g_L(x)g_L^*(y)+g_R(x)g_R^*(y)], \quad (1.83)$$

$$g_B(x,y) = \frac{1}{2}[g_L(x)g_R^*(y)+g_R(x)g_L^*(y)]. \quad (1.84)$$

The CP-conserving part will generate the terms

$$S_f^{CPC}(x) = \Gamma_f^+(x)(\mu_f+\mu_h)+\Gamma_f^-(x)(\mu_h-\mu_f), \quad (1.85)$$

and correspond to relaxation terms in the transport equations. Here the relaxation rates is given by

$$
\begin{aligned}
&\Gamma_f^{\pm}(x) = \frac{1}{2\pi^2 T}\mathrm{Im}\int_0^\infty \frac{|\vec{k}|^2 d|\vec{k}|}{\omega_f\omega_h}\Bigg\{\\
&\frac{h_h(\varepsilon_h)\mp h_h(\varepsilon_f^*)}{\varepsilon_h-\varepsilon_f^*}\Big[(\varepsilon_h\varepsilon_f^*-\vec{k}^2)(|g_L(x)|^2+|g_R(x)|^2)+m_f m_h(g_L^*(x)g_R(x)+g_L(x)g_R^*(x))\Big]\\
&\frac{h_h(\varepsilon_h)\mp h_h(\varepsilon_f)}{\varepsilon_h+\varepsilon_f}\Big[(\varepsilon_f\varepsilon_h+\vec{k}^2)(|g_L(x)|^2+|g_R(x)|^2)-m_f m_h(g_L^*(x)g_R(x)+g_L(x)g_R^*(x))\Big]\Bigg\},
\end{aligned}
\tag{1.86}
$$

where in the drivation the following assumptions were used

$$g_A(x,z)+g_A(z,x)\approx 2g_A(x,x)=|g_L(x)|^2+|g_R(x)|^2, \tag{1.87}$$

$$g_B(x,z)+g_B(z,x)\approx 2g_B(x,x)=g_L^*(x)g_R(x)+g_L(x)g_R^*(x), \tag{1.88}$$

The calculation of the CP-violating source terms $S_i^{C\!\!/P}$ basically parallels above CP-conserving calculations. However the factor $g_j(x,y)-g_j(y,x)$ that appears in Eq. 1.80 vanishes at leading order in the expansion of y near x, so we keep the next order in this expansion and define the expansion coefficients,

$$g_A(x,y)-g_A(y,x)=i\mathrm{Im}\left[g_L(x)g_L^*(y)+g_R(x)g_R^*(y)\right]\equiv iH_\mu^A(y-x)^\mu+\cdots, \tag{1.89}$$

$$g_B(x,y)-g_B(y,x)=i\mathrm{Im}\left[g_L(x)g_R^*(y)+g_R(x)g_L^*(y)\right]\equiv iH_\mu^B(y-x)^\mu+\cdots, \tag{1.90}$$

where the coefficients H_μ^A and H_μ^B need to be evaluated in each specific model. Evaluting the traces and inserting the propagators in the equation and it turns out only the time components contribute under the integral therefore only H_0^A, H_0^B appear in the final expression. The source from the "A" term is

$$
\begin{aligned}
S_{f,A}^{CPV}(x) \;=\; & \frac{H_0^A}{\pi^2}\int_0^\infty \frac{|\vec{k}|^2 d|\vec{k}|}{\omega_h\omega_f}\mathrm{Im}\Big\{\frac{(\varepsilon_h\varepsilon_f^*-\vec{k}^2)[n_F(\varepsilon_h)-n_F(\varepsilon_f^*)]}{(\varepsilon_h-\varepsilon_f^*)^2}\\
&-\frac{(\varepsilon_h\varepsilon_f+\vec{k}^2)[n_F(\varepsilon_h)+n_F(\varepsilon_f)]}{(\varepsilon_f+\varepsilon_h)^2}\Big\},
\end{aligned}
\tag{1.91}
$$

and for the “B” term it is

$$S^{CPV}_{f,B}(x) = -\frac{H^B_0}{\pi^2} m_f m_h \int_0^\infty \frac{|\vec{k}|^2 d|\vec{k}|}{\omega_h \omega_f} \mathrm{Im}\left\{ \frac{n_F(\varepsilon_h) - n_F(\varepsilon^*_f)}{(\varepsilon_h - \varepsilon^*_f)^2} - \frac{n_F(\varepsilon_h) + n_F(\varepsilon_f)}{(\varepsilon_f + \varepsilon_h)^2} \right\}, \tag{1.92}$$

Note in above expressions, we have removed the terms that are divergent under the integral and results from the normal ordering of the fields [176].

1.4.3 Analytical Approximations

The transport equations in Eq. 1.73 is a type of coupled set of second order ordinary differential equations which can generally be solved only numerically as discussed in detail in the appendix. However there are certain assumptions under which these equations can be simplified and admit analytical solutions which are used frequently in the literature.

- If the interaction rate Γ_X is sufficiently slow, then the corresponding term can be dropped from the above equation.
- If the interaction rate Γ_X is sufficiently fast, then the corresponding interaction can reach chemical equilibrium, that is,

$$\mu_i + \mu_j + \cdots - \mu_k - \mu_l - \cdots = 0 \tag{1.93}$$

The resulting solution is then actually a perturbative expansion in terms of $\frac{\Gamma}{\Gamma_X}$ where Γ is typical scales of the other interactions rates much smaller than Γ_X. We can verify the correctness of above statement more precisely by numerically investigating a case where such assumptions exist. For this purpose, we study a set of two coupled transport equations regarding two scalar fields H_1 and H_2,

$$\bar{D}_H H_1'' - v_w H_1' - \Gamma_A(H_1 - H_2) - \Gamma_B(H_1 + H_2) + \bar{S}_1 = 0,$$
$$\bar{D}_H H_2'' - v_w H_2' - \Gamma_A(H_2 - H_1) - \Gamma_B(H_1 + H_2) + \bar{S}_2 = 0. \tag{1.94}$$

The asymptotic behavior of H_1, H_2 at $z \to \pm\infty$ is required to be

$$H_i(\pm\infty) = \sum_{n=0}^{\infty} \frac{a_{in}}{z^n} \quad \text{with} \quad i = 1, 2,$$

which we can solve at leader order of the z^{-1} expansion,

$$\begin{bmatrix} \Gamma_A + \Gamma_B & \Gamma_B - \Gamma_A \\ \Gamma_B - \Gamma_A & \Gamma_A + \Gamma_B \end{bmatrix} \begin{bmatrix} H_1 \\ H_2 \end{bmatrix} = \begin{bmatrix} \bar{S}_1 \\ \bar{S}_2 \end{bmatrix} = \begin{bmatrix} 0 \\ 0 \end{bmatrix} \quad \Rightarrow \quad \begin{cases} H_1(\pm\infty) = 0 \\ H_2(\pm\infty) = 0 \end{cases}$$

So $H_{1,2}(z)$ both approach 0 as $z \to \pm\infty$. Now we study a case when Eq. 1.94 has an analytical solution. We assume that $\Gamma_B >> \Gamma_A > 0$. Since Γ_B constitutes the largest scale in the transport equations and much greater than the remaining scale, the transport equations written above can be expanded in power of $\frac{\Gamma}{\Gamma_B} \equiv \delta$ with Γ some other scale in the equations, in particular

$$\Gamma_B(H_1 + H_2) = \Gamma_B \left[\delta + \mathcal{O}(\delta)\right],$$

that is, we solve the transport equations perturbatively in powers of δ. In particular at lead order we have $H_1 = -H_2$. Take the difference of the two equations and use $H_1 = -H_2$ at leading order, we obtain here a single equation for H_1,

$$\bar{D}_H H_1'' - v_w H_1' - 2\Gamma_A H_1 + \frac{\bar{S}_1 - \bar{S}_2}{2} = 0,$$

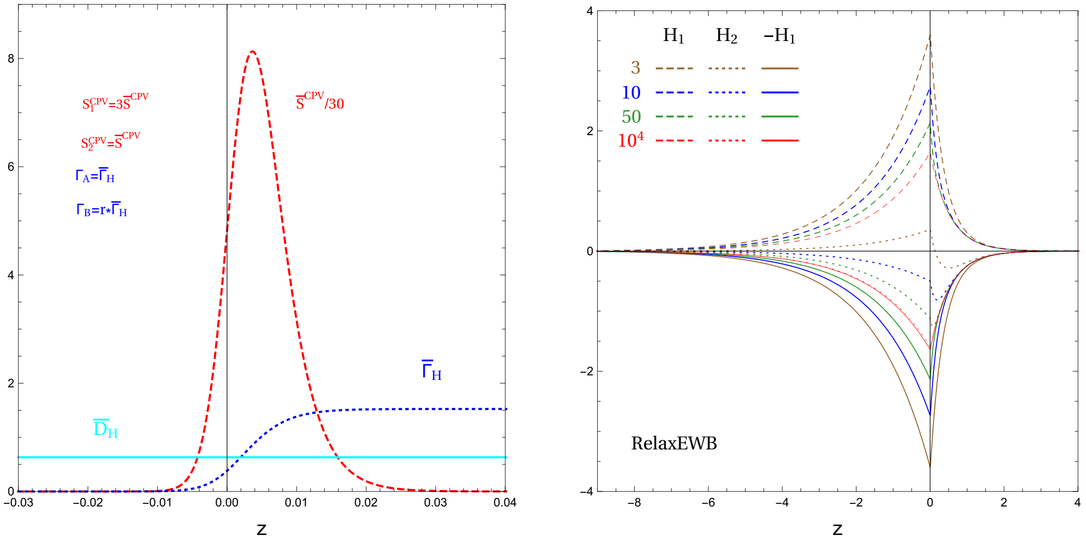

Figure 1.8: The approach to analytical solution of a set of coupled transport equations in Eq. 1.94. The left plot shows the input profiles. The right plot shows the numerically solved solutions of H_1(Dashed) and H_2(Dotted) where $-H_1$(Solid) is also plotted. Each color corresponds a fixed r. As r getting larger, $-H_1$ approaches more closer to H_2.

In this case, so in order to have a non-trivial solution, we need $\bar{S}_1 \neq \bar{S}_2$. If the relaxation coefficient $\bar{\Gamma}_A$ is a constant of z a step-function, this equation can be solved analytically and this is the generally considered analytical approximation in the literature. However near the bubble wall, the relaxation profile is not exactly a step-function which can be solved analytically and a more precise solution requires again numerical solutions. To study how large $\bar{\Gamma}_B$ should be such that $H_1 \approx -H_2$, we choose different ratios r defined by $\bar{\Gamma}_B = r\bar{\Gamma}_A$, numerically solve the original set of transport equations in Eq. 1.94 and show H_1, H_2 and $-H_1$ in Fig. 1.8. In this case, NDSolve can not give stable results and we show only the profiles obtained using RelaxEWB whose correctness has been tested in various cases in previous sections.

In this figure, the left panel shows the input profiles and the right panel shows obtained H_1(dashed), H_2(dotted) and $-H_1$(solid) for several choices of r taking values of 3, 10, 50, 10^4. Here $-H_1$ is to be compared with H_2 and we expect for larger r, $-H_1$

should approach close to H_2. This trend is indeed confirmed in the right plot. For the choices of 10^4, the difference between $-H_1$ and H_2 is barely visible and corresponds to a much more precise analytical approximation.

CHAPTER 2

DARK MATTER

The fact that the majority of the non-relativistic matter in our universe is attributed to dark matter is now well established [209]. A conventional evidence for the existence of DM is from galaxy rotation curves where the measured velocity of luminous stars as a function of distance shows that this can not be accounted for by only the luminous objects and the mass density should include substantial invisible fractions of the dark matter. Recently Ref. [148] shows similar evidence for dark matter from our Milky Way galaxy. More precise measurement of its abundance has been performed by the Planck collaboration from a fit of the base ΛCDM(Lambda Cold Dark Matter) model to correlations of temperature fluctuations in the Cosmic Microwave Background(CMB) radiation. Their 2015 result on the cold dark matter abundance is $\Omega_c h^2 = 0.1186 \pm 0.0020$ at 68% CL [13].

Weakly interacting massive particles(WIMP) can serve as dark matter candidates and will be the focus here. DM is detected traditionally in two ways, direct detection and indirect detection. Direct detection refers to the deep underground experiments looking for events of signals from dark matter scattering off the atomic nuclei. Depending on the types of this interactions, the results are presented as spin-dependent or spin-independent. Of these experiments, the LUX collaboration put currently the strongest constraints on dark matter - nucleon scattering spin-independent cross sections [20]. Indirect detection infers the existence of dark matter through observing dark matter annihilation products which for example can change the normal cosmic rays of rare anti-particles like positrons. There can also be monochromatic gamma rays produced through annihilatioins of dark matter through for example the $\gamma\gamma$ or γZ final states which can provide a sharp peak on top of the continuum gamma ray background. It was also proposed in Ref. [135] to search for indirect signals of DM from merging galaxy clusters such as the Bullet Cluster where the spatial distribution of DM is directly measurable through gravitational lensing which is substantially different from the distribution of potential astrophysical backgrounds. DM can also be searched at colliders. For example for an effective interaction like $\bar{\psi}\psi\bar{q}q$, one process to look at is $\bar{q}q \to \bar{\psi}\psi$ with initial state emissions of jets and this leads to the mono-jet plus missing transverse energy signatures. Searches of this kind of final states have been performed at ATLAS [2, 4, 1] and CMS [77, 79, 162].

Despite the concrete evidence for DM and the ongoing efforts in various experiments searching for it, the SM of particle physics unfortunately does not have a DM candidate and we need to resort to new physics to incorporate a DM candidate. For example in the supersymmetric version of the SM the lightest neutralino can serve as a dark matter candidate. Explaining the DM using a mechanism similar to the generation of baryon asymmetry has also been studied and is named asymmetric dark matter [159, 196, 221]. Since a generic UV-complete model have large parameter space, it is preferred in some cases to use effective field theory(EFT) [68, 47, 33, 115, 133, 84, 220, 85, 83, 199, 178, 218, 134, 121]. But at high energies as for example at LHC, the conditions for EFT is not generally met and this in turn motivates the use of simplified dark matter models [22, 10, 181, 143, 61, 150]. Incorporating dark matters in the SM can also be done with a bottom up approach by opening up portals of interactions of SM particles with dark matter in a minimal way. For example for simple extensions of the SM with an extended Higgs sector, single or multiplets of scalars can be added. This procedure can also be done in the 2HDM and will be studied in detail in later chapters. Due to the increasing strengent upper limit on the DM nucleon scattering cross sections, there are also scenarios proposed with DM quark interactions proceed through loop level diagrams which are generally suppressed as compared with tree level contributions. I will also discuss such scenarios in the 2HDM framework and in a model with lepton portal interactions.

In the following, the calculations of DM relic density and direct detection cross sections are briefly reviewed. While the relic density calculations follow the standard freezing-out approach [172, 50, 132], the direct detection calculations use the systematic non-relativistic EFT theory developed in Ref. [115, 120, 119, 24].

2.1 Relic Abundance

The main observable regarding the properties of dark matter is its inferred relic abundance $\Omega_c h^2$ from cosmological studies. The calculations of this quantity dark matter remain standard following works in Ref. [172, 50, 132] where the freezing out picture is used. In this picture the dark matter remain equilibrium with the SM particles initially through the assumed portal interactions and when the rate of these interactions fall below the expansion rate of the universe, the dark matter abundance freezes around a constant value. Here a brief description is given following above references. For homogeneous and isotropic universe, phase space density $f(\vec{p}, \vec{x}, t)$ is only functions of energy and time whose evolution is governed by the quantum Boltzmann equation,

$$L[f] = C[f] \tag{2.1}$$

where L is the Liouville operator and C denotes the collision terms in the Boltzmann equation. The integral over momentum space over the $L[f]$ gives the density change given by

$$g_1 \int L[f] \frac{d\vec{p_1}^3}{(2\pi)^3} = \dot{n}_1 + 3Hn_1, \tag{2.2}$$

where g_1 is the degrees of freedom of particle density "n_1", H is the Hubble constant and the term on the right hand side of above equation is the dilution of the number density due to the expansion of the universe. The collision term of the Boltzmann equation includes all the inelastic scattering processes increasing or decreasing the DM density while the elastic scattering wont change the density. This gives

$$g_1 \int C[f] \frac{d\vec{p_1}^3}{(2\pi)^3} = -\langle \sigma v_{\mathrm{mol}} \rangle (n_1 n_2 - n_1^{\mathrm{eq}} n_2^{\mathrm{eq}}), \tag{2.3}$$

and then it follows that

$$\dot{n}_1 + 3Hn_1 = -\langle \sigma v_{\mathrm{mol}} \rangle (n_1 n_2 - n_1^{\mathrm{eq}} n_2^{\mathrm{eq}}). \tag{2.4}$$

where $v_{\mathrm{mol}} \equiv \frac{F}{E_1 E_2} = [|\vec{v}_1 - \vec{v}_2|^2 - |\vec{v}_1 \times \vec{v}_2|^2]^{\frac{1}{2}}$ is the Moller velocity, n_i^{eq} is the particle equilibrium distribution and

$$\langle \sigma v_{\mathrm{mol}} \rangle = \frac{\int \sigma v_{\mathrm{mol}} dn_1^{\mathrm{eq}} dn_2^{\mathrm{eq}}}{\int dn_1^{\mathrm{eq}} dn_2^{\mathrm{eq}}} = \frac{\int \sigma v_{\mathrm{mol}} \exp(-\frac{E_1}{T} - \frac{E_2}{T}) d\vec{p_1}^3 d\vec{p_2}^3}{\int \exp(-\frac{E_1}{T} - \frac{E_2}{T}) d\vec{p_1}^3 d\vec{p_2}^3}. \tag{2.5}$$

After evaluating the integrals in the numerator and denominator, the result can be written as a more compact form,

$$\langle \sigma v_{\mathrm{mol}} \rangle = \frac{2\pi^2 T \int \sigma (s - 4m^2) \sqrt{s} K_1(\frac{\sqrt{s}}{T}) ds}{\left[4\pi m^2 T K_2(\frac{m}{T})\right]^2}, \tag{2.6}$$

where the special functions $K_n(a)$ is the modified Bessel function of the second kind,

$$K_n(a) = \frac{\sqrt{\pi}}{(n - \frac{1}{2})!} (\frac{1}{2} a)^n \int_1^\infty e^{-ax} (x^2 - 1)^{n - \frac{1}{2}} dx. \tag{2.7}$$

In the lab frame

$$\langle \sigma v_{\mathrm{lab}} \rangle^{\mathrm{lab}} = \frac{2x}{K_2^2(x)} \int_0^\infty d\epsilon \sqrt{\epsilon} (2\epsilon + 1) K_1(2x\sqrt{\epsilon + 1}) (\sigma v_{\mathrm{lab}}). \tag{2.8}$$

Another quantity $Y_f = n_f/s$ with s the entropy density of the universe is also generally used in cosmological characterization of abundances and its relation to Ω_f is

$$\Omega_f = \frac{\rho_f}{\rho_{crit}} \approx \frac{2.75 \times 10^8}{h^2} \frac{m_f}{\text{GeV}} Y_f. \tag{2.9}$$

2.2 Direct Detection

When dark matter scatters off nuclei, the recoil effects can be detected through the emitting photons and this kind of detection is categorized as the direct detection of dark matter. For example the LUX experiment can measure the number of photoelectrons produced from prompt scintillation(S_1) and from electroluminescence(S_2) of ionization electrons where the requirement of both S_1 and S_2 is to distinguish the WIMP-induced nuclear recoil energy signal from the electromagnetic background of electronic recoils(ERs) [20]. However there is currently no signal for dark matter discovery from direct detection and upper limits are set on cross sections of the dark matter nucleon spin-independent(SI) and spin-dependent(SD) cross sections. Here SI and SD refer to whether the nature of dark matter nucleon interaction is spin-independent or spin-dependent and these two are the traditionally considered set of interactions. Even though more complicated spin structures was also considered in the studies but in a ad hoc way. This picture of dark matter nucleon interactions are far from complete for example a dark matter with non-zero electric dipole moments(EDM) or magnetic dipole moments(MDM) can have more complicated spin interactions with nucleons. Due to the low momentum transfer in this scattering process, an effective field theory framework has been constructed in recent years which incorporates a full set of non-relativistic operators constructed from the Galilean invariant physical quantities [120],

$$i\vec{q}, \quad \vec{v}^{\perp}, \quad \vec{S}_{\psi}, \quad \vec{S}_N \tag{2.10}$$

where $\vec{q}$ is the momentum transfer from nucleon to the fermionic dark matter ψ, $\vec{v}^{\perp} = \vec{v} + \frac{\vec{q}}{2\mu_N}$ with $\vec{v} = \vec{v}_{\psi,\text{in}} - \vec{v}_{N,\text{in}}$, $\vec{S}_\psi$ and $\vec{S}_N$ are the spins of ψ and nucleon N. From this definition the relation $\vec{v}^{\perp} \cdot \vec{q} = 0$ holds. The list of operator relevant for spin-0 and spin-1 mediators are [24],

$$\begin{aligned}
\mathcal{O}_1 &= 1_\psi 1_N \\
\mathcal{O}_2 &= (v^{\perp})^2 \\
\mathcal{O}_3 &= i\vec{S}_N \cdot (\frac{\vec{q}}{m_N} \times \vec{v}^{\perp}) \\
\mathcal{O}_4 &= \vec{S}_\psi \cdot \vec{S}_N \\
\mathcal{O}_5 &= i\vec{S}_\psi \cdot (\frac{\vec{q}}{m_N} \times \vec{v}^{\perp}) \\
\mathcal{O}_6 &= (\vec{S}_\psi \cdot \frac{\vec{q}}{m_N})(\vec{S}_N \cdot \frac{\vec{q}}{m_N}) \\
\mathcal{O}_7 &= \vec{S}_N \cdot \vec{v}^{\perp} \\
\mathcal{O}_8 &= \vec{S}_\psi \cdot \vec{v}^{\perp} \\
\mathcal{O}_9 &= i\vec{S}_\psi \cdot (\vec{S}_N \times \frac{\vec{q}}{m_N}) \\
\mathcal{O}_{10} &= i\vec{S}_N \cdot \frac{\vec{q}}{m_N} \\
\mathcal{O}_{11} &= i\vec{S}_\psi \cdot \frac{\vec{q}}{m_N} \qquad (2.11)
\end{aligned}$$

where $\mathcal{O}_1$ and $\mathcal{O}_4$ are the SI and SD interactions usually considered in the literature. It is found that starting from above set of non-relativistic operators, the final dark matter nucleus cross sections can be written in a factorized form [24]

$$\sum_k R_k(c_i) W_k(\vec{q}^{\,2}) \qquad (2.12)$$

where R_k depends on the coefficients of above non-relativistic operators c_i and is the WIMP response function associated with the $k-$th nuclear response function $W_k(\vec{q}^{\,2})$. In the analysis of Ref. [24], there is a total of six nuclear response functions. To use above framework, the following steps should be followed

- Write down the set of quark level relativistic operators at the scale of typical momentum transfer $\mathcal{O}(50\text{MeV})$.
- Match these quark level operators to nucleon level operators of the form $\bar{\psi}\Gamma_A\psi\bar{N}\Gamma^B N$.
- Decompose the relativistically covariant nucleon level operators into non-relativistic operators in Eq. 2.11.
- Find the WIMP response function R_k using the translation formula in Eq.38 of Ref. [24].
- Calculate the nuclear response functions using the formulae given in Ref. [120].
- Calculate cross sections and compare with experimental limits.

In the following a study a dark matter with non-zero magnetic dipole moment and charge radius is performed to see how to use above framework in detail. This appears in a following project that will be discussed in more detail later. Start from the following dark matter ψ and quark interactions,

$$\Delta\mathcal{L}^{\psi\mathrm{q}} = \sum_q \left[eQ_q b_\psi \bar{\psi}\gamma^\mu\psi\bar{q}\gamma_\mu q + eQ_q\mu_\psi\bar{\psi}i\sigma^{\mu\nu}\psi\frac{q^\nu}{q^2}\bar{q}\gamma_\mu q + d_\psi^q\bar{\psi}\psi\bar{q}q \right], \tag{2.13}$$

where b_ψ and μ_ψ are the charge radius and magnetic dipole moment of ψ, Q_q is the charge of quark species "q" and d_ψ^q comes from a $t-$channel scalar mediation between ψ and q.

To convert these into Lagrangian at nucleon level, we need a matching condition by calculating the amplitude using both quark and nucleon degrees of freedom where Nucleon matrix elemnts are expressed by form factors. For the scalar operator $\langle N|m_q\bar{q}q|N\rangle$, it measures the quark contribution to nucleon mass and the form factor

$$f_{Tq}^N = \frac{\langle N|m_q\bar{q}q|N\rangle}{m_N}, \qquad \text{q=u,d,s,c,b,t} \tag{2.14}$$

is generally used. For light quarks, this can be determined from quark masses and ratios of $B_q = \langle N|\bar{q}q|N\rangle$ [44]. Several groups have worked on this and we use the values tabulated in Table.4 in Ref. [89]. On the other hand, for heavy quarks, it contributes to DM-gluon interactions through loops and the form factor can be calculated from QCD trace anomaly and is related to light quark form factors. The relation is

$$f_{Tq}^N = \frac{2}{27}(1 - \sum_{q=u,d,s} f_{Tq}^N) = \frac{2}{27} f_{Tg}^N, \qquad \text{q=c,b,t} \tag{2.15}$$

For the vector current, we use the following Gordon identity [136] at low momentum transfer

$$\langle N|\sum_q Q_q\bar{q}\gamma^\mu q|N\rangle = \langle N|\bar{N}(Q_N\frac{K^\mu}{2m_N} - \tilde{\mu}_N\frac{i\sigma^{\mu\nu}q_\nu}{2m_N})N|N\rangle, \tag{2.16}$$

where the q is the momentum transfer from nucleon to DM, Q_N is charge, $\tilde{\mu}_N$ is half of the g factor of nucleon, that is, $\tilde{\mu}_p \approx 2.80, \tilde{\mu}_n \approx -1.91$ and $Q_n = 0, Q_p = 1$. Then the nucleon level operators are

$$\Delta\mathcal{L}^{\psi\mathcal{N}} = C_h^N\bar{\psi}\psi\bar{N}N + C_\gamma^N\bar{\psi}\gamma^\mu\psi\bar{N}\gamma_\mu N + C_Q^N\bar{\psi}i\sigma^{\mu\nu}\frac{q_\nu}{q^2}\psi\bar{N}K^\mu N + C_\mu^N\bar{\psi}i\sigma^{\mu\nu}\frac{q_\nu}{q^2}\psi\bar{N}i\sigma^{\mu\nu}q_\nu N, \tag{2.17}$$

with the coefficients of above operators being

$$\begin{aligned}
C_\gamma^N &= eb_\psi \sum_q n_q Q_q = eb_\psi Q_N, \\
C_h^N &= \sum_{q=1}^{6} d_\psi^q \frac{m_N}{m_q} f_{Tq}^N, \\
C_Q^N &= \frac{e\mu_\psi Q_N}{2m_N}, \\
C_\mu^N &= -\frac{e\mu_\psi \tilde{\mu}_N}{2m_N}.
\end{aligned} \tag{2.18}$$

Here the dimension of b_ψ, d_ψ^q is -2 and dimension of μ_ψ is -1. So the couplings in Eq. 2.17 are all of dimension -2. The next step is to do a non-relativistic reduction of the nucleon level operators, that is to calculate the amplitude for $\psi N \to \psi N$ with polarized ψ and N and the results can be represented by the operators given in Eq. 2.11. A convenient reduction table for each relativistic operator has been given in Table.1 in Ref. [24] where the reduction assumes non-relativistic normalizations of $|\psi\rangle, |N\rangle$ and we need an extra factor of $4m_N m_\psi$ here. Then we have

$$\begin{aligned}
\frac{\mathcal{L}^{\psi N}}{4m_\psi m_N} = \quad & C_\gamma^N Q_1 + C_h^N Q_1 + \frac{2m_N}{q^2} C_Q^N \left[-\frac{\vec{q}^2}{2m_\psi} O_1 + 2m_N O_5 - 2m_N \left(\frac{\vec{q}^2}{2m_\psi} O_4 - O_6 \right) \right] \\
& + (C_Q^N + C_\mu^N) \frac{4}{q^2} (\vec{q}^2 O_4 - m_N^2 O_6)
\end{aligned} \tag{2.19}$$

Use the expressions of $C_\gamma^N, C_h^N, C_Q^N, C_\mu^N$, we then have

$$\begin{aligned}
\mathcal{L}^{\psi q} = \quad & \left[4m_\psi m_N \left(eb_\psi Q_N + \sum_{q=1}^{6} d_\psi^q \frac{m_N}{m_q} f_{Tq}^N \right) + e\mu_\psi Q_N 2m_N \right] O_1 \\
& + 8e\mu_\psi m_\psi \tilde{\mu}_N (O_4 - \tilde{O}_6^{lr}) + 8e\mu_\psi Q_N m_N m_\psi \tilde{Q}_5^{lr},
\end{aligned} \tag{2.20}$$

and we have defined the long-range operators with a tilde by

$$\begin{aligned}
\tilde{Q}_5^{lr} &= \frac{m_N O_5}{q^2} = -\frac{m_N O_5}{\vec{q}^2}, \\
\tilde{Q}_6^{lr} &= -\frac{m_N^2 O_6}{q^2} = \frac{m_N^2 O_6}{\vec{q}^2}.
\end{aligned} \tag{2.21}$$

As a check, these two long range operators are essentially the same as those defined in Ref. [89] since the operator O_5 needs a factor of m_N and minus sign from different definition of $\vec{q}$ to be the same as in that literature while O_6 needs a factor of m_N^2. Keeping only the μ_ψ term, we recover the result in Ref. [89].

With the non-relativistic operators and their coefficients calculated, the cross section can be written down in a factorized form in Eq. 2.12 where the coefficients of the various nuclear responses can be readily obtained from Eq.38 in Ref. [24] which are functions of the coefficients of above non-relativistic operators.

Finally we can calculate the differential rate with respect to the nuclear recoil energy E_R from the differential cross section. The differential rate($\mathcal{R}$) with respect to E_R per kilogram of target can be written as an integral over the DM velocity distribution,

$$\frac{d\mathcal{R}}{dE_R} = N_T \frac{\rho_\psi}{m_\psi} \int_{v_{min}} v f(\vec{v}) \frac{d\sigma}{dE_R} d^3\vec{v}, \tag{2.22}$$

where N_T is the number of nuclei per kilogram, $f(\vec{v})$ is the local dark matter velocity distribution, ρ_ψ is the local DM mass density($\approx 0.3\text{GeV/cm}^2$). Note that above procedure of inputing the nuclear responses from the set of non-relativistic operators have been streamlized in a public package [89] and will be used in later analysis.

It should be noted that a global analysis can be performed on the full set of Wilson coefficients of the non-relativistic operators rather than being restricted to the SI and SD interpretations of the experimental limits. For example the SuperCDMDS collaboration has set limits on coefficients of these operators [203] using optimum interval method. Global analysis in this direction has also been considered in Bayesian and frequentist framework [72, 26].

CHAPTER 3

THE TWO HIGGS DOUBLET MODEL

In this chapter a brief introduction to the two Higgs doublet model(2HDM) is given since most of the work is set in this model or its extentions. The 2HDM is a simple extention of the SM with one more repetition of the Higgs doublet and was originally introduced to provide sources of time reversal violation [175](See [59] for a review). This model is extensively studied in the literature due to the following reasons: the Higgs sector of the type II 2HDM is similar to the Higgs sector in supersymmetric theories, the precision ρ parameter constraint is naturally satisifed at tree level, there are new sources of CP-violation(equivalent to T-violation from CPT conservation) which makes this model capable to explain the BAU, etc,.

Define the two Higgs doublets by $\Phi_1 = (\varphi_1^+, (v_1 + \rho_1 + i\eta_1)/\sqrt{2})^T$, and $\Phi_2 = (\varphi_2^+, (v_2 + \rho_2 + i\eta_2)/\sqrt{2})^T$ where $v_1 \equiv v\cos\beta$, $v_2 \equiv v\sin\beta$, $v \equiv 256\text{GeV}$, ρ_1 and ρ_2 are two CP-even scalars, η_1, η_2 are two CP-odd scalars and $\varphi_1^\pm, \varphi_2^\pm$ are two charged scalars in the gauge eigenbasis. In total there are eight degrees of freedom and three of them would become the unphysical Goldstones leaving five physical scalars $h_1, h_2, h_3, H^\pm$. The physical particle spectrum can be determined once the potential is given. The most general renormalizable potential is [59]

$$\begin{aligned}
V_H &= m_{11}^2\Phi_1^\dagger\Phi_1 + m_{22}^2\Phi_2^\dagger\Phi_2 - (m_{12}^2\Phi_1^\dagger\Phi_2 + h.c.) \\
&\quad + \frac{1}{2}\lambda_1(\Phi_1^\dagger\Phi_1)^2 + \frac{1}{2}\lambda_2(\Phi_2^\dagger\Phi_2)^2 + \lambda_3(\Phi_1^\dagger\Phi_1)(\Phi_2^\dagger\Phi_2) + \lambda_4(\Phi_1^\dagger\Phi_2)(\Phi_2^\dagger\Phi_1) \\
&\quad + \left[\frac{1}{2}\lambda_5(\Phi_1^\dagger\Phi_2)^2 + \lambda_6(\Phi_1^\dagger\Phi_1)(\Phi_1^\dagger\Phi_2) + \lambda_7(\Phi_2^\dagger\Phi_2)(\Phi_1^\dagger\Phi_2) + h.c.\right], \qquad (3.1)
\end{aligned}$$

where there are 6 real parameters m_{11}^2, m_{22}^2, λ_1, λ_2, λ_3, λ_4 and 4 complex parameters m_{12}^2, λ_5, λ_6, λ_7 and therefore a total of 14 real parameters. The minimization conditions will reduce three parameters. From the minimization with respect to the direction of ρ_1 and ρ_2 around the vacuum, the two parameters m_{11}^2 and m_{22}^2 can be solved as a function of the other parameters,

$$
\begin{aligned}
0 = \frac{\partial V_H}{\partial \rho_1} \Rightarrow m_{11}^2 &= \quad t_\beta \mathrm{Re}(m_{12}^2) - \frac{1}{2} v^2 \left[\lambda_1 c_\beta^2 + \lambda_{345} s_\beta^2 + 3\lambda_6^{\mathrm{Re}} s_\beta c_\beta + \lambda_7^{\mathrm{Re}} s_\beta^2 t_\beta\right], \\
0 = \frac{\partial V_H}{\partial \rho_2} \Rightarrow m_{22}^2 &= \cot_\beta \mathrm{Re}(m_{12}^2) - \frac{1}{2} v^2 \left[\lambda_2 s_\beta^2 + \lambda_{345} c_\beta^2 + \lambda_6^{\mathrm{Re}} c_\beta^2 \cot_\beta + 3\lambda_7^{\mathrm{Re}} s_\beta c_\beta\right],
\end{aligned}
\tag{3.2}
$$

while minimizing in the direction of η_1 and η_2 can only solve one more parameter since they lead to similar conditions

$$
\begin{aligned}
0 = \frac{\partial V_H}{\partial \eta_1} &= v s_\beta \mathrm{Im}\left[v^2 \left(s_\beta c_\beta \lambda_5 + c_\beta^2 \lambda_6 + s_\beta^2 \lambda_7\right) - 2 m_{12}^2\right], \\
0 = \frac{\partial V_H}{\partial \eta_2} &= v c_\beta \mathrm{Im}\left[v^2 \left(s_\beta c_\beta \lambda_5 + c_\beta^2 \lambda_6 + s_\beta^2 \lambda_7\right) - 2 m_{12}^2\right].
\end{aligned}
\tag{3.3}
$$

Note this condition also follows from the requirement that Goldstones get no mass from the potential, that is, from requiring $\det(M_{\mathrm{SC}}^2) = \det(M_{\mathrm{SN}}^2) = 0$ where M_{SC}^2 and M_{SN}^2 are the mass matrix for charged scalars $\varphi_1^\pm$, $\varphi_2^\pm$ and neutrl CP-odd scalars η_1, η_2 respectively. From this condition we can solve for $\mathrm{Im}(m_{12}^2)$ if it is non-zero,

$$
\mathrm{Im}(m_{12}^2) = \frac{1}{2} v^2 \left[s_\beta c_\beta \lambda_5^{\mathrm{Im}} + c_\beta^2 \lambda_6^{\mathrm{Im}} + s_\beta^2 \lambda_7^{\mathrm{Im}}\right]. \tag{3.4}
$$

Using this in M_{SC}, the mass matrix for charged scalars is

$$
M_{\mathrm{SC}}^2 = \overbrace{\left\{\frac{\mathrm{Re}(m_{12}^2)}{s_\beta c_\beta} - \frac{1}{2} v^2 \left[\lambda_4 + \lambda_5^{\mathrm{Re}} + \lambda_6^{\mathrm{Re}} \cot\beta + t_\beta \lambda_7^{\mathrm{Re}}\right]\right\}}^{\equiv \mathbf{m^2_{H^\pm}}} \begin{bmatrix} s_\beta^2 & -s_\beta c_\beta \\ -s_\beta c_\beta & c_\beta^2 \end{bmatrix} \tag{3.5}
$$

and from diagonalization of it, the mass eigenstates are

$$\begin{aligned} G^{\pm} &= c_\beta \varphi_1^{\pm} + s_\beta \varphi_2^{\pm}, \\ H^{\pm} &= -s_\beta \varphi_1^{\pm} + c_\beta \varphi_2^{\pm}, \end{aligned} \tag{3.6}$$

where the mass of the charged Higgs is $m_{H^\pm}$ as defined above. For neutral scalars, it is convenient to isolate the neutral Goldstone boson through the following definition

$$G^0 = c_\beta \eta_1 + s_\beta \eta_2, \tag{3.7}$$

$$A^0 = -s_\beta \eta_1 + c_\beta \eta_2. \tag{3.8}$$

where G^0 is the Goldstone boson and A_0 a CP-odd scalar which is a mass eigenstate if there is no CPV in the potential. With this definition, the mass matrix for $(G^0, \rho_1, \rho_2, A_0)$ is block diagonal with G^0 already a mass eigenstate. The 3×3 mass matrix for the remaining scalars (ρ_1, ρ_2, A_0) is given by a real symmetric matrix $\hat{m}^2$ with matrix elements

$$\begin{aligned} \hat{m}^2_{11} &= t_\beta \mathrm{Re}(m^2_{12}) + \frac{1}{2} v^2 \left[2\lambda_1 c^2_\beta + 3\lambda_6^{\mathrm{Re}} s_\beta c_\beta - \lambda_7^{\mathrm{Re}} s^2_\beta t_\beta\right], \\ \hat{m}^2_{22} &= \cot_\beta \mathrm{Re}(m^2_{12}) + \frac{1}{2} v^2 \left[2\lambda_2 s^2_\beta + 3\lambda_7^{\mathrm{Re}} s_\beta c_\beta - \lambda_6^{\mathrm{Re}} c^2_\beta \cot_\beta\right], \\ \hat{m}^2_{33} &= \frac{\mathrm{Re}(m^2_{12})}{s_\beta c_\beta} - \frac{1}{2} v^2 t_\beta \left[2\lambda_5^{\mathrm{Re}} \cot\beta + \lambda_6^{\mathrm{Re}} \cot^2\beta + \lambda_7^{\mathrm{Re}}\right], \\ \hat{m}^2_{12} &= -\mathrm{Re}(m^2_{12}) + \frac{1}{2} v^2 \left[\lambda_{345} s_{2\beta} + 3\lambda_6^{\mathrm{Re}} c^2_\beta + 3 s^2_\beta \lambda_7^{\mathrm{Re}}\right], \\ \hat{m}^2_{13} &= -\frac{1}{2} v^2 \left[s_\beta \lambda_5^{\mathrm{Im}} + 2 c_\beta \lambda_6^{\mathrm{Im}}\right], \\ \hat{m}^2_{23} &= -\frac{1}{2} v^2 \left[c_\beta \lambda_5^{\mathrm{Im}} + 2 s_\beta \lambda_7^{\mathrm{Im}}\right], \end{aligned} \tag{3.9}$$

and the minimization conditions have been used in obtaining above expressions. Clearly, when there is no CPV, that is when λ_5, λ_6 and λ_7 are all real, A^0 is a mass eigenstate. However generally when there is CPV, A^0 would mix with ρ_1 and ρ_2. This mass matrix $\hat{m}^2$ can be diagonalized by a rotation matrix R,

$$R\hat{m}^2 R^T = \text{diag}(m_{h_1}^2, m_{h_2}^2, m_{h_3}^2), \tag{3.10}$$

and from this definition of R, the physical states h_1, h_2, h_3 is related to the gauge eigenstates by

$$\begin{bmatrix} h_1 \\ h_2 \\ h_3 \end{bmatrix} = R \begin{bmatrix} \rho_1 \\ \rho_2 \\ A_0 \end{bmatrix}. \tag{3.11}$$

The rotation matrix R can be parametrized by three angles γ, δ, σ,

$$\begin{aligned} R(\gamma, \delta, \alpha) &= R(\vec{e}_1, -\gamma) R(\vec{e}_2, -\delta) R(\vec{e}_3, -\alpha) \\ &= \begin{bmatrix} c_\alpha c_\delta & s_\alpha c_\delta & -s_\delta \\ s_\gamma s_\delta c_\alpha - s_\alpha c_\gamma & s_\alpha s_\delta s_\gamma + c_\alpha c_\gamma & s_\gamma c_\delta \\ s_\alpha s_\gamma + s_\delta c_\alpha c_\gamma & s_\alpha s_\delta c_\gamma - s_\gamma c_\alpha & c_\gamma c_\delta \end{bmatrix}, \end{aligned} \tag{3.12}$$

In the absence of CPV, $\gamma = \delta = 0$ and α is the traditionally defined mixing angle of the two CP even states ρ_1 and ρ_2 [138],

$$R(0, 0, \alpha) = \begin{bmatrix} c_\alpha & s_\alpha & 0 \\ -s_\alpha & c_\alpha & 0 \\ 0 & 0 & 1 \end{bmatrix}. \tag{3.13}$$

In above definition of the rotation matrix R, h_1 is the defined as a CP-even Higgs scalar and h_2 is another CP-even scalar identified as the SM Higgs boson. With h_2 defined as the SM Higgs, above definition of α is the same mixing angle as traditionally defined angle in the literature if there is no CPV in the potential. It is useful to note that there exist several different definitions of the rotation angles. The rotation matrix in Ref. [164] can be obtained using the following replacement $\gamma = \alpha_c, \delta = -\alpha_b, \alpha = \tilde{\alpha}$ but there $m_{h_1} < m_{h_2} < m_{h_3}$ is defined. So actually the identification $\tilde{\alpha} = \alpha + \pi/2$ in the CP-conserving limit connect the two kinds of definitions of α but the thus obtained heavier CP-even Higgs has a sign difference. The case in Ref. [215] can be obtained from the identifications $\gamma = \alpha_3, \delta = -\alpha_2, \alpha = \alpha_1$. From the definition of the rotation matrix R in Eq.3.10, the potential parameters can be expressed as functions of the physical parameters including the three neutral scalar masses and three rotation angles,

$$\begin{aligned}
\lambda_1 &= \frac{1}{c_\beta^2}\left[\frac{R^m_{11}}{v^2} - \tilde{\nu} s_\beta^2 + \frac{1}{2}\lambda_7^{\rm Re} s_\beta^2 t_\beta - \frac{3}{2}\lambda_6^{\rm Re} s_\beta c_\beta\right], \\
\lambda_2 &= \frac{1}{s_\beta^2}\left[\frac{R^m_{22}}{v^2} - \tilde{\nu} c_\beta^2 + \frac{1}{2}\lambda_6^{\rm Re} c_\beta^2 \cot_\beta - \frac{3}{2}\lambda_7^{\rm Re} s_\beta c_\beta\right], \\
\lambda_3 &= \frac{1}{s_{2\beta}}\left[2\frac{R^m_{12}}{v^2} - 3\lambda_6^{\rm Re} c_\beta^2 - 3\lambda_7^{\rm Re} s_\beta^2\right] + \tilde{\nu} - \lambda_4 - \lambda_5^{\rm Re}, \\
\lambda_4 &= 2\tilde{\nu} - 2\frac{m_{H^\pm}^2}{v^2} - \lambda_5^{\rm Re} - \lambda_6^{\rm Re}\cot\beta - t_\beta \lambda_7^{\rm Re}, \\
\lambda_5^{\rm Re} &= -\frac{R^m_{33}}{v^2} + \tilde{\nu} - \frac{1}{2}\lambda_6^{\rm Re}\cot\beta - \frac{1}{2}\lambda_7^{\rm Re} t_\beta, \\
\lambda_5^{\rm Im} &= \frac{2}{s_\beta}\left[-\frac{R^m_{13}}{v^2} - \lambda_6^{\rm Im} s_\beta\right], \\
\lambda_5^{\rm Im} &= \frac{2}{c_\beta}\left[-\frac{R^m_{23}}{v^2} - \lambda_7^{\rm Im} s_\beta\right],
\end{aligned} \tag{3.14}$$

where in above equations, $R^m_{ij} = [R^T \mathrm{diag}(m_{h_1}^2, m_{h_2}^2, m_{h_3}^2) R]_{ij}$ and the dimensionless quantity $\tilde{\nu} = \mathrm{Re} m_{12}^2 / v_1 v_2$ is defined to replace the real part of m_{12}^2. Note the parameter $\lambda_5^{\rm Im}$ can be solved in two different ways as is evident from the last two equations and this leads to one more condition on the physical parameters and allows to reduce one more parameter [147]. Of course when there is no CPV in the potential, these last two equations become trivial since $R^m_{13} = 0$ and $\lambda_{5,6,7}^{\rm Im} = 0$. After the potential parameters are expressed as functions of physical parameters, the purely scalar interactions can be obtained straightforwardly by expanding the potential in terms of physical fields and physical parameters.

With now the scalar spectrum determined from the potential, the Yukawa couplings of these calars can be obtained from the $SU(2)_L \times U(1)_Y$ invariant Lagrangian which is given generally by

$$\mathscr{L}_{\text{Yukawa}} = -\overline{Q_L}\left[\sum_{j=1}^{2}\Phi_j Y_j^D\right] D_R - \overline{Q_L}\left[\sum_{j=1}^{2}\widetilde{\Phi_j} Y_j^U\right] U_R - \overline{E_L}\left[\sum_{j=1}^{2}\Phi_j Y_j^E\right] e_R + h.c.. \tag{3.15}$$

Here Q_L, E_L are three vectors in the flavor space with each element being a $SU(2)_L$ doublet, U_R, D_R, E_R are three vectors in the flavor space but $SU(2)_L$ singlets, $\Phi_{1,2}$ are the two Higgs doublets and $\widetilde{\Phi_j} \equiv \epsilon\Phi_j$. Furthermore $Y_{1,2}^U$, $Y_{1,2}^D$, $Y_{1,2}^E$ are 3×3 Yukawa matrice in flavor space. Diagonalizing the fermion fields, the above Lagrangian written in terms of physical states is [59]

$$\begin{aligned}
\mathscr{L}_{\text{Yukawa}} = & - \overline{U}m_U U - \overline{D}m_D D - \overline{E}m_E E \\
& + \frac{\sqrt{2}}{v}G^+\left[\overline{U_R}m_U V D_L - \overline{U_L}V m_D D_R - \overline{\nu_L}m_E E_R\right] + h.c. \\
& - \frac{i}{v}G^0[\overline{U_R}m_U U_L - \overline{U_L}m_U U_R + \overline{D_L}m_D D_R - \overline{D_R}m_D D_L \\
& \qquad + \overline{E_L}m_E E_R - \overline{E_R}m_E E_L] \\
& + \frac{\sqrt{2}}{v}H^+\left[\overline{U_R}N_U^\dagger V D_L - \overline{U_L}V N_D D_R - \overline{\nu_L}N_E E_R\right] + h.c. \\
& - \frac{S_1}{v}\left[\overline{U}m_U U + \overline{D}m_D D + \overline{E}m_E E\right] \\
& - \frac{S_2 + iA^0}{v}\left[\overline{U_R}N_U^\dagger U_L + \overline{D_L}N_D D_R + \overline{E_L}N_E E_R\right] + h.c.
\end{aligned} \tag{3.16}$$

where m_F is the 3×3 diagonal mass matrix for fermions of group "F" and N_F is a 3×3 matrix and is completely arbitrary. In above terms, The first line is the mass terms for quarks and leptons, the following three lines are Yukawa interactions involving the unphysical Goldstone bosons which remain the same as that in the SM, the fifth line is interactions involving charged Higgs $H^\pm$ where V is the CKM matrix and the last two lines give Yukawa interactions of the physical scalars. Here (S_1, S_2, A_0) are the scalars in the Higgs basis, the two Higgs doublet basis when only one doublet has the full vev and the other no vev. This doublets basis can be obtained from the generic basis doublets Φ_1 and Φ_2 by a rotation with angle β,

$$\begin{bmatrix} H_1 \\ H_2 \end{bmatrix} = \begin{bmatrix} c_\beta & s_\beta \\ -s_\beta & c_\beta \end{bmatrix} \begin{bmatrix} \Phi_1 \\ \Phi_2 \end{bmatrix}, \tag{3.17}$$

and it follows that

$$\begin{aligned} H_1 &= \begin{bmatrix} c_\beta \varphi_1^+ + s_\beta \varphi_2^+ \\ \frac{v + c_\beta \rho_1 + s_\beta \rho_2 + i(c_\beta \eta_1 + s_\beta \eta_2)}{\sqrt{2}} \end{bmatrix} \equiv \begin{bmatrix} G^+ \\ \frac{v + S_1 + iG_0}{\sqrt{2}} \end{bmatrix}, \\ H_2 &= \begin{bmatrix} -s_\beta \varphi_1^+ + c_\beta \varphi_2^+ \\ \frac{-s_\beta \rho_1 + c_\beta \rho_2 + i(-s_\beta \eta_1 + c_\beta \eta_2)}{\sqrt{2}} \end{bmatrix} \equiv \begin{bmatrix} H^+ \\ \frac{S_2 + iA_0}{\sqrt{2}} \end{bmatrix}. \end{aligned} \tag{3.18}$$

Then (S_1, S_2, A_0) are related to the physical scalars (h_1, h_2, h_3) by

$$\begin{bmatrix} S_1 \\ S_2 \\ A_0 \end{bmatrix} = \begin{bmatrix} c_\beta & s_\beta & 0 \\ -s_\beta & c_\beta & 0 \\ 0 & 0 & 1 \end{bmatrix} \overbrace{R^{\mathrm{T}} \begin{bmatrix} h_1 \\ h_2 \\ h_3 \end{bmatrix}}^{=(\rho_1, \rho_2, A_0)^{\mathrm{T}}} \equiv \widetilde{R}^{\mathrm{T}} \begin{bmatrix} h_1 \\ h_2 \\ h_3 \end{bmatrix}, \tag{3.19}$$

and a new rotation matrix $\tilde{R}$ is defined for the Higgs basis scalars. For the case of the CP-consering Higgs potential,

$$S_1 = c_{\beta-\alpha} H + s_{\beta-\alpha} h, \tag{3.20}$$

$$S_2 = -s_{\beta-\alpha} H + c_{\beta-\alpha} h. \tag{3.21}$$

For $\beta - \alpha \approx \frac{\pi}{2}$, we can see from Eq. 3.16 that the couplings of the SM-like Higgs takes its SM value. This limit is called the SM limit or the alignment limit. In many following studies, I will take a bottom-up approach by working around this limit and open up the non-SM effects gradually to be consistent with all the phenomenological observations.

Away from the alignment limit, since the matrix N^F is completely arbitrary, there will be flavor changing neutral interactions(FCNI) associated with these scalars at tree level which are generally dangerous since in the SM these processes can only happen at loop level and are thus greatly suppressed. These tree level FCNI can be absent at tree level if N^F is diagonal and can be obtained by allowing each U_R or D_R or E_R to couple to only one of $\Phi_{1,2}$. Fixing up type quarks to couple to Φ_2, there are four ways of assigning couplings of down type quarks and leptons to $\Phi_{1,2}$ with natural flavor conservation [131, 194] at tree level and this corresponds to the four types of 2HDM generally encountered in the literature. I follow the convention of Ref. [37, 114] to call them type I, II, III, IV and note that type III (IV) is also called type Flipped [59] or Y [25] (Lepton-Specific [59] or X [25]). Defining $N_F \equiv \kappa_F m_F$ with the β dependent real factor κ_F given in Table. 3.1 for the four types of 2HDM, we write down explicitly the Yukawa terms related to S_1, S_2, A_0 in a more intuitive form

Type	I	II	III	IV
κ_U	$\cot\beta$	$\cot\beta$	$\cot\beta$	$\cot\beta$
κ_D	$\cot\beta$	$-t_\beta$	$-t_\beta$	$\cot\beta$
κ_E	$\cot\beta$	$-t_\beta$	$\cot\beta$	$-t_\beta$

Table 3.1: The four types of 2HDM and the corresponding factor κ_F.

$$\begin{aligned}\mathcal{L}^{S_1,S_2,A_0}_{\text{Yukawa}} &= -\frac{1}{v}\sum_{F=U,D,E}\sum_{a=1,3} m_F h_a \overline{F}\left[\widetilde{R}^{\mathrm{T}}_{1a} + \kappa_F \widetilde{R}^{\mathrm{T}}_{2a} - i\gamma^5(2I_{3F})\kappa_F \widetilde{R}^{\mathrm{T}}_{3a}\right] F \\ &= -\frac{1}{v}\sum_{F=U,D,E}\sum_{a=1,3} m_F h_a \overline{F}\Big[s_\beta(\cot\beta - \kappa_F)R^{\mathrm{T}}_{1a} + c_\beta(t_\beta + \kappa_F)R^{\mathrm{T}}_{2a} \\ &\qquad -i\gamma^5(2I_{3F})\kappa_F R^{\mathrm{T}}_{3a}\Big] F. \end{aligned} \tag{3.22}$$

The couplings in the other sectors of the 2HDM can be written down straightforwardly. Especially the purely gauge interactions and fermionic kinetic terms are the same as in the SM, the gauge-fixing and FP ghost interactions can be obtained directly from the SM set by substituting S_1 for h. The Higgs kinetic interactions and their interactions with gauge fields are more complicated but can be written down in a compact form using definitions of several rotation matrices as was done in Ref. [137]. One such example is the "SVV" type interactions which is given by

$$\mathcal{L}_{SVV} = g(m_W W^+ W^- + \frac{m_Z}{c_W}\frac{Z^2}{2}) \underbrace{\sum_{a=1}^{3} \widetilde{R}^{\mathrm{T}}_{1a} h_a}_{S_1}, \tag{3.23}$$

where $\widetilde{R}^{\mathrm{T}}_{1a} = c_\beta R^{\mathrm{T}}_{1a} + s_\beta R^{\mathrm{T}}_{2a}$ and the terms in the sum is actually S_1. So S_1 couples fully to WW/ZZ and the strength of the $h_{1,2,3}$ coupling to WW/ZZ depends on their magnitude of component in S_1. This can easily understood by going to Higgs basis and notice that only the term corresponding to the doublet with nonvanishing vev can generate such couplings.

CHAPTER 4

ELECTROWEAK BEAUTYGENESIS

Currently most of the CPV interactions in existing literature are flavor diagonal while EWBG induced by flavor off-diagonal interactions is less studied [95, 213, 176]. The flavor off-diagonal scenario is beneficial in that it wont contribute to EDM until at two-loop order upon properly chosing the Yukawa textures in the weak eigenbasis. Thus it is less severely constrained by the null search result of EDM for various systems which generally impose the most stringent constraint on new sources of CPV. Also there will generally be flavor off-diagonal interactions that provide novel signatures of flavor changing neutral interactions of the Higgs boson. In particular the lepton flavor violating Higgs decays reported by ATLAS [8] and CMS [163] might be connected with this scenario. As the Higgs signal strength measurements in various channels acquire higher precision in the future, this will either confirm or exclude such scenarios. Along this line, in Ref. [176], we introduced a novel scenario that the baryon asymmetry is generated by a flavor off-diagonal CP-violating Yukawa interactions in the down quark sector. This scenario is set in the type III 2HDM with generic Yukawa interactions in the $b - s$ quark system and its connections with CPV in $B_s - \bar{B}_s$ mixing is explored. In this work, we extend our previous analysis by doing a more detailed study of this flavor off-diagonal EWBG scenario. We found that the mass matrix texture in the weak gauge eigenbasis is severely constrained by the bi-diagonalization procedure and we list all possible mass and Yukawa matrix textures thus allowed by this condition. Furthermore we made a more comprehensive and detailed analysis of the phenomenological constraints.

The rest of this paper is organized as follows. In Sec. 4.1, we define our conventions on the type III 2HDM and discuss CP-violation in the Yukawa sector. We then in Sec. 4.3 analyze phenomenological constraints on weak eigenbasis and mass eigenbaiss parameters from experimental measurements of Higgs signal strength measurements, $B_s \to X_s\gamma$, $\bar{B}_s - B_s$ mixing and electric dipole moments. We calculate in Sec. 4.2 the baryon asymmetry within the framework of closed-time-path-formula. We then make a summary.

4.1 Two Higgs Doublet Model

Since our focus is on $b - s$ Yukawa induced CP-violation the details of the 2HDM potential wont matter so much and we consider the softly broken Z_2 symmetric and CP-conserving Higgs potential [59, 138] which is one of the mostly studied case in the literature. This means we take $\lambda_6 = \lambda_7 = 0$ in discussions of chapter 3. Also we do not impose the accompanying Z_2 transformation on the quark sector such that a type III Yukawa texture can be allowed.

4.1.1 Yukawa Interactions and CP-Violation

At high temperatures when Higgs have not yet developed a nonzero vacuum expectation value(vev), the quarks and leptons which later gain their mass through Higgs mechanism are now all massless. The transition from this electroweak symmetric phase to a broken phase occurs during the electroweak phase transition(EWPT) through bubble nucleation, expansion and coalition. The turbulent bubble boundary provides a non-equilibrium environment where the CP-violating interactions leads to a imbalance between left and right handed charge densities which then bias electroweak sphalerons in the symmetric phase to generate a net baryon number. This baryon number is then captured by the expanding bubble and leads to the baryon asymmetry we observed.

The CP-violating interactions that enter this picture add source terms to the coupled transport equations for the various charge densities and the calculation is generally based on the vev insertion approximation [200]. In this approximation, the Higgs vev and its rate of change is assumed to be small and the transition to mass eigenbasis is treated perturbatively by considering particles scattering off the Higgs vev using the bilinear mass terms in the weak eigenbasis.

In 2HDM, the $SU(2)_L \otimes U(1)_Y$ invariant Yukawa interactions one can write down for down type quarks is

$$\mathscr{L}_{\text{Yukawa}}^{\text{Down}} = -\overline{Q_L}\left[\Phi_1 Y_1^D + \Phi_2 Y_2^D\right] D_R + h.c. \tag{4.1}$$

where Q_L and D_R denote three families of left-handed doublet and right-handed singlet quarks and $Y_{1,2}^D$ are two generic Yukawa coupling matrices. Since our focus is the $b - s$ system and the down quark mass is negligible, we adopt the following Yukawa structures with complex $Y_{1,2}^D$ components

$$\begin{aligned} M_D(\bar{z}) &= \frac{v_1(\bar{z})Y_1^D + v_2(\bar{z})Y_2^D}{\sqrt{2}} \\ &= \frac{1}{\sqrt{2}}\left[v_1(\bar{z}) \begin{pmatrix} 0 & 0 & 0 \\ 0 & (Y_1^D)_{22} & (Y_1^D)_{23} \\ 0 & (Y_1^D)_{32} & (Y_1^D)_{33} \end{pmatrix} + v_2(\bar{z}) \begin{pmatrix} 0 & 0 & 0 \\ 0 & (Y_2^D)_{22} & (Y_2^D)_{23} \\ 0 & (Y_2^D)_{32} & (Y_2^D)_{33} \end{pmatrix} \right]. \end{aligned} \tag{4.2}$$

Here we have assumed a one dimensional bubble profile for simplicity and $\bar{z}$ is the spatial coordinate in the bubble wall rest frame with $\bar{z} > 0$ corresponding to broken phase and $\bar{z} < 0$ to unbroken phase. We also assume the Yukawa structures in up-type quark sector are chosen appropriately to reproduce the CKM matrix when Higgs field acquires a full vev.

Some of the phases in the mass matrix can be partly removed via appropriate quark and Higgs field rephasing. It can be seen that the gauge kinetic term and the potential is invariant [101] under the following transformations

$$U(3)_{Q_L} \otimes U(3)_{D_R} \otimes U(2)_H. \tag{4.3}$$

More explicitly, we define the transformation to be

$$D'_R = D(D_R)D_R, \quad Q'_L = D(Q_L)Q_L, \quad \Phi'_i = U_{ij}\Phi_j, \tag{4.4}$$

and the Yukawa matrices is transofrmed to

$$Y_i^{D\prime} = D(Q_L)Y_j^D D^\dagger(D_R)U^*_{ij}. \tag{4.5}$$

For fields rephasing, the transformation matrices are diagonal

$$\begin{aligned} D(Q_L) &= \mathrm{diag}(\cdots, e^{i\theta^L_a}, \cdots), \\ D(D_R) &= \mathrm{diag}(\cdots, e^{i\theta^R_a}, \cdots), \\ U &= \mathrm{diag}(\cdots, e^{i\theta^H_j}, \cdots), \end{aligned} \tag{4.6}$$

with here the index a running over the number of generation of quarks and i taking values of 1 and 2 since there are two Higgs doublets. Defining the phase of $Y^D_{i,ab}$ to be $\theta^Y_{i,ab}$, then from Eq. 4.5, we have

$$\theta'^Y_{i,ab} = \theta^Y_{i,ab} + \underbrace{\theta^L_a - \theta^R_b - \theta^H_i}_{\equiv \xi^i_{ab}}, \tag{4.7}$$

and we have defined ξ^i_{ab} to a linear combination of $\theta^L_a, \theta^R_a, \theta^H_i$ for convenience. For the specific Yukawa structure in Eq. 4.2, we have now eight $\theta^Y_{i,ab}$, eight $\xi_{i,ab}$ and a total of six of $\theta_a^Y, \theta_a^R, \theta_i^H$. The 8×6 transformation matrix from $\theta_1^L, \theta_2^L, \theta_1^R, \theta_2^R, \theta_1^H, \theta_2^H$ to eight ξ_{ab}^i has rank four, thus only four of ξ_{ab}^i are independent and correspondingly a maximum of four of $\theta_{i,ab}^Y$ can be rendered real by rephasings. The number of ways that such 4 phases can be removed is 58 but physical observables should only depend on rephasing invariant representations of CP violation. In our previous study [176], $Y_{1,22}^D$, $Y_{2,22}^D$, $Y_{1,23}^D$ and $Y_{2,23}^D$ are set to be 0. For the remaining 4 of $\theta_{i,ab}^Y$, only 3 of ξ_{ab}^i are independent and the last remaining phase was chosen to be $\theta_{1,32}^Y$.

More generally, if we consider not just fields rephasing but generic transformations then things become more complicated in finding invariant characterizations of CP violation. In SM, there is only one such invariant, the Jarlskog invariant [151, 111]. Generalizations to 2HDM have been studied in the past [57] and invariants are generally constructed by taking traces or determinants of appropriate products of $Y_{i,j}^{U/D}$. In our calculations, we have expressed the CP-violating source terms in terms of such invariants. For more generall transformations, the study of the invariant forms of the result will be postponed to a further study.

In the broken phase when Higgs acquires the full vev (≈ 246 GeV), the diagonalization of the mass matrix in Eq. 4.2 will give the Yukawa interactions in the mass eigenbasis which has already been summarized in Eq. 3.16. The relation between $Y_{1,2}^D$ and m_D, N_D is

$$m_D = A_L^D \frac{v_1 Y_1^D + v_2 Y_2^D}{\sqrt{2}} A_R^{D\dagger}, \qquad N_D = A_L^D \frac{-v_2 Y_1^D + v_1 Y_2^D}{\sqrt{2}} A_R^{D\dagger}, \tag{4.8}$$

and $A_{L/R}^D$ are the matrices that diagonalize the quark mass matrix. The diagonalization of the mass matrix is in fact the singular value decomposition of the complex matrix M_D,

$$M_D = A_L^{D\dagger} \begin{pmatrix} 0 & 0 & 0 \\ 0 & m_s(M_{ij}^D) & 0 \\ 0 & 0 & m_b(M_{ij}^D) \end{pmatrix} A_R^D, \tag{4.9}$$

with unitary matrices $A_{L/R}^D$ each of which can be parametrized by N^2 $(N = 2)$real parameters. The real diagonal mass matrix has N real parameters making the total number of real parameters on the right hand side $2N^2 + N$. However the above decomposition is invariant under the transformation

$$A_{L/R}^{D\prime} = \begin{pmatrix} e^{i\theta_1} & 0 & 0 \\ 0 & e^{i\theta_2} & 0 \\ 0 & 0 & e^{i\theta_3} \end{pmatrix} A_{L/R}^D \tag{4.10}$$

and this can be used to eliminate N phases on r.h.s of Eq. 4.9. So we can parameterize the r.h.s of Eq. 4.9 using $2N^2$ real parameters, or more explicitly, $2 \times \frac{N(N-1)}{2}$ rotation angles, N physical masses and $2 \times \frac{N(N+1)}{2} - N = N^2$ phases. The original M_D, being a generic complex matrix, has $2N^2$ real parameters with N^2 magnitudes and N^2 phases. With such parametrization and for appropriately chosen parameter space, we can find one to one correspondence between these two sets of parameters. In fact physical masses have known values and therefore we actually have $2N^2 - N$ independent real parameters. We discuss then the actual procedure of mass diagonalization and these additional N constraints.

To actually find the map between these two parameters sets, we use the following diagonalization

$$A_L^D M_D M_D^\dagger A_L^{D\dagger} = m_D^2, \quad A_R^D M_D^\dagger M_D A_R^{D\dagger} = m_D^2, \tag{4.11}$$

to find the unitary matrices A_L^D, A_R^D which in most general case can be parametrized by

$$A_L^{D\dagger} = \begin{pmatrix} 1 & 0 & 0 \\ 0 & c_{\alpha_L} & s_{\alpha_L} e^{i\theta_L} \\ 0 & -s_{\alpha_L} e^{-i\theta_L} & c_{\alpha_L} \end{pmatrix} \begin{pmatrix} 1 & 0 & 0 \\ 0 & e^{i\varphi_2^L} & 0 \\ 0 & 0 & e^{i\varphi_3^L} \end{pmatrix}, \tag{4.12}$$

and use the similar definition for $A_R^{D\dagger}$ with $L \to R$. The rotation angle $\alpha_{L/R}$ and phase $\theta_{L/R}$ are defined by

$$\tan\alpha_L = \frac{|M_{22}^D M_{32}^{D*} + M_{23}^D M_{33}^{D*}|}{\lambda_+ - |M_{22}^D|^2 - |M_{23}^D|^2}, \qquad \theta_L = \arg(M_{22}^D M_{32}^{D*} + M_{23}^D M_{33}^{D*}),$$

and

$$\tan\alpha_R = \frac{|M_{22}^{D*} M_{23}^{D} + M_{33}^D M_{32}^{D*}|}{\lambda_+ - |M_{22}^D|^2 - |M_{32}^D|^2}, \qquad \theta_R = \arg(M_{22}^{D*} M_{23}^{D} + M_{33}^D M_{32}^{D*}), \tag{4.13}$$

with here $\lambda_\pm$ being those two eigenvalues of $M_D M_D^\dagger$ or $M_D^\dagger M_D$ relevant for us,

$$\lambda_\pm = \frac{1}{2}\left[\sum_{i,j=2}^{3} |M_{ij}^D|^2 \pm \sqrt{(|M_{22}^D|^2 + |M_{32}^D|^2 - |M_{23}^D|^2 - |M_{33}^D|^2)^2 + 4|M_{22}^D M_{23}^{D*} + M_{32}^D M_{33}^{D*}|^2}\right]. \tag{4.14}$$

For the phases $\varphi_i^{L/R}$ as mentioned earlier, we can determine $\varphi_i^L - \varphi_i^R$ from Eq. 4.9 while $\varphi_i^L + \varphi_i^R$ are redundant and can be rotated away. Equivalently, we can define φ_i^L to be 0 and determine φ_i^R from Eq. 4.9 or vice versa. Choosing the former case, then for each i, we set $\varphi_i^L + \varphi_i^R = 0$ and solve $\varphi_i^L - \varphi_i^R$ from

$$m_i^D e^{i(\varphi_i^L - \varphi_i^R)} = (A_L^D M_D A_R^{D\dagger})_{ii}\big|_{\varphi_{1,\cdots,N}^{L/R}=0}, \quad i = 1, \cdots, N. \tag{4.15}$$

When the texture of M_D is chosen such that the value on the r.h.s. vanishes automatically then $\varphi_i^L - \varphi_i^R$ should be set to 0 so the number of parameters in the weak and mass eigenbasis are the same. Since diagonalized quark masses have known numerical values $\varphi_i^L - \varphi_i^R$ can be solved for each i when the corresponding quark mass m_i^D is non-zero and in addition we have one real constraint on the parameters in the weak basis such that the diagonalized quark mass is indeed the numerical value. When for one i, m_i^D is required to be 0, we set $\varphi_i^L - \varphi_i^R = 0$ and have two more real relations among the weak basis parameters. In our special case of two quark families, we have three real relations among parameters from the following two (one real, one complex) relations,

$$\begin{aligned} \mathrm{tr}(M_D M_D^\dagger) &= \sum_{i,j=2}^{3} |(M_D)_{ij}|^2 = m_s^2 + m_b^2, \\ \det(M_D M_D^\dagger) &= 0 * |(M_D)_{23}(M_D)_{32} - (M_D)_{22}(M_D)_{33}|^2 = 0 * m_s^2 m_b^2. \end{aligned} \tag{4.16}$$

In our following calculations, we take $m_s = 0$ consistently and then the above two relations become

$$\sum_{i,j=2}^{3} |(M_D)_{ij}|^2 = m_b^2 \quad \text{and} \quad (M_D)_{23}(M_D)_{32} = (M_D)_{22}(M_D)_{33}. \tag{4.17}$$

From the first relation, we can see the magnitude of all the matrix elements in M_D are set by the scale of b quark mass and the different components in the mass matrix are competing against each other for magnitude. A larger $b \to s$ transition would make the others to be smaller and on the contrary a larger diagonal element can push the $b \to s$ element to the corner.

Two more conditions follow from the second equation, that is, the equality of the phases and magnitudes of the products of two diagonal and two off-diagonal elements. From these, the number of zeros in M_D can take the value of 0, 2 or 3. In the case of three 3 zeros, the non-vanishing element is $(M_D)_{33}$ and its magnitude is m_b. In this case, there is no CP-violating source terms generated and we do not consider it. If allowing 2 zeros, then one should be diagonal and the other off-diagonal and we have the following four textures

$$\begin{pmatrix} 0 & 0 & 0 \\ 0 & 0 & 0 \\ 0 & \times & \times \end{pmatrix}, \quad \begin{pmatrix} 0 & 0 & 0 \\ 0 & \times & \times \\ 0 & 0 & 0 \end{pmatrix}, \quad \begin{pmatrix} 0 & 0 & 0 \\ 0 & \times & 0 \\ 0 & \times & 0 \end{pmatrix}, \quad \begin{pmatrix} 0 & 0 & 0 \\ 0 & 0 & \times \\ 0 & 0 & \times \end{pmatrix}, \tag{4.18}$$

and the first one is what we considered in our previous work [176]. Here each non-zero component is a linear combination of corresponding two $Y^D_{i,ab}$ matrix elements from Eq. 4.2 and it can be shown 3 of the 4 $Y^D_{i,ab}$ can be made real by field rephasing but the remaining complex number can be any one of them. Physical results however do not depend on the choice of the phase convention and for convenience we always choose the off-diagonal $Y^D_{1,ij}$ $(i \neq j)$ to be the only complex parameter. Therefore we parametrize the off-diagonal mass matrix element in the weak basis after the Higgs acquires a full vev by

$$(M_D)_{ij} = \frac{v s_\beta}{\sqrt{2}} Y^D_{2,ij} [1 + \cot\beta sgn(Y^D_{2,ij}) r_{ij} e^{i\phi_{ij}}], \tag{4.19}$$

with here $r_{ij} = \frac{|Y^D_{1,ij}|}{|Y^D_{2,ij}|}$ and ϕ_{ij} is the phase of $Y^D_{2,ij}$. On the other hand, due to the constraint in Eq. 4.17, we solve the magnitude of the diagonal $Y^D_{2,ii}$ by

$$|Y^D_{2,ii}| = \frac{\sqrt{2(m_b^2 - |M^D_{ij}|^2)}}{v|s_\beta[1 + \cot\beta r_{ii} sign(Y^D_{1,ii} Y^D_{2,ii})]|}, \tag{4.20}$$

which leads to the requirement $m_b \geq |M^D_{ij}|$.

4.2 Baryon Asymmetry Calculations

In this section, we write down the set of coupled differential equations for the various particle densities including the effect of diffusion, particle number changing reactions and CP-violating source terms and solve them analytically under reasonable assumptions to find the baryon number density.

4.2.1 CP-violating Sources

The calculation of the CP-violating source terms $S_i^{\not{C}P}$ entering above quantum Boltzmann equation follows closely the treatement in Ref. [200, 174] and we refer the reader to those references for more details. In our case, the CP-violating source terms are generated by the bilinear terms in the Lagrangian, that is, the mass term for b and s,

$$\Delta\mathcal{L} = -\bar{s}\left[M_{sb}^{D}(\bar{z})P_R + M_{bs}^{D*}(\bar{z})P_L\right]b - \bar{b}\left[M_{bs}^{D}(\bar{z})P_R + M_{sb}^{D*}(\bar{z})P_L\right]s, \tag{4.21}$$

This then generate the CP-violating source term for "b_L" in Eq. 1.73,

$$\begin{aligned} S_{b_L}^{\not{C}P} &= \frac{N_c v_w |M_{bs}^D(\bar{z})|^2 \frac{\partial\theta_{bs}^D(\bar{z})}{\partial\bar{z}}}{\pi^2}\int_0^\infty \frac{dk k^2}{\omega_{b_L}\omega_{s_R}} \\ &\quad \mathrm{Im}\left\{\frac{(\varepsilon_{b_L}^*\varepsilon_{s_R} - k^2)\left[n_F(\varepsilon_{s_R}) - n_F(\varepsilon_{b_L}^*)\right]}{(\varepsilon_{s_R} - \varepsilon_{b_L}^*)^2} + \frac{(\varepsilon_{b_L}\varepsilon_{s_R} + k^2)\left[n_F(\varepsilon_{s_R}) + n_F(\varepsilon_{b_L})\right]}{(\varepsilon_{s_R} + \varepsilon_{b_L})^2}\right\}, \end{aligned} \tag{4.22}$$

where $n_F = \frac{1}{e^x+1}$ is the Fermi distribution, $N_c = 3$, $\varepsilon_a \equiv \omega_a - i\Gamma_a$ and $\omega_a^2 \equiv k^2 + m_a^2$ for particle a. The source term for s_R is connected with b_L by $S_{s_R}^{\not{C}P} = -S_{b_L}^{\not{C}P}$ while for s_L, b_R, the corresponding source terms can be obtained from above formula by the substitution $b \leftrightarrow s$. In the above expression, the phase $\theta_{ij}^D(\bar{z})$ is defined by

$$M_{ij}^D(\bar{z}) = \frac{1}{\sqrt{2}}\left[v_1(\bar{z})Y_{1,ij}^D + v_2(\bar{z})Y_{2,ij}^D\right] \equiv |M_{ij}^D| e^{i\theta_{ij}^D}, \tag{4.23}$$

and its derivative can be written explicitly by

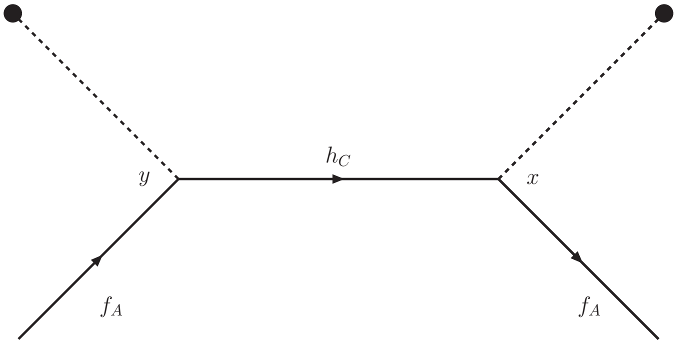

Figure 4.1: Vev insertion approximations, the subscript “A” and “C” denote chiralities “L” or “R”.

$$\begin{aligned}
\theta^{D\prime}_{ij}(\bar{z}) &= \frac{1}{2|M^D_{ij}|^2}[(|v_1|'|v_2| - |v_1||v_2|')|Y^D_{1,ij}Y^D_{2,ij}|\sin(\theta^Y_{1,ij} - \theta^Y_{2,ij}) \\
&\quad + \frac{1}{2}\sum_{ab}|v_a v_b||Y^D_{a,ij}Y^D_{b,ij}|(\theta^Y_{a,ij} + \theta^Y_{b,ij})'\cos(\theta^Y_{a,ij} - \theta^Y_{b,ij})], \qquad (4.24)
\end{aligned}$$

Here all the derivatives are taken with respect to $\bar{z}$ and above phase difference and sum can be written explicitly in a manifestly rephasing invariant way under the transformations in Eq. 4.6,

$$\begin{aligned}
&\theta^Y_{a,ij} - \theta^Y_{b,ij} = \mathrm{Arg}[\frac{v_a v_b^*}{v_a^0 v_b^{0*}}] + \mathrm{Arg}[v_a^0 v_b^{0*} Y^D_{a,ij} Y^{D*}_{b,ij}], \\
&(\theta^Y_{a,ij} + \theta^Y_{b,ij})' = (\mathrm{Arg}[\frac{v_a v_b}{v_a^0 v_b^0}])', \qquad (4.25)
\end{aligned}$$

where v_i^0 is the corresponding vev at zero temperature. We note that fields rephasing only change v_i and Yukawa couplings by global phases which are then independent on $\bar{z}$. Also the same amount of global phase change in v_i will propogate alll the way to v_i^0 leaving their ratio unchanged. On the other hand, the quantity $v_a^0 v_b^{0*} Y^D_{a,ij} Y^{D*}_{b,ij}$ is one of the rephasing invariant quantities at zero temperature and is similar in form to those found in the literature. We note that for real v_1 and v_2, the derivative reduces to

$$\theta^{D\prime}_{ij} = \frac{1}{2|M^D_{ij}|^2}|Y^D_{1,ij}||Y^D_{2,ij}|(v_1' v_2 - v_2' v_1)\sin(\varphi_{Y^D_{1,ij}} - \varphi_{Y^D_{2,ij}}). \tag{4.26}$$

and is just what we used previously in Ref. [176].

4.2.2 Transport Equations and Baryon Asymmetry

We neglect weak sphaleron interactions so we can forget about leptons in the equations and this also implies global baryon number conservation. Furthermore local baryon number is also approximately conserved since their diffusion are dominated by strong interactions. We also assume weak interactions are in thermal equilibrium then particles in the same isodoublet have equal chemical potential. Thus we define $Q_{1,2,3}, U, D, C, S, B, T, H = H_u^+ + H_u^0 - H_d^- - H_d^0$ corresponding to three families of left chiral quarks, right chiral quarks and Higgs bosons in which Q_1, U, C, D are only produced in strong sphaleron interactions. We include also top Yukawa and relaxation processes while neglect others then with all these taken into account we have

$$\begin{aligned}
&Q_1 = -2U = -2C = -2D,\\
&\sum_{i=1}^{3}(Q_i + U_i + D_i) = 0,
\end{aligned} \tag{4.27}$$

which impose constraints among the entire set of 10 charge densities $Q_{1,2,3}$, $U_{1,2,3}$, $D_{1,2,3}$ and H and leave us 6 which we choose to be $Q_2, Q_3, b_R, s_R, t_R, H$.

$$\begin{aligned}
&\partial_\mu Q_2^\mu = 2\Gamma_{ss}\delta_{ss} + S^{\not{C}P}_{s_L},\\
&\partial_\mu Q_3^\mu = \Gamma_{m_t}(\xi_T - \xi_{Q_3}) + \Gamma_t\delta_t + 2\Gamma_{ss}\delta_{ss} + S^{\not{C}P}_{b_L},\\
&\partial_\mu T^\mu = -\Gamma_{m_t}(\xi_T - \xi_{Q_3}) - \Gamma_t\delta_t - \Gamma_{ss}\delta_{ss},\\
&\partial_\mu H^\mu = \Gamma_t\delta_t - 2\Gamma_h H,\\
&\partial_\mu S^\mu = -\Gamma_{ss}\delta_{ss} + S^{\not{C}P}_{s_R},\\
&\partial_\mu B^\mu = -\Gamma_{ss}\delta_{ss} + S^{\not{C}P}_{b_R}.
\end{aligned} \tag{4.28}$$

Here $\delta_{ss} \equiv \sum_{i=1}^{3}(\xi_{U_i} + \xi_{D_i} - 2\xi_{Q_i})$, $\delta_t \equiv \xi_T - \xi_H - \xi_{Q_3}$, $\Gamma_{ss} = 16\kappa' \alpha_s^4 T$ with $\kappa' \approx 1$ is the strong sphaleron rate [186]. For CP violating source terms here, we have $S^{C\!\!\!/P}_{s_R} = -S^{C\!\!\!/P}_{b_L}$ and $S^{C\!\!\!/P}_{b_R} = -S^{C\!\!\!/P}_{s_L}$. Also as usual we ignore the bubble wall curvature and work in the bubble wall rest frame with the coordinate $\bar{z} = x + v_w t$ with v_w being the wall velocity and $\bar{z} < 0$ corresponding to unbroken phase while $\bar{z} > 0$ associated with broken phase. Then all the above number densities are functions of $\bar{z}$. Assuming also $D_{Q_i} = D_{U_i} = D_{D_i} \equiv D$ then we are able to solve the above coupled diffusion equations analytically order by order in $\frac{1}{\Gamma_{ss}}$ and $\frac{1}{\Gamma_t}$ as follows. We define $\delta_2 = Q_2 + 2S$ and $\delta_3 = Q_3 + T + S$ as well as $\delta = S - B$ and then we have

$$
\begin{aligned}
\partial_\mu \delta^\mu &= S^{C\!\!\!/P}_{s_R} - S^{C\!\!\!/P}_{b_R} = S^{C\!\!\!/P}_{s_L} - S^{C\!\!\!/P}_{b_L}, \\
\partial_\mu \delta_2^\mu &= S^{C\!\!\!/P}_{s_L} + 2S^{C\!\!\!/P}_{s_R} = S^{C\!\!\!/P}_{s_L} - 2S^{C\!\!\!/P}_{b_L}, \\
\partial_\mu \delta_3^\mu &= S^{C\!\!\!/P}_{b_L} + S^{C\!\!\!/P}_{s_R} = 0,
\end{aligned}
\tag{4.29}
$$

giving $n_L \equiv \sum_{i=1}^{3} Q_i = -\frac{1}{2}\delta_{ss} k_R$. The last remaining equation is about H which we put in the standard form

T	$\frac{v}{2.5}$	k_B	3	k_H	4
D	$\frac{6}{T}$	D_H	$\frac{110}{T}$	κ	20
v_w	0.4	L_w	$\frac{2}{T}$	κ'	1
$\Delta\beta$	-0.05	α_s	0.09	α_w	$\frac{1}{30}$
θ_w	$\arcsin(\sqrt{0.23})$	Γ_{ws}	$6\kappa\alpha_w^5 T$	Γ_{ss}	$6\kappa' \frac{8}{3}\alpha_s^4 T$
Γ_{b_L,s_R}	$\alpha_s T$	Γ_h	0	s	$\frac{2\pi^2 g_* T^3}{45}$

Table 4.1: Summary of Inputs

$$
\bar{D}_H H'' - v_w H' - \bar{\Gamma}_H H + \bar{S}_H = 0, \tag{4.30}
$$

where $'$ means derivatives with respect to $\bar{z}$, then upon neglecting δ_t and δ_{ss} terms, we have

$$\begin{aligned}
\bar{D}_H &= \frac{7D_H k_H + 6Dk_R}{7k_H + 6k_R}, \\
\bar{\Gamma}_H &= \frac{7\left(2\Gamma_h + \Gamma_{m_t}\right)}{7k_H + 6k_R}, \\
\bar{S}_H &= \frac{k_H(3S^{C\!\!/P}_{b_L} + 4S^{C\!\!/P}_{b_R} + 6S^{C\!\!/P}_{s_L} + 4S^{C\!\!/P}_{s_R})}{7k_H + 6k_R} = \frac{k_H(2S^{C\!\!/P}_{s_L} - S^{C\!\!/P}_{b_L})}{7k_H + 6k_R}.
\end{aligned} \tag{4.31}$$

Another thing to notice is that the assmption $D_L = D_R$ makes coefficients of $\delta, \delta_2, \delta_3$ all vanish. Assuming $\overline{\Gamma}_H$ to be constant of space coordinate, we have the analytical solution for H in the unbroken phase,

$$H(\overline{z} < 0) \;=\; \left[\frac{1}{\overline{D}_H \lambda^H_+} \int_0^\infty \overline{S}_H(u) e^{-\lambda^H_+ u} du\right] e^{v_w \overline{z}/\overline{D}_H}, \tag{4.32}$$

where $\lambda^H_\pm = \frac{v_w \pm \sqrt{v_w^2 + 4\bar{D}_H \bar{\Gamma}_H}}{2\bar{D}_H}$. Now with $H, \delta, \delta_2, \delta_3$ solved at leading order in $\frac{1}{\Gamma_{ss}}$ and $\frac{1}{\Gamma_t}$, n_L being proportional to δ_{ss} can be written down explicitly. Here δ_{ss} can be obtained by plugging the leading order solutions back in the diffusion equaiton and discarding higher order terms,

$$\delta_{ss} = \frac{\partial_\mu Q_2^\mu - S^{C\!\!/P}_{s_L}}{2\Gamma_{ss}}. \tag{4.33}$$

and $Q_2 = \frac{2[k_H(3\delta - \delta_2 - 4\delta_3) + Hk_R]}{7k_H}$, then we have

$$\delta_{ss} = \frac{1}{14\Gamma_{ss}} \left[\frac{2k_R}{k_H}(v_w H' - DH'') - 3S^{C\!\!/P}_{s_L} - 2S^{C\!\!/P}_{b_L}\right]. \tag{4.34}$$

We only need n_L for $\bar{z} < 0$ and since all CP violating source terms vanish, then

$$\begin{aligned}
n_L(\bar{z} < 0) &= -\frac{1}{2}\delta_{ss} k_R \\
&= -\frac{k_R^2}{14\Gamma_{ss} k_H}(v_w H' - DH'') \\
&= -\frac{k_R^2}{14\Gamma_{ss} k_H} \frac{v_w^2}{\overline{D}_H}(1 - \frac{D}{\overline{D}_H}) H(\bar{z}).
\end{aligned} \tag{4.35}$$

The baryon number density ρ_B satisfies the equation [71, 94]

$$\partial_\mu {\rho_B}^\mu = -\Theta(-\bar{z})\Gamma_{ws}(\frac{15}{4}\rho_B + 3n_L), \tag{4.36}$$

where the weak sphaleron rate is given by $\Gamma_{ws} = 6\kappa\alpha_w^5 T$ with $\kappa \approx 20$. The solution of ρ_B in the broken phase is

$$\begin{aligned}
\rho_B(\bar{z})|_{\bar{z}>0} &= \frac{3\Gamma_{ws}}{D\lambda_+^\rho}\int_0^{-\infty} n_L(y)e^{-\lambda_-^\rho y}dy \\
&= \frac{3\Gamma_{ws}}{D\lambda_+^\rho}\left[-\frac{k_R^2}{14\Gamma_{ss}k_H}\frac{v_w^2}{\bar{\bar{D}}_H}(1-\frac{D}{\bar{\bar{D}}_H})\right]\int_0^{-\infty} H(y)e^{-\lambda_\rho^- y}dy\ .
\end{aligned} \tag{4.37}$$

4.3 Phenomenological Constraints

In this section we discuss phenomenological constraints on the parameter space. We first consider the constraints on the modified SM Higgs couplings from the Higgs signal strength measurements and then we discuss how FCNC interactions can alter the precisely measured $B_s^0 - \bar{B}_s^0$ and $B_s \to X_s\gamma$ observables. Finally we consider how searches of electric dipole moment affect the magnitude of CP violation. In all the analysis, we have assumed that the CKM matrix can be faithfully reconstructed from the Yukawa structures we considered by appropriately choosing the up type quark Yukawa textures.

4.3.1 Higgs Signal Strength

In our model, the only modified SM Higgs couplings are $h\bar{d}d'$ interactions. Since we assume no CP violation from the potential, the particle spectrum is the same as those generally considered in other CP-conserving 2HDM while the Yukawa couplings differ

$$h\bar{d}_i d_j : \qquad -s_{\beta-\alpha}\frac{im_{d_i}}{v}\delta_{ij} - c_{\beta-\alpha}\frac{i}{v}[N_{ij}^{D\prime} + N_{ji}^{D\prime *} + (N_{ij}^{D\prime} - N_{ji}^{D\prime *})\gamma_5]. \tag{4.38}$$

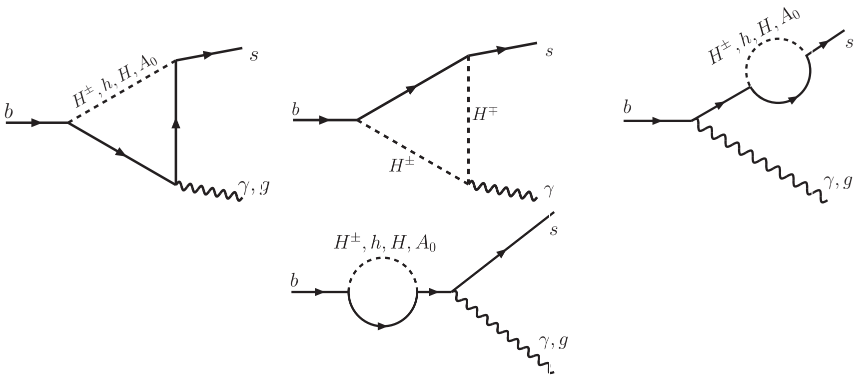

Figure 4.2: Neutral(h, H, A_0) and charged $(H^\pm)$ Higgs contributions to $B_s \to X_s\gamma$ by quark level $b \to s\gamma$ and $b \to sg$. The quarks in the loop are of up and down type for charged and neutral Higgs respectively.

In type I,IV 2HDM, $N'^D = \cot\beta m_D$ and in type II, III $N'^D = -\tan\beta m_D$. In our case, it has non-diagonal terms. Since the couplings from $N^{D\prime}$ does not appear in other channels. Therefore the conclusion that the 2HDM is close to the alignment limit $\beta - \alpha$ is only modified minorly and the deviation depends on how precisely the various Higgs signal strenght are measured. The benefit for BAU is that $\cos\beta - \alpha$ is small and therefore the effect of a relatively large N'^D can be allowed.

4.3.2 $B_s \to X_s\gamma$

For type III 2HDM, flavor changing neutral interactions(FCNI) exist in the Yukawa matrices and therefore contribute to the transition $b \to s\gamma$ and $b \to sg$ at quark level. The resulting rare decay $B_s \to X_s\gamma$ places rather strong constraint on new physics model, so in this section, we see how this would affect our model. Experimentally, the global average of the brahcing ratio from HFAG [23] is

$$\mathrm{Br}(B_s \to X_s\gamma)^{exp}_{E_\gamma > 1.6\mathrm{GeV}} = (355 \pm 24 \pm 9) \times 10^{-6}, \tag{4.39}$$

while the SM calculations give

$$\mathrm{Br}(B_s \to X_s\gamma)^{\mathrm{SM,\ NNLO}}_{E_\gamma > 1.6\mathrm{GeV}} = (315 \pm 23) \times 10^{-6}. \tag{4.40}$$

In 2HDM, one loop level exchange of the neutral and charged Higgs in Fig. 4.2 contributes to this branching ratio through the following two dipole operators (See Ref. [63] for details.)

$$Q_7^{L/R} = \frac{e}{8\pi^2} m_b \bar{s}_\alpha \sigma^{\mu\nu}(1 \mp \gamma^5) b_\alpha F_{\mu\nu}, \quad Q_8^{L/R} = \frac{g}{8\pi^2} m_b \bar{s}_\alpha \sigma^{\mu\nu}(1 \mp \gamma^5) T^a_{\alpha\beta} b_\beta G^a_{\mu\nu}, \tag{4.41}$$

and the associated Wilson coefficients are generally denoted by $C_7^{L/R}$ and $C_8^{L/R}$. Including SM NNLO result using the master formula [185, 65, 52, 53, 56], we can separate new physics contributions from that of SM,

$$\mathrm{Br}(B_s \to X_s \gamma) = \mathrm{Br}_{\mathrm{SM}}^{\mathrm{NNLO}} + 0.00247 \left[|\Delta C_7^L(\mu_b)|^2 + |\Delta C_7^R(\mu_b)|^2 - 0.706 \mathrm{Re}(\Delta C_7^L(\mu_b)) \right], \tag{4.42}$$

where $\Delta C_7^{L/R}(\mu_b)$ characterizes new contributions to the Wilson coefficient $Q_7^{L/R}$ from diagrams in Fig. 4.2 at the scale of B_s meson mass and the expressions for $C_{7,8}^{L/R}$ are summarized in the following. In the running from the 2HDM scale μ_H to hadronic scale, we have neglected extra operators induced by FCNC interactions and their mixing with SM operators.

The four Wilson coefficients C_7^L, C_7^R, C_8^L and C_8^R receive contributions from diagrams shown in Fig. 4.2 by mediations of neutral(h, H_0, A_0) and charged($H^\pm$) Higgs scalars at one-loop. For completeness, we also show the SM contribution from one-loop exchanges of $W^\pm$. We have demonstrated explicit cancellation of the gauge parameter dependence in our calculation and the result here also agrees with Ref. [56].

$$
\begin{aligned}
C_{7L}^{(0)}(\mu_H) &= C_{7L}^{(0)\mathrm{SM}}(\mu_H) + C_{7L}^{(0)H^\pm}(\mu_H) + C_{7L}^{(0)H^0,h,A^0}(\mu_H) \\
&= \sum_{i=u,c,t}\left[\frac{(N_D'^\dagger V^\dagger)_{si}(VN_D')_{ib}}{3m_i^2}F_7^{(1)}(x_i^{H^\pm}) - \frac{(N_D'^\dagger V^\dagger)_{si}(N_U'^\dagger V)_{ib}}{m_i m_b}F_7^{(2)}(x_i^{H^\pm})\right] \\
&\quad -\frac{1}{6}\sum_{i=d,s,b}\Big(\frac{(N_D'^*)_{is}(N_D')_{ib}}{3m_i^2}\left[s_{\beta-\alpha}^2F_8^{(1)}(x_i^{H^0}) + c_{\beta-\alpha}^2F_8^{(1)}(x_i^{h^0}) + F_8^{(1)}(x_i^{A^0})\right] \\
&\quad -\frac{(N_D'^*)_{is}(N_D'^*)_{bi}}{m_i m_b}\left[-s_{\beta-\alpha}^2F_8^{(2)}(x_i^{H^0}) - c_{\beta-\alpha}^2F_8^{(2)}(x_i^{h^0}) + F_8^{(2)}(x_i^{A^0})\right]\Big)\,, \qquad (4.43)
\end{aligned}
$$

$$
\begin{aligned}
C_{7R}^{(0)}(\mu_H) &= C_{7R}^{(0)\mathrm{SM}}(\mu_H) + C_{7R}^{(0)H^\pm}(\mu_H) + C_{7R}^{(0)H^0,h,A^0}(\mu_H) \\
&= \sum_{i=u,c,t}V_{is}^*V_{ib}\left[-\frac{1}{2}A_0(x_i^W)\right] \\
&\quad +\sum_{i=u,c,t}\left[\frac{(V^\dagger N_U')_{si}(N_U'^\dagger V)_{ib}}{3m_i^2}F_7^{(1)}(x_i^{H^\pm}) - \frac{(V^\dagger N_U')_{si}(VN_D')_{ib}}{m_b m_i}F_7^{(2)}(x_i^{H^\pm})\right] \\
&\quad -\frac{1}{6}\sum_{i=d,s,b}\Big(\frac{(N_D')_{si}(N_D'^*)_{bi}}{3m_i^2}\left[s_{\beta-\alpha}^2F_8^{(1)}(x_i^{H^0}) + c_{\beta-\alpha}^2F_8^{(1)}(x_i^{h^0}) + F_8^{(1)}(x_i^{A^0})\right] \\
&\quad -\frac{(N_D')_{si}(N_D')_{ib}}{m_i m_b}\left[-s_{\beta-\alpha}^2F_8^{(2)}(x_i^{H^0}) - c_{\beta-\alpha}^2F_8^{(2)}(x_i^{h^0}) + F_8^{(2)}(x_i^{A^0})\right]\Big)\,, \qquad (4.44)
\end{aligned}
$$

$$
\begin{aligned}
C_{8L}^{(0)}(\mu_H) &= C_{8L}^{(0)\mathrm{SM}}(\mu_H) + C_{8L}^{(0)H^\pm}(\mu_H) + C_{8L}^{(0)H^0,h,A^0}(\mu_H) \\
&= \sum_{i=u,c,t}\left[\frac{(N_D'^\dagger V^\dagger)_{si}(VN_D')_{ib}}{3m_i^2}F_8^{(1)}(x_i^{H^\pm}) - \frac{(N_D'^\dagger V^\dagger)_{si}(N_U'^\dagger V)_{ib}}{m_i m_b}F_8^{(2)}(x_i^{H^\pm})\right] \\
&\quad +\frac{1}{2}\sum_{i=d,s,b}\Big(\frac{(N_D'^*)_{is}(N_D')_{ib}}{3m_i^2}\left[s_{\beta-\alpha}^2F_8^{(1)}(x_i^{H^0}) + c_{\beta-\alpha}^2F_8^{(1)}(x_i^{h^0}) + F_8^{(1)}(x_i^{A^0})\right] \\
&\quad -\frac{(N_D'^*)_{is}(N_D'^*)_{bi}}{m_i m_b}\left[-s_{\beta-\alpha}^2F_8^{(2)}(x_i^{H^0}) - c_{\beta-\alpha}^2F_8^{(2)}(x_i^{h^0}) + F_8^{(2)}(x_i^{A^0})\right]\Big)\,, \qquad (4.45)
\end{aligned}
$$

$$\begin{aligned}
C_{8R}^{(0)}(\mu_H) &= C_{8R}^{(0)\mathrm{SM}}(\mu_H) + C_{8R}^{(0)H^\pm}(\mu_H) + C_{8R}^{(0)H^0,h,A^0}(\mu_H) \\
&= \sum_{i=u,c,t} V_{is}^* V_{ib} \left[-\frac{1}{2} F_0(x_i^W) \right] \\
&\quad + \sum_{i=u,c,t} \left[\frac{(V^\dagger N'_U)_{si}(N'^\dagger_U V)_{ib}}{3m_i^2} F_8^{(1)}(x_i^{H^\pm}) - \frac{(V^\dagger N'_U)_{si}(V N'_D)_{ib}}{m_b m_i} F_8^{(2)}(x_i^{H^\pm}) \right] \\
&\quad + \frac{1}{2} \sum_{i=d,s,b} (\frac{(N'_D)_{si}(N'^*_D)_{bi}}{3m_i^2} \left[s_{\beta-\alpha}^2 F_8^{(1)}(x_i^{H^0}) + c_{\beta-\alpha}^2 F_8^{(1)}(x_i^{h^0}) + F_8^{(1)}(x_i^{A^0}) \right] \\
&\quad - \frac{(N'_D)_{si}(N'_D)_{ib}}{m_i m_b} \left[-s_{\beta-\alpha}^2 F_8^{(2)}(x_i^{H^0}) - c_{\beta-\alpha}^2 F_8^{(2)}(x_i^{h^0}) + F_8^{(2)}(x_i^{A^0}) \right]) \qquad (4.46)
\end{aligned}$$

with here $x_i^f \equiv \frac{m_i^2}{m_f^2}$. The loop integral functions used above are defined following conventions of the SuperIso package [180]

$$\begin{aligned}
A_0(x) &= \frac{-3x^3 + 2x^2}{2(1-x)^4} \ln x + \frac{22x^3 - 153x^2 + 159x - 46}{36(1-x)^3}, \\
F_0(x) &= \frac{3x^2}{2(1-x)^4} \ln x + \frac{5x^3 - 9x^2 + 30x - 8}{12(1-x)^3}, \\
F_7^{(1)}(x) &= \frac{x(7 - 5x - 8x^2)}{24(x-1)^3} + \frac{x^2(3x-2)}{4(x-1)^4} \ln x, \\
F_8^{(1)}(x) &= \frac{x(2 + 5x - x^2)}{8(x-1)^3} - \frac{3x^2}{4(x-1)^4} \ln x, \\
F_7^{(2)}(x) &= \frac{x(3-5x)}{12(x-1)^2} + \frac{x(3x-2)}{6(x-1)^3} \ln x, \\
F_8^{(2)}(x) &= \frac{x(3-x)}{4(x-1)^2} - \frac{x}{2(x-1)^3} \ln x \, . \qquad (4.47)
\end{aligned}$$

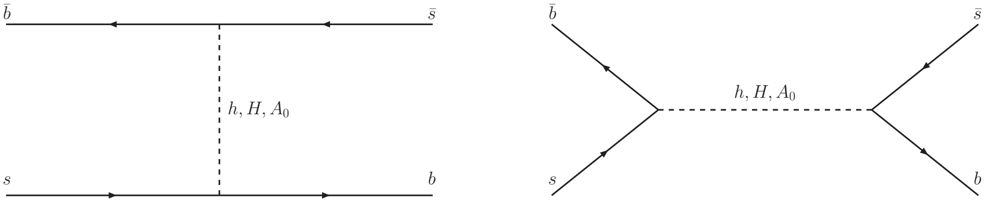

Figure 4.3: h, H and A_0 mediated tree diagram contributions to $B_s^0 - \bar{B}_s^0$ at quark level.

4.3.3 $B_s^0 - \bar{B}_s^0$ Mixing

The presence of flavor changing neutral interactions in the Lagrangian associated with neutral Higgs scalars will contribute to $B_s^0 - \bar{B}_s^0$ mixing through the treel diagrams shown in Fig. 4.3 at quark level. In SM, the mixing happens first at one loop through $W^\pm$ mediated box diagrams and includes a single operator $(\bar{b}\gamma_\mu P_L s)(\bar{b}\gamma^\mu P_L s) + h.c.$ [108, 60]. While for the leading order tree level diagrams shown in Fig. 4.2, a different set of operators contribute and the effective Hamiltonian after integrating out the heavy scalars h, H, A_0 is

$$\mathcal{H}_{\text{eff}}^{\Delta B=2}(\mu_H) = C_1^{\text{SLL}}(\bar{b}P_L s)(\bar{b}P_L s) + C_1^{\text{SRR}}(\bar{b}P_R s)(\bar{b}P_R s) + C_2^{\text{LR}}(\bar{b}P_L s)(\bar{b}P_R s) + h.c \tag{4.48}$$

Here we follow the conventions of Ref. [64] on classifying the operators using "SLL", "SRR" and "LR" and their corresponding Wilson coefficients at 2HDM scale μ_H is

$$C_1^{\text{SLL}} = -\sum_i \frac{(\kappa_{sb}^{i*})^2}{m_i^2 v^2}, \quad C_1^{\text{SRR}} = -\sum_i \frac{(\kappa_{bs}^{i})^2}{m_i^2 v^2}, \quad C_2^{\text{LR}} = -\sum_i \frac{2\kappa_{sb}^{i*}\kappa_{bs}^{i}}{m_i^2 v^2}, \tag{4.49}$$

wherein the sum runs over h, H, A_0 with their respective coupling matrices κ^i given by

$$\kappa^h = -\frac{c_{\beta-\alpha}}{\sqrt{2}}N_D', \quad \kappa^H = \frac{s_{\beta-\alpha}}{\sqrt{2}}N_D', \quad \kappa^{A_0} = -\frac{iN_D'}{\sqrt{2}}. \tag{4.50}$$

Running down to the hadronic scale at B_s mass, the "SLL" operator mixes with the tensor operator $(\bar{b}\sigma_{\mu\nu}P_L s)(\bar{b}\sigma^{\mu\nu}P_L s)$, the "SRR" operator mixes with $(\bar{b}\sigma_{\mu\nu}P_R s)(\bar{b}\sigma^{\mu\nu}P_R s)$ and these two sets have the same evolution matrix since QCD preserves chirality. Furthermore the "LR" scalar operator mixes with $(\bar{b}\gamma_\mu P_L s)(\bar{b}\gamma^\mu P_R s)$. Including also the

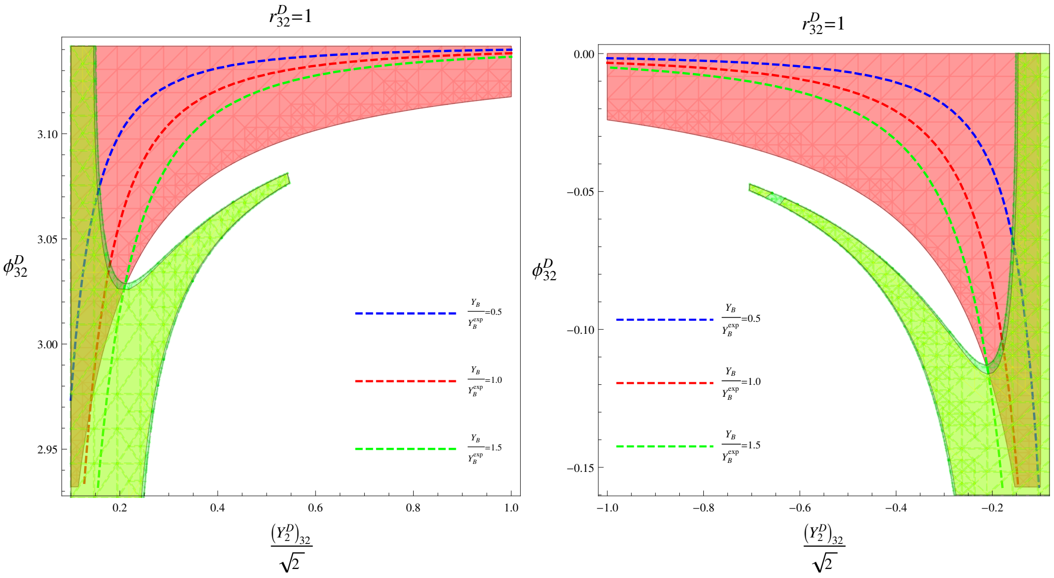

Figure 4.4: Baryon asymmetries with CP violation in B_s meson system incuded. The blue regions are allowed regions from fit to the $B_s^0 - \bar{B}_s^0$ parameters, semileptonic charge asymmetries and CP asymmetries in hadronic B_s decays. Here we have chosen $m_{A_0}/m_H = 1.002$

.

values of the hardonic matrix elements, the final contributions to the $B_s^0 - \bar{B}_s^0$ mass splitting is captured in this equation [64],

$$\Delta M_s = 2|M_{12}^s| = 2\langle\overline{B_s^0}|\mathcal{H}_{\text{eff}}^{\Delta B=2}(\mu_b)|B_s^0\rangle = \frac{2}{3}m_B F_B^2[2.46C_2^{\text{LR}} - 1.47(C_1^{\text{SLL}} + C_1^{\text{SRR}})]. \tag{4.51}$$

Physically this contribution can be probed in the following observables

$$\begin{aligned} \Delta\Gamma_s &= \Delta_s^{\text{SM}}\cos(\phi_s^{\text{SM}} + \phi_s^{\Delta}), \quad \Delta m_s = \Delta m_s^{\text{SM}}|\Delta_s|, \\ a_{\text{SL}}^s &= \frac{\Delta\Gamma^{\text{SM}}}{\Delta m_s^{\text{SM}}}\frac{\sin(\phi_s^{\text{SM}} + \phi_s^{\Delta})}{|\Delta_s|}, \quad 2\beta_s = 2\beta_s^{\text{SM}} - \phi_s^{\Delta}, \end{aligned} \tag{4.52}$$

where Δm_s and $\Delta\Gamma_s$ are the mass and width difference between the heavy and light B_s mesons, a_{SL}^s is the charge asymmetry in semileptonic B_s decays and β_s characterizes the time-dependent CP asymmetries in the hadronic B_s decays. We thus do a combined χ^2 fit to the $D\emptyset$, CDF and LHCb measurements.

Even though the generic Yukawa structures give a tree level meson mixing, there is certain limit when this contribution vanishes. The Higgs signal strength measurements pushes the 2HDM to be close to the alignment limit $\beta - \alpha = \pi/2$ where the couplings of h reduce to those in SM and does not contribute to the above Wilson coefficients. Furthermore the contributions of H and A_0 to C_1^{SLL} and C_1^{SRR} add up to 0 when their masses are degenerate. On the other hand, C_2^{LR} can be made 0 if we keep only one non-diagonal matrix element. In this special situation where all these conditions are met, new physics contributions to mixing occurs at one loop and since their masses are much larger than the $W^\pm$ mass, their contributions are much suppressed. Therefore a large CPV effect for BAU can be quite safe for the mixing.

The final combined plots are shown in Fig. 4.4 where the various phenomenologicall allowed regions are plotted as colored regions. There the dashed lines label the obtained baryon asymmetries relative to the observed value where for the blue lines only half of the baryon asymmetry can be obtained, the red lines give the right amount of baryon asymmetry while the green lines give an over-abundance of the experimentally measured value. From these analysis, we can see a quark sector CPV can provide the mechanism for generating the observed baryon asymmetry while at the same be compatible with the other phenomenological measurements.

CHAPTER 5

LEPTON FLAVORED ELECTROWEAK BARYOGENESIS

In 2015, the CMS collaboration reported the result [163] of their first direct search for the lepton flavor violating(LFV) decays of the Higgs boson in the channel $h \to \tau\mu$ and observed a slight excess with 2.4 standard deviation and with a best fit branching ratio $\mathrm{Br}(h \to \tau\mu) = 0.84^{+0.39}_{-0.37}\%$ as well as an upper limit $\mathrm{Br}(h \to \tau\mu) < 1.51\%$ at 95% CL. Several months later the ATLAS collaboration also presented their search [8] of this channel and put an looser upper limit on this branching ratio $\mathrm{Br}(h \to \tau\mu) < 1.85\%$ at 95%CL. Recently ATLAS updated their result [9] and reported a more stringent upper limit with $\mathrm{Br}(h \to \tau\mu) < 1.43\%$ at 95%CL. This LFV process if futrher confirmed would certainly imply new physics since the SM can not accommodate it. On the other hand if this is indeed the portal where new physics hides, the chances are high that there will also be CPV with this sector which could be responsible for the generation of baryon asymmetry during the early universe. It is also intriguing to see how this CPV that could be origin of the BAU manifests itself phenomenologically at collider searches and in low energy probes of electric dipole moments. We thus study a model with an extended leptonic Yukawa sector where LFV interactions and new sources of CPV exist and study within the framework of EWBG to see if this CPV can generate the right amount of CPV during the EWPT and see how this CPV can be detected at collider searches and low energy probes. We will work in a simple benchmark model, the 2HDM with generic Yukawa interactions in the lepton sector. It can be seen from previous analysis that this kind of interactions can be generated if the right-handed leptons couple to both Higgs doublets.

5.1 Type L Two Higgs Doublet Model.

Since our focus is on CPV in the lepton sector, we assume the potential to be CP-conserving with parameters chosen to generate a strongly first order electroweak phase transition (EWPT) [110, 109]. The particle spectrum consists of two CP-even neutral scalars (h, H), the neutral CP-odd A^0, and a pair of charged scalars $H^{\pm}$. Here we take the lighter h as the SM-like Higgs boson. The $SU(2)_L \times U(1)_Y$ invariant weak eigenbasis lepton Yukawa interaction is

$$\mathscr{L}_{\text{Yukawa}}^{\text{Lepton}} = -\overline{E_L^i}\left[(Y_1^E)_{ij}\Phi_1 + (Y_2^E)_{ij}\Phi_2\right] e_R^j + h.c., \tag{5.1}$$

where $\Phi_{1,2}$ are the two Higgs doublets with the same hypercharge, E_L^i is the left-handed lepton doublet in family "i" and e_R^j is the right-handed lepton singlet in family "j". We focus now on the second and third families, neglecting the muon mass as a first approximation and assuming the Yukawa structures are such that the relevant up- and down- type quarks have similar couplings as those in SM.

The relevant Jarlskog-like CPV invariant that is the origin of both BAU and non-vanishing ϕ_τ is the imaginary part of the following basis invariant [151, 57]:

$$J_E = \frac{1}{v^2 \mu_{12}^{\text{HB}}} \sum_{a,b,c=1}^{2} v_a v_b^* \mu_{bc} \sum_{ij=\tau,\mu} (Y_c^E)_{ij} (Y_a^{E\dagger})_{ji} \quad , \tag{5.2}$$

where $v_a = \sqrt{2}\langle\Phi_a^0\rangle$; μ_{ab} is the coefficient of $\Phi_a^\dagger\Phi_b$ in the potential; and μ_{ab}^{HB} the corresponding value when the $\Phi_{1,2}$ are transformed into the "Higgs basis" [57, 59] in which $\langle\Phi_1^0\rangle = v/\sqrt{2} = 174$ GeV while $\langle\Phi_2^0\rangle = 0$. The value of J_E is invariant under a $U(2)$ Higgs doublets basis transformation and lepton family transformations; it is normalized to $v^2\mu_{12}^{\text{HB}}$ to obtain a dimensionless quantity. Note that J_E takes on different explicit forms in the weak eigenbasis (most convenient for BAU calculations) and the mass eigenbasis (appropriate for phenomenological analyses).

In the weak eigenbasis, the (μ, τ) mass matrix is

$$M^E = (v_1 Y_1^E + v_2 Y_2^E)/\sqrt{2} \quad . \tag{5.3}$$

At $T = 0$ it is bidiagonalized to give the physical masses, which constrains the possible textures for M^E in the weak eigenbasis. For illustration, we choose a texture wherein only the second row elements $Y^E_{j,\tau\mu}$, $Y^E_{j,\tau\tau}$ $(j = 1, 2)$ are non-vanishing. After all possible rephasings of the lepton and Higgs fields, only one of the four non-zero Yukawa matrix elements can be complex, chosen here to be $Y^E_{1,\tau\mu}$. The resulting off-diagonal mass matrix element can be parametrized as

$$M^E_{\tau\mu} = \frac{v s_\beta}{\sqrt{2}} Y^E_{2,\tau\mu}[1 + \cot\beta \ \mathrm{sgn}(Y^E_{2,\tau\mu}) r_{\tau\mu} e^{i\phi^E_{\tau\mu}}] \quad , \tag{5.4}$$

with $r_{\tau\mu} \equiv |Y^E_{1,\tau\mu}|/|Y^E_{2,\tau\mu}|$ and $\tan\beta = v_2/v_1$. We further assume the non-vanishing diagonal elements of the two Yukawa matrices to be equal and positive for simplicity giving then $M^E_{\tau\tau} = v Y^E_{2,\tau\tau}(s_\beta + c_\beta)/\sqrt{2}$. From the diagonalization condition $|M^E_{\tau\mu}|^2 + |M^E_{\tau\tau}|^2 = m_\tau^2$ (neglecting m_μ compared to m_τ), we obtain $Y^E_{2,\tau\tau} = \sqrt{2(m_\tau^2 - |M^E_{\tau\mu}|^2)}/|v(s_\beta + c_\beta)|$, which implies that $|M^E_{\tau\mu}| \leq m_\tau$. Under the foregoing assumptions, the independent weak eigenbasis parameters are $|Y^E_{2,\tau\mu}|$, $\phi^E_{\tau\mu}$, $r_{\tau\mu}$ and β.

The other linear combination of the Yukawa matrices, $(-v_2 Y_1^E + v_1 Y_2^E)/\sqrt{2}$ generally cannot be simultaneously diagonalized and that couples to the Higgs basis neutral scalar $h_2 \equiv -\sin\beta\Phi_1^0 + \cos\beta\Phi_2^0$ that has no $T = 0$ vacuum expectation value (vev), in contrast to the state $h_1 \equiv \cos\beta\Phi_1^0 + \sin\beta\Phi_2^0$ whose vev is $v/\sqrt{2}$. The content of the physical neutral scalars h, H, and A^0 is determined by diagonalizing the scalar potential, assumed here to be CP-conserving, with corresponding mixing angle α. The resulting couplings to the τ lepton are given by

$$-\frac{1}{v}\overline{\tau_L}\tau_R[h(m_\tau s_{\beta-\alpha} + N^E_{\tau\tau} c_{\beta-\alpha}) + H(m_\tau c_{\beta-\alpha} - N^E_{\tau\tau} s_{\beta-\alpha}) + iA_0 N^E_{\tau\tau}] + \text{h.c.}, \tag{5.5}$$

where the angle $(\beta - \alpha)$ is invariant under Higgs doublet basis transformations [138] and the real and imaginary parts of $N^E_{\tau\tau}$ are related to the corresponding parts of J_E,

$$\begin{aligned}
\mathrm{Re}(N^E_{\tau\tau}) &= \frac{v^2 \mu_{12}^{\mathrm{HB}} \mathrm{Re} J_E - 2\mu_{11}^{\mathrm{HB}} m_\tau^2}{2\mu_{12}^{\mathrm{HB}} m_\tau} \\
&\overset{\tan\beta=1}{=} \frac{v^2 |Y^E_{2,\tau\mu}|^2}{4m_\tau}(1 - r^2_{\tau\mu}), \\
\mathrm{Im}(N^E_{\tau\tau}) &= \frac{v^2 \mathrm{Im} J_E}{2m_\tau} = \frac{-v^2 Y^E_{2,\tau\mu} \mathrm{Im} Y^E_{1,\tau\mu}}{2m_\tau} \quad . \qquad (5.6)
\end{aligned}$$

Since physical quantities are independent of the choice of Higgs basis and thus $\tan\beta$, we will eventually work with $\tan\beta = 1$ for convenience (indicated by the second line above) while keeping the following expressions largely general. The off-diagonal element $N^E_{\tau\mu}$ controls the strength of the Higgs CLFV couplings

$$-\frac{N^E_{\tau\mu}}{v}\overline{\tau_L}\mu_R(c_{\beta-\alpha}h - s_{\beta-\alpha}H + iA_0) + \mathrm{h.c.}, \qquad (5.7)$$

and its expression in terms of weak basis parameters is

$$N^E_{\tau\mu} = e^{i\delta}\left| N^E_{\tau\tau}\frac{M^E_{\tau\tau}}{M^E_{\tau\mu}}\right|, \qquad (5.8)$$

where δ is an arbitrary, un-physical phase undetermined from the diagonalization procedure that can be removed by a field redefinition. Finally the charged Higgs interactions are governed by $-\sqrt{2}/vH^+\overline{\nu^i_L}N^E_{ij}e^j_R + \mathrm{h.c.}$.

5.2 Phenomenology and the BAU.

We will express the various phenomenological constraints and implications of the BAU in terms of the effective $h\bar{\tau}\tau$ coupling [49]

$$-\frac{m_\tau}{v}(\mathrm{Re} y_\tau \bar{\tau}\tau + \mathrm{Im} y_\tau \bar{\tau} i\gamma_5 \tau)h \qquad (5.9)$$

with $\mathrm{Re}y_\tau \equiv \kappa_\tau \cos\phi_\tau$ and $\mathrm{Im}y_\tau \equiv \kappa_\tau \sin\phi_\tau$. In the transformation from the weak basis parameters to mass basis parameters, the condition $|M^E_{\tau\mu}| \le m_\tau$ imposes a strong constraint in the ($\mathrm{Re}y_\tau$, $\mathrm{Im}y_\tau$) plane in Fig. 5.1, allowing only the interior of a circular region plane centered at $\mathrm{Re}y_\tau = s_{\beta-\alpha} + c_{\beta-\alpha}(1+r^2_{\tau\mu})/(1-r^2_{\tau\mu})$, $\mathrm{Im}y_\tau = 0$ with radius $2|c_{\beta-\alpha} r_{\tau\mu}/(1-r^2_{\tau\mu})|$. For $r_{\tau\mu} = 1$, $N^E_{\tau\tau}$ is purely imaginary and corresponds to a vertical line at $\mathrm{Re}y_\tau = s_{\beta-\alpha}$. Moreover, for a given $r_{\tau\mu}$, the three mass basis parameters are not all independent. For example, inverting Eq. (5.6), we can solve for $|Y^E_{2,\tau\mu}|$ and $\sin\phi^E_{\tau\mu}$ as functions of $\mathrm{Re}N^E_{\tau\tau}$ and $\mathrm{Im}N^E_{\tau\tau}$. Eq. (5.8) then implies that rates for CLFV interactions like $h \to \tau\mu$ and $\tau \to \mu\gamma$ depend on $\Gamma(h \to \tau\tau)$.

5.3 Higgs signal strength measurement.

Measurements of the Higgs signal strength in the $\tau\tau$ channel, $\mu^{\tau\tau}$, constrain $N^E_{\tau\tau}$, which enters the $h \to \tau^+\tau^-$ decay rate via Eq. (5.5):

$$\Gamma^{\tau\tau} = \frac{\sqrt{2} G_F m_h}{8\pi} |m_\tau s_{\beta-\alpha} + c_{\beta-\alpha} N^E_{\tau\tau}|^2. \tag{5.10}$$

Experimentally, ATLAS gives $\mu^{\tau\tau}_{\mathrm{ATLAS}} = 1.43^{+0.43}_{-0.37}$ [7] while CMS favors a smaller one $\mu^{\tau\tau}_{\mathrm{CMS}} = 0.78 \pm 0.27$ [80]. We combine these two measurements by centralizing the errors of ATLAS, assuming both to be Gaussian distributed, neglecting their correlations and defining a χ^2 to obtain the 95%C.L. limit. The allowed parameter space from this constraint corresponds to annular regions between the green dashed lines in Fig. 5.1. A future determination of this coupling that agrees with the SM value within 10% is plotted as the inner sky blue band. The green regions that correspond to the intersection of above bands with the two circular regions from $|M^E_{\tau\mu}| \le m_\tau$ are the $\mu^{\tau\tau}$ constraint for $r_{\tau\mu} = 0.9$(left) and $r_{\tau\mu} = 1.1$(right).

5.4 Constraints from measurement of Br$(h \to \tau\mu)$.

The flavor off-diagonal $N^E_{\tau\mu}$ generates $h \to \tau\mu$ with width

$$\Gamma^{\tau\mu} = \frac{\sqrt{2}c^2_{\beta-\alpha}G_F m_h}{8\pi}|N^E_{\tau\mu}|^2 \quad . \tag{5.11}$$

ATLAS sets an upper limit on the corresponding branching ratio of Br$(h \to \tau\mu) <$ 1.43% at 95C.L. [9], while CMS gives a best fit Br$(h \to \tau\mu) = 0.84^{+0.39}_{-0.37}\%$ as well as an upper limit Br$(h \to \tau\mu) <$ 1.51% at 95% C.L. [163]. For a given value of $r_{\tau\mu}$, Br$(h \to \tau\mu)$ is correlated with $\Gamma(h \to \tau\tau)$ via Eqs. (5.4, 5.6, 5.8). This correlation is given by the brown arcs in in Fig. 5.1 for $r_{\tau\mu} = 0.9$ and $r_{\tau\mu} = 1.1$. The current ATLAS upper limit 1.43% as well as two prospective future results with upper bounds 1%, 0.5% are labeled as dashed lines while the circular boundaries give zero branching ratio. Moreover the branching ratio 1.41% is the value at the center of the left circular region.

5.5 The rare decay $\tau \to \mu\gamma$.

The flavor off-diagonal couplings (5.7) and their charge changing counterparts also contribute to the rare decay $\tau \to \mu\gamma$. The current experimental limit is Br$(\tau \to \mu\gamma) <$ 4.4×10^{-8} (90% C.L.) [29]. Theoretically, one has

$$\mathrm{Br}(\tau \to \mu\gamma) = \frac{\tau_\tau \alpha G_F^2 m_\tau^5}{32\pi^4}(|C_{7L}|^2 + |C^2_{7R}|), \tag{5.12}$$

where $\tau_\tau = (290.3 \pm 0.5) \times 10^{-15}s$ [193] is the τ lifetime and $C_{7L/R}$ are the Wilson coefficients of the two dipole operators

$$Q_7^{L/R} = \frac{e}{8\pi^2} m_\tau \bar{\mu}\sigma^{\mu\nu}(1 \mp \gamma^5)\tau F_{\mu\nu}, \tag{5.13}$$

defined by the effective Hamiltonian $-G_F[C_{7L}Q_7^L + C_{7R}Q_7^R]/\sqrt{2}$[63]. They receive contributions from one loop neutral and charged Higgs mediated diagrams and two loop

Barr-Zee type diagrams [40]. Results for the latter contributions have been adapted from the calculations in Ref. [73, 11, 146, 58]. We find that C_{7L} is proportional to $N^{E}_{\tau\mu}{}^{*}$ while $C_{7R} \propto N^{E}_{\mu\tau}$, which vanishes for our choice of Yukawa texture. The gray region in Fig. 5.1 is consistent with this bound and the aforementioned constraints.

5.6 Electric and magnetic dipole moments.

In principle, measurements of the muon anomalous magnetic moment and upper bounds on the electron electric dipole (EDM) moment provide additional constraints (those for the τ are less constraining). The one loop contributions to muon dipole come from exchanges of the neutral scalars and are proportional to the invariant $N^{E}_{\tau\mu}N^{E}_{\mu\tau}$, which vanishes for our choice of Yukawa texture. The two loop Barr-Zee type diagrams have similar topology as for the $\tau \to \mu\gamma$ amplitude but their contributions to the muon dipole moments all vanish due to the vanishing $h_a\bar{\mu}\mu$, $H^{+}\bar{\nu}_{\mu}\mu$ couplings on the lower leg of the diagrams. The two-loop electron EDM is dominated by the exchange of h, whose coupling to the electron is proportional to y_e in the alignment limit. We find that $|d_e/e| \approx 1.57 \times 10^{-25}\,|\mathrm{Im}y_\tau|$cm, implying that $|\mathrm{Im}y_\tau| < 5.53$ in order to be consistent with the present electron EDM upper bound[39].

5.7 Collider probes of a CP-violating $h\bar{\tau}\tau$ coupling

. Im J_E represents a different source of CPV compared to the case where a CPV $h\bar{\tau}\tau$ coupling results from mixing between CP-even and CP-odd Higgs scalars. The latter would originate from CPV in the potential which is highly constrained by EDM limits [147]. Studies of collider sensitivities of a CPV $h\bar{\tau}\tau$ coupling employing the ρ-meson decay plane method and the impact parameter method show that the phase ϕ_τ can be determined with an uncertainty of $15^\circ(9^\circ)$ at the LHC with an integrated luminosity of $150\text{fb}^{-1}(500\text{fb}^{-1})$ while $\approx 4^\circ$ with $3\,\text{ab}^{-1}$ can be achieved [49]. At Higgs factories, this phase may be measured with ≈ 4.4° accuracy with a 250 GeV run and $1\,\mathrm{ab}^{-1}$ luminosity [142].

5.8 Electroweak baryogenesis.

The first order EWPT proceeds via bubble nucleation. CPV scattering from the bubble walls generates a net left-handed fermion density n_L, whose diffusion ahead of the advancing wall biases the electroweak sphalerons into producing a net baryon number density, n_B. The expanding bubbles capture and preserve this density if the sphaleron processes are sufficiently quenched inside the bubbles. We compute n_L from a set of quantum transport equations, derived from the equations of motion for Wightman functions arising in the closed time path formulation of non-equilibrium quantum field theory by expanding in gradients of the bubble wall profile and chemical potentials (see Ref. [174] for pedagogical discussions). As with earlier work, we will employ the "vev insertion approximation", which provides a reasonable estimation of the CPV sources (see Ref. [192] for a discussion of theoretical issues associated with the computation of these sources). Since the weak sphaleron rate Γ_{ws} [55, 182, 168, 187] is much smaller than the rates for diffusion and particle number changing reactions that govern n_L [87], we first solve for this density and substitute the result into the equation for n_B.

For simplicity, we neglect bubble wall curvature [94], so that the the quantities entering the quantum transport equations depend only on the coordinate in the bubble wall rest frame $\bar{z} = z + v_w t$ with v_w being the wall velocity, $\bar{z} > 0$ corresponding to broken phase and $\bar{z} < 0$ for unbroken phase. Since non-zero densities for the first and second generation quarks as well as for the bottom quark are generated only by strong sphaleron processes, the following relations hold: $Q_1 = Q_2 = -2U = -2D = -2C = -2S = -2B$, where Q_k denotes the density of left-handed quarks of generation k and U, D, *etc.* denote the corresponding right-handed quark densities. In addition,

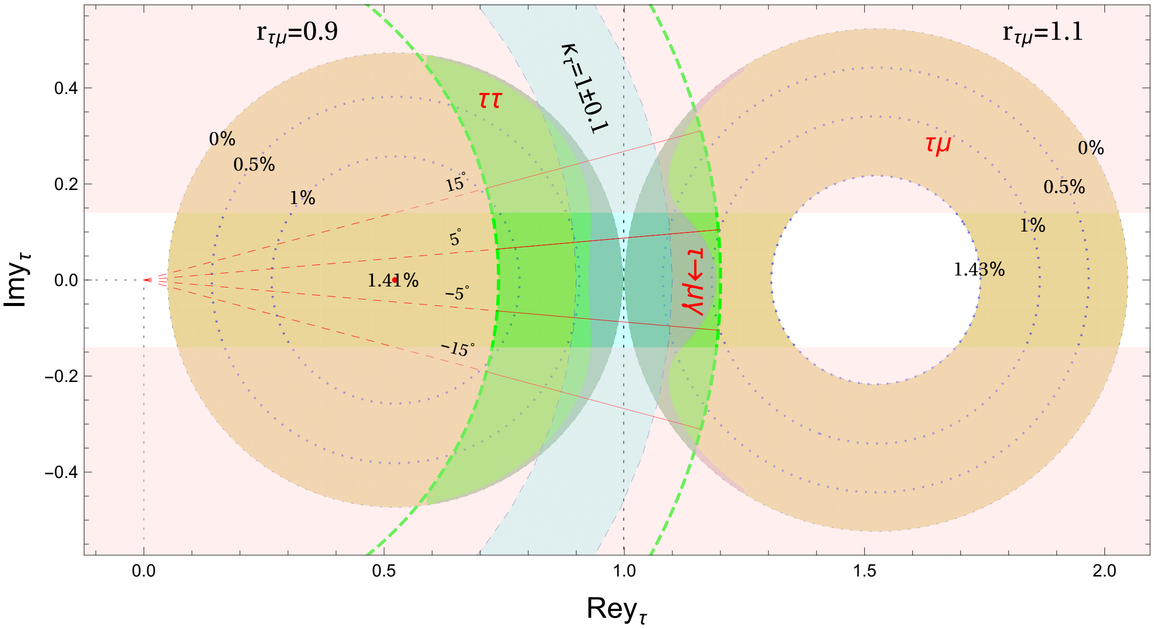

Figure 5.1: Allowed regions in the $(\mathrm{Re}y_\tau, \mathrm{Im}y_\tau)$ plane from $h \to \tau\mu$(brown, ATLAS bound $\mathrm{Br}(h \to \tau\mu) \le 1.43\%$ at 95%CL), $h \to \tau\tau$(green, 95% CL), $\tau \to \mu\gamma$(gray, 90% CL) and BAU(pink bands, $|\Delta\beta| \le 0.4$) for $\beta - \alpha - \frac{\pi}{2} = 0.05$, $r_{\tau\mu} = 0.9$(then $\mathrm{Re}y_\tau \lesssim 1$) and $r_{\tau\mu} = 1.1$(then $\mathrm{Re}y_\tau \gtrsim 1$). The $r_\tau = 0.9$ and $r_{\tau\mu} = 1.1$ regions are separated by the vertical dashed line at $\mathrm{Re}y_\tau = \sin(0.05 + \frac{\pi}{2}) \approx 1$. Several branching ratios of $h \to \tau\mu$: 1.43%, 1.41%(center of left circle), 1%, 0.5% and 0% are shown with circular dashed lines inside the brown arcs. The inner parts of circular regions satisfy the diagonalization constraint $|M^E_{\tau\mu}| \le m_\tau$ with their outer boundaries giving vanishing $\tau \to \mu\gamma$ and $h \to \tau\mu$. The region inside the green dashed lines is allowed at 95%CL by Higgs signal strength $\mu^{\tau\tau}$ measurements without assuming a specific Yukawa texture. The inner light-blue band labelled $\kappa_\tau = 1 \pm 0.1$ corresponds to the allowed region for a more SM-like $h\bar{\tau}\tau$ coupling. The angles $\phi_\tau = \pm 15\%, \pm 5\%$ are shown. The other parameters are fixed to be $m_H = 400\mathrm{GeV}$, $m_{A^0} = 600\mathrm{GeV}$ and $m_{H^\pm} = 500\mathrm{GeV}$, $v_w = 0.05$, $L_W = 2/T$, $D_q = 6/T$ and $T = 100\mathrm{GeV}$.

$E_1 = E_2 = e_R \approx 0$ since the corresponding leptonic Yukawa interactions are negligible compared to those retained in our choice of Yukawa texture. Local baryon number density is also approximately conserved on the time scales relevant to the reactions that govern n_L, so that $\sum_{i=1}^{3}(Q_i + U_i + D_i) = 0$. The resulting transport equations are

$$\begin{aligned}
\partial_\mu Q_3^\mu &= \Gamma_{mt}(\xi_T - \xi_{Q_3}) + \Gamma_t(\xi_T - \xi_H - \xi_{Q_3}) \\
&\quad +2\Gamma_{ss}\delta_{ss}, \\
\partial_\mu H &= \Gamma_t(\xi_T - \xi_H - \xi_{Q_3}) + \Gamma_\tau(\xi_{E_3} - \xi_{\tau_R} - \xi_H) \\
&\quad -2\Gamma_h \xi_H, \\
\partial_\mu E_3^\mu &= -\Gamma_{m\tau}(\xi_{E_3} - \xi_{\tau_R}) - \Gamma_\tau(\xi_{E_3} - \xi_{\tau_R} - \xi_H) \\
&\quad +S_{\tau_L}^{\not{C}P}, \\
\partial_\mu {\tau_R}^\mu &= -\Gamma_\tau(\xi_H + \xi_{\tau_R} - \xi_{E_3}) + \Gamma_{m\tau}(\xi_{E_3} - \xi_{\tau_R}) \\
&\quad +S_{\tau_R}^{\not{C}P}, \\
\partial_\mu T^\mu &= -\Gamma_{mt}(\xi_T - \xi_{Q_3}) - \Gamma_t(\xi_T - \xi_H - \xi_{Q_3}) \\
&\quad -\Gamma_{ss}\delta_{ss}, \\
\partial_\mu \mu_R^\mu &= S_{\mu_R}^{\not{C}P},
\end{aligned} \tag{5.14}$$

where $\delta_{ss} = \xi_T + 9\xi_B - 2\xi_{Q_3}$, $\xi_a = n_a/k_a$, with k_a being the statistical weight [174] associated with the number density n_a of species "a" and $\partial_\mu \approx v_w \frac{d}{d\bar{z}} - D_a \frac{\partial^2}{d\bar{z}^2}$ with D_a being the diffusion constant [156] from the diffusion approximation. The CPV source terms are

$$S_{\tau_L}^{\not{C}P} = -S_{\mu_R}^{\not{C}P} = \frac{v^2(\bar{z}) v_w \frac{d\beta(\bar{z})}{d\bar{z}} \mathrm{Im} J_E}{2\pi^2} \mathcal{I} \ , \tag{5.15}$$

where $\mathcal{I}$ is a momentum-space integral that depends on the leptonic thermal masses (see Ref. [176]) and $d\beta/d\bar{z}$ characterizes the local variation of $\tan\beta(\bar{z})$ as one moves across the bubble wall. Note that $S_{\tau_R}^{C\!\!/P} = 0$ due to the vanishing Yukawa texture in the first row of $Y_{1,2}^E$. Furthermore $\Gamma_{ss} \approx 16\alpha_s^4 T$ is the strong sphaleron rate [130]; Γ_{mt} is the two body top relaxation rate [174]; and $\Gamma_{t/\tau}$ is the t/τ Yukawa induced three body rate [92]. After solving for the densities in Eqs. (5.14), we obtain $n_L = \sum_i (Q_i + E_i)$ [71] and n_B, which is a constant in the broken phase:

$$n_B = \frac{3\Gamma_{\text{ws}}}{D_q \lambda_+} \int_0^{-\infty} n_L(\bar{z}) e^{-\lambda_- \bar{z}} d\bar{z} \quad , \tag{5.16}$$

where $\Gamma_{\text{ws}} \approx 120\alpha_w^5 T$ [55] and $\lambda_\pm = (v_w \pm \sqrt{v_w^2 + 15\Gamma_{\text{ws}} D_q})/(2D_q)$.

Assuming a fast τ_R diffusion [88], we solve the transport equations perturbatively at the leading order of Γ_t^{-1}, Γ_y^{-1}, Γ_τ^{-1} and Γ_{ss}^{-1}. We further neglected $\Gamma_{m\tau}$ in the final result as it is generally small compared with Γ_{mt} and then n_B is proportional to $\text{Im}y_\tau$ with no dependence on $\text{Re}y_\tau$. Doing this would allow us to show the generic constraint from BAU for the whole parameter space without being restricted in the circular regions corresponding to a specific $r_{\tau\mu}$. Furthermore in the calculation of n_B, the most important uncertainty is the difference of $\beta(\bar{z})$ in the broken and symmetric phases($\equiv \Delta\beta$) since the CPV source term and thus n_B are both directly proportional to it. Due to the so far absence of its calculations, we take its maximum magnitude to be 0.4 and vary it to obtain the bands in Fig. 5.1 where the upper and lower bands give opposite signs of BAU resulting from the unknown sign of $\Delta\beta$.

Taking into account the previously discussed phenomenological constraints, a BAU consistent with all observations can be obtained for $|\phi_\tau| \gtrsim 7^\circ$ which can be probed at colliders as discussed before. One immediate and important implication is that $\text{Br}(h \to \tau\mu) \lesssim 0.5\%$ and a larger CP-violating $h\bar{\tau}\tau$ would imply a smaller $\text{Br}(h \to \tau\mu)$. Also since the BAU constrains $\text{Im}y_\tau$ or ϕ_τ through the invariant,

$$\text{Im}J_E = \frac{2m_\tau \text{Im}N_{\tau\tau}^E}{v^2} = 2\frac{m_\tau^2}{v^2}\frac{\text{Im}y_\tau}{c_{\beta-\alpha}}, \tag{5.17}$$

thus, should future measurements imply that the Higgs leptonic interactions be even more SM-like with $\beta - \alpha$ closer to $\pi/2$, the minimally required $\text{Im}y_\tau$ or ϕ_τ would become smaller. This in turn needs $r_{\tau\mu}$ to be more closer to 1 to avoid shrinking of the region $|M^E_{\tau\mu}| \leq m_\tau$.

It needs to mention that there is still relatively large uncertainties with the BAU calculations [192, 174]. This necessitate in part the need of a dedicated analysis of the EWPT, precise determinations of the expanding bubble wall profiles [188, 184], a resummed vev insertion approximation [70, 169, 90, 91, 118], a more comprehensive definition of the transport equations from a more precise Yukawa texture including a clear identification of CPV origins incorporating extra CPV invariants [57] and these will be deferred to future works.

CHAPTER 6

TAU FLAVORED DARK MATTER

In chapter 6, we discussed the dark matter nucleon interactions with spin structures other than the SI and SD types and studied how the direct detection signals can be calculated. In this chapter, we are going to study a lepton flavored dark matter scenario where such interactions can arise and study its phenomenological implications. Flavored dark matter has been studied in various contexts [74, 66, 36, 75, 202, 17, 99, 32, 122, 31, 103, 82, 19, 67, 167, 173, 18, 16, 41, 165, 170, 166, 217, 81] and they can be used to explain the galactic center gamma ray excess [16] observed by the *Fermi-LAT* [12]. Moreover a common feature for the lepton flavored dark matter scenarios is that the dark matter nucleon interactions generally arise from loop level diagrams and thus have suppressed effect on direct detection cross sections. Thus these types of interactions can generally easily evade the direct detection null search limits while still be compatible with relic density requirements. We focus here on the tau flavored dark matter since this model would change the Yukawa interactions of Higgs to tau leptons and might explain the the discrepancy of the Higgs signal strengh in the $\tau\tau$ channel.

6.1 Model

We extend the SM with an inert scalar doublet, a singly charged scalar singlet and a Dirac dark matter, which is stabilized by a Z_2 discrete flavor symmetry, in which dark matter and the third generation leptons are odd while all other particles are even. In the following we first describe scalar interactions, then go to the dark matter interactions. The scalar potential can be written as

$$\begin{aligned} V &= -\mu^2 H^\dagger H + \lambda(H^\dagger H)^2 + m_1^2 \Phi^\dagger \Phi + \lambda_1(\Phi^\dagger\Phi)^2 + \lambda_2(\Phi^\dagger\Phi)(H^\dagger H) + \lambda_3(\Phi^\dagger H)(H^\dagger \Phi) \\ &\quad + m_2^2 S^+ S^- + \lambda_4 (S^+ S^-)^2 + \lambda_5 (S^+S^-)(H^\dagger H) + \lambda_6 (S^+ S^-)(\Phi^\dagger \Phi) \\ &\quad + \sqrt{2}\Lambda H^T \varepsilon \Phi S^- + \text{h.c.} \end{aligned} \tag{6.1}$$

where $H^T \equiv (G^+, (h + iG_0 + v)/\sqrt{2})$ is the SM Higgs, $v = 246$ GeV is the vacuum expectation value (VEV), $\Phi^T \equiv (\Phi^+, (\rho + i\eta)/\sqrt{2})$ is the inert scalar doublet, $S^\pm$ is the singly charged scalar singlet, Λ is certain energy scale. Assuming that the mass term of Φ is positive, it develops no VEV. As a result, there is no mixing between h and ρ. The masses of neutral scalars can be written as

$$m_h^2 = 2\lambda v^2 \, , \qquad m_\rho^2 = m_\eta^2 = m_1^2 + \frac{1}{2}(\lambda_2 + \lambda_3) v^2 \, . \tag{6.2}$$

Due to the last term in Eq. (6.1), there is mixing between Φ^+ and S^+. The relevant mass matrix is The corresponding mass eigenvalues are

$$\hat{m}_{1,2}^2 = \frac{1}{2}\left\{ m_1^2 + m_2^2 + \frac{1}{2}(\lambda_2 + \lambda_5)v^2 \pm \sqrt{\left[m_1^2 - m_2^2 + \frac{1}{2}(\lambda_2 - \lambda_5)v^2\right]^2 + 4(\Lambda v)^2} \right\} \tag{6.3}$$

and the relations between physical eigenstates and interaction eigenstates are $\Phi^+ = c_\theta \hat{\Phi}^+ + s_\theta \hat{S}^+$, $S^+ = -s_\theta \hat{\Phi}^+ + c_\theta \hat{S}^+$, where $c_\theta = \cos\theta$ and $s_\theta = \sin\theta$, with θ the rotation angle that diagonalizes the mass matrix in Eq.4.2.

We have the following set of free parameters: m_h, m_ρ, $\hat{m}_{1,2}$, θ, $\lambda_i (i = 1, 2, 4, 5, 6)$, and Λ. Not all of them are physical and their relations with the physical parameters are

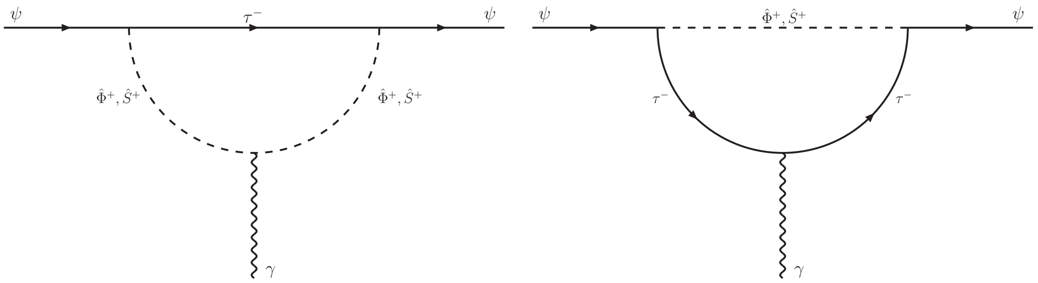

Figure 6.1: Feynman diagrams contributing to the dark matter electromagnetic form factors.

$$(A)\begin{cases} \mu^2 = 1/2m_h^2 \\ m_1^2 = \hat{m}_1^2 c_\theta^2 + \hat{m}_2^2 s_\theta^2 - 1/2\lambda_2 v^2 \\ m_2^2 = \hat{m}_1^2 s_\theta^2 + \hat{m}_2^2 c_\theta^2 - 1/2\lambda_5 v^2 \end{cases} \qquad (B)\begin{cases} \lambda \ = m_h^2 v^{-2}/2 \\ \Lambda = (\hat{m}_1^2 - \hat{m}_2^2) c_\theta s_\theta v^{-1} \\ \lambda_3 = 2v^{-2}[m_\rho^2 - (\hat{m}_1^2 c_\theta^2 + \hat{m}_2^2 s_\theta^2)] \end{cases} \tag{6.4}$$

Notice that in the parameter set we have chosen, $\lambda_1, \lambda_4, \lambda_6$ describe quartic interactions among these extra scalars and are not so relevant for the study in this paper. λ_2 and λ_5 are relevant for the $h\gamma\gamma$ and $h\bar{\tau}\tau$ couplings as will be seen in the next section.

We assume that dark matter only interacts with the new scalars and third generation leptons which can be written as

$$-\mathcal{L}_Y = \kappa_1 \overline{\ell_L^3} \tilde{\Phi} \psi + \kappa_2 \overline{\psi} S^+ \tau_R + \text{h.c.}\ , \tag{6.5}$$

where ℓ_L^3 is the third generation left-handed lepton doublet and ψ is the Dirac dark matter. As a result, the dark matter can only annihilate into $\bar{\tau}\tau$ and $\bar{\nu}_\tau \nu_\tau$. For the benefits of the direct detection, one needs to calculate the electromagnetic form factors of the dark matter, which arise at one loop level from the relevant penguin diagrams shown in Fig. 6.1. The induced effective dark matter-photon interactions are where b_ψ is the charge radius, c_ψ is the axial charge radius or anapole moment and μ_ψ is the magnetic moment. Since there is no CP violation in the dark matter sector, the electric dipole moment term is absent. We assume the following mass hierarchy

$m_\tau \ll m_\psi < \hat{m}_{1,2}, m_{\rho,\eta}$. Besides the typical momentum transfer of DM-Nucleon interactions is about 50MeV, thus the momentum transfer, $\sqrt{-q^2}$, is far smaller than the τ mass and constitutes the smallest scale. Collecting all the contributing diagrams and expanding in terms of q^2, we obtain

$$\begin{aligned}
\mu_\psi &= \sum_{i=1}^{2} -\frac{e m_\psi \zeta_i}{64\pi^2} \int_0^1 dx \frac{x(1-x)}{\Delta_i} \,, \\
b_\psi &= \sum_{i=1}^{2} \frac{e\zeta_i}{32\pi^2} \int_0^1 dx \left\{ \frac{x^3 - 2(1-x)^3}{6\Delta_i} + \frac{(x-1)^3(x^2 m_\psi^2 + m_\tau^2) + 2(1-x)x^4 m_\psi^2}{6\Delta_i^2} \right\}, \\
c_\psi &= \sum_{i=1}^{2} \frac{e\hat{\zeta}_i}{192\pi^2} \int_0^1 dx \left\{ \frac{(-3x^3 + 6x^2 - 6x + 2)x\hat{m}_i^2 + (-2x^4 + 6x^3 - 9x^2 + 7x - 2)x m_\psi^2}{\Delta_i^2} \right\},
\end{aligned} \tag{6.6}$$

where m_ψ is the dark matter mass, $\zeta_1 = c_\theta^2\kappa_1^2 + s_\theta^2\kappa_2^2$, $\zeta_2 = s_\theta^2\kappa_1^2 + c_\theta^2\kappa_2^2$, $\hat{\zeta}_1 = c_\theta^2\kappa_1^2 - s_\theta^2\kappa_2^2$, $\hat{\zeta}_2 = s_\theta^2\kappa_1^2 - c_\theta^2\kappa_2^2$, and $\Delta_i = x\hat{m}_i^2 + x(x-1)m_\psi^2 + (1-x)m_\tau^2$. We have ignored terms proportional to $\mathcal{O}(m_\tau^2)$ in Eg. (6.6). Note that the limit $m_\psi, m_\tau \ll \hat{m}_{1,2}$ allows us to recover the familiar result [74, 141]

$$b_\psi = \sum_i \frac{e\zeta_i^2}{64\pi^2\hat{m}_i^2}\left(1 + \frac{2}{3}\ln\frac{m_\tau^2}{\hat{m}_i^2}\right), \tag{6.7}$$

where m_τ serves as an infrared regulator.

Similarly there are also form factors for the effective dark matter-Z boson interactions. The contribution of these interactions to the dark matter-nuclei scattering cross section is subdominant compared with those arising from electromagnetic form factors. So we neglect these interactions in our calculation.

6.2 Phenomenology

We will study in this section phenomenologies arising from this model, including the dark matter relic density, signatures in direct detections, the loop induced τ lepton mass, the effective coupling of $h\bar{\tau}\tau$ as well as the Higgs to diphoton decay rate. Finally we will discuss signatures of our model at colliders.

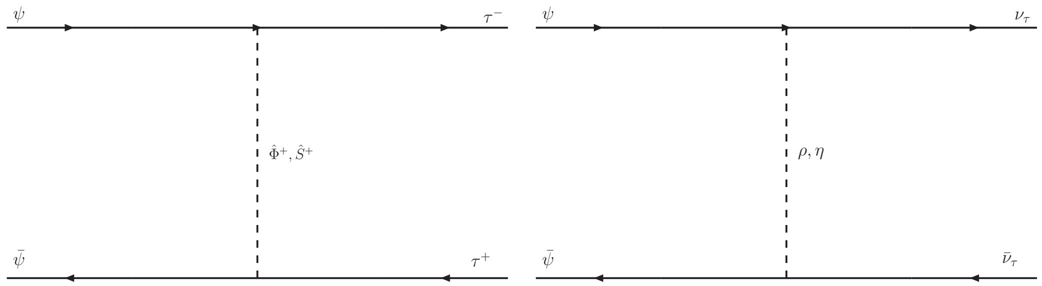

Figure 6.2: Dark matter annihilation channels.

6.2.1 Relic density

We have assumed that the dark matter is a Dirac fermion and only interacts with the third generation leptons in our model. It annihilates into $\bar{\tau}\tau/\bar{\nu}_\tau\nu_\tau$ with the relevant Feynman diagrams shown in Fig. 6.2. The cold dark matter was in local thermodynamic equilibrium in the early Universe. When its interaction rate drops below the expansion rate of the Universe, the dark matter is said to be decoupled. The evolution of the dark matter number density n, is governed by the Boltzmann equation [132]:

$$\dot{n} + 3Hn = -\langle \sigma v_{\mathrm{M\o ller}} \rangle (n^2 - n_{\mathrm{EQ}}^2) \ , \tag{6.8}$$

where H is the Hubble constant, $\sigma v_{\mathrm{M\o ller}}$ is the total annihilation cross section multiplied by the M$\o$ller velocity with $v_{\mathrm{M\o ller}} = (|v_1 - v_2|^2 - |v_1 \times v_2|^2)^{1/2}$, brackets denote thermal average and n_{EQ} is the number density in thermal equilibrium. It has been shown that $\langle \sigma v_{\mathrm{M\o ller}} \rangle = \langle \sigma v_{\mathrm{lab}} \rangle = 1/2[1 + K_1^2(x)/K_2^2(x)] \langle \sigma v_{\mathrm{cm}} \rangle$ [132], where $x = m_{\mathrm{DM}}/T$ and $K_i(x)$ is the modified Bessel functions of the i-th order. To derive the relic density of the tau flavored dark matter, one needs to calculate the thermal average of the total annihilation cross section. Analytically one can approximate the thermal average $\langle \sigma v \rangle$ with the non-relativistic expansion $\langle \sigma v \rangle = a + b \langle v^2 \rangle$ in the lab frame,

$$\begin{aligned}\langle\sigma v\rangle &= \sum_{i=1}^{4}\zeta_i^2\left(\frac{m_\psi^2}{32\pi(m_\psi^2+\hat{m}_i^2)^2}+\langle v^2\rangle\frac{m_\psi^2(-7m_\psi^4-18m_\psi^2\hat{m}_i^2+\hat{m}_i^4)}{384\pi(m_\psi^2+\hat{m}_i^2)^4}\right)+\\ &\quad \frac{1}{4}s_{2\theta}^2(\kappa_1^2-\kappa_2^2)^2\left(\frac{m_\psi^2}{16\pi(\hat{m}_1^2+m_\psi^2)(\hat{m}_2^2+m_\psi^2)}+\frac{\langle v^2\rangle\Delta}{192\pi(\hat{m}_1^2+m_\psi^2)^3(\hat{m}_2^2+m_\psi^2)^3}\right)\\ &\equiv a+b\langle v^2\rangle, \end{aligned} \tag{6.9}$$

where

$$\begin{aligned}\Delta &= -m_\psi^2\left(7m_\psi^8+16m_\psi^6(\hat{m}_1^2+\hat{m}_2^2)+m_\psi^4(5\hat{m}_1^4+32\hat{m}_1^2\hat{m}_2^2+5\hat{m}_2^2)\right.\\ &\quad \left.+8m_\psi^2\hat{m}_1^2\hat{m}_2^2(\hat{m}_1^2+\hat{m}_2^2)-\hat{m}_1^4\hat{m}_2^4\right). \end{aligned} \tag{6.10}$$

Here $\zeta_{1,2}$ were defined below Eq. (6.6) and $\zeta_{3,4}=\sqrt{2}\kappa_1^2$. The notation $\hat{m}_i$, where $i=1,2,3,4$, denotes the mass of $\hat{\Phi}^+$, $\hat{S}^+$, ρ and η respectively.

The present relic density of the DM is simply given by $\rho_{\rm DM}=m_{\rm DM}n_{\rm DM}=m_{\rm DM}s_0Y_\infty$ [51], where s_0 is the present entropy density. The relic abundance can be written in terms of the critical density

$$\Omega h^2 \approx 2\times\frac{1.07\times10^9}{M_{\rm pl}}\frac{x_F}{\sqrt{g_*}}\frac{1}{a+3b/x_F}, \tag{6.11}$$

where a and b were defined in Eq. (6.9), $M_{\rm pl}$ is the Planck mass, $x_F=m_{\rm DM}/T_F$ with T_F being the freezing out temperature of the dark matter, g_* is the degrees of freedom at the freeze out temperature and the factor 2 on the right-hand side accounts for the fact that dark matter in our model is a Dirac fermion.

The dark matter relic density measured by the Planck experiment is $\Omega h^2 = 0.1199\pm0.0022$ [14]. To see its constraints on the parameter space, we plot in Fig. 6.3 (a) contours of the dark matter relic density requiring the relic density to be within two standard deviations of the measured central value in the $\kappa_1-\kappa_2$ plane by setting $\hat{m}_1=400$ GeV, $\hat{m}_2=600$ GeV and $m_\rho=m_\eta=700$ GeV. The red, yellow, blue,

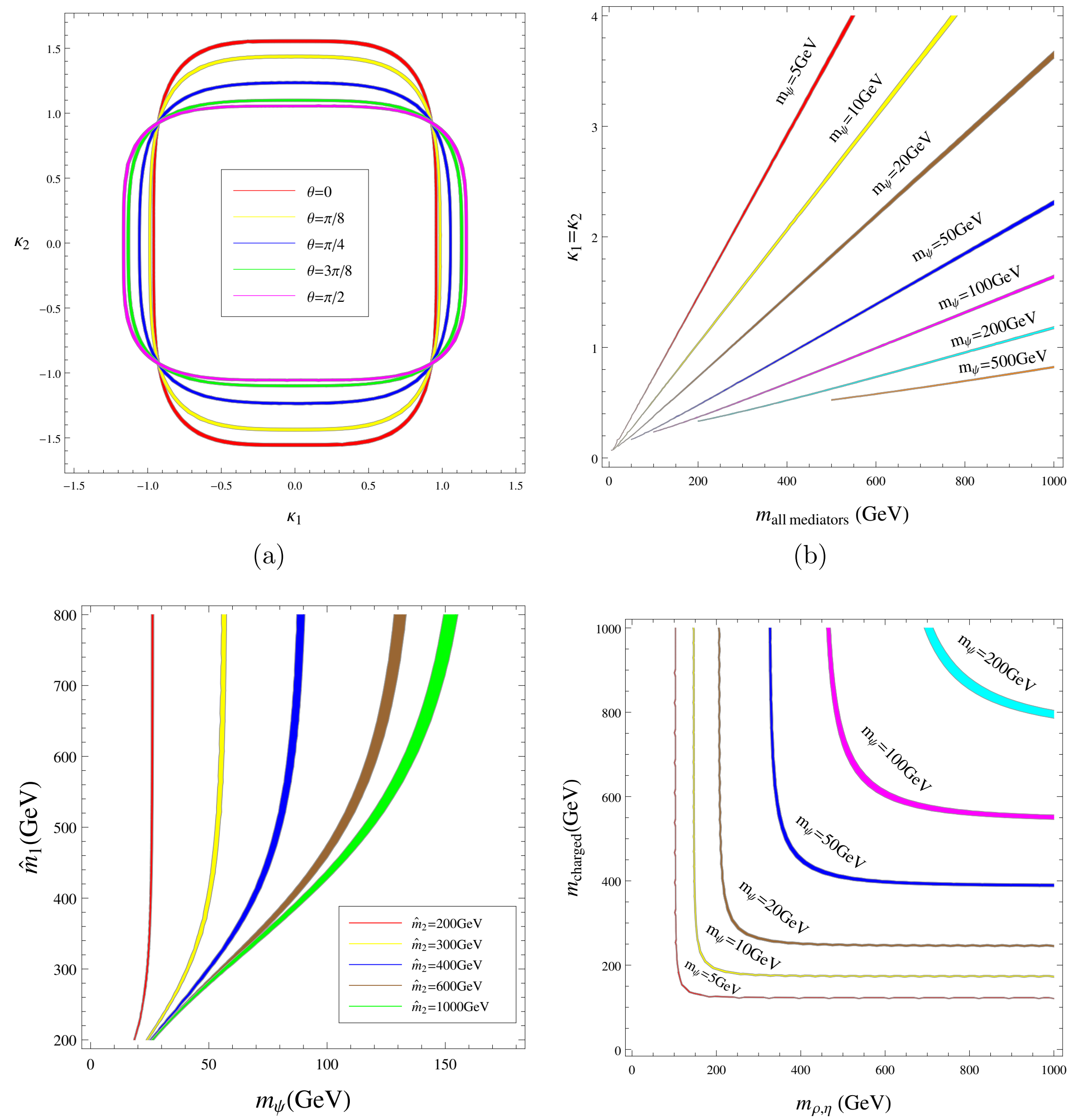

(a) (b)

(c) (d)

Figure 6.3: The contours of the relic density within two standard deviations of the measured value: In Fig. (a), we show contours in $\kappa_1 - \kappa_2$ plane with different inputs of mixing angle θ, by setting $m_\psi = 100$ GeV, $\hat{m}_1 = 400$ GeV, $\hat{m}_2 = 600$ GeV and $m_\rho = m_\eta = 700$ GeV; In Fig. (b), we show contours in the $\kappa_1 - m_{\text{all mediators}}$ plane for different dark matter masses, by assuming all mediators have the same mass and $\kappa_1 = \kappa_2$; Fig.(c) show contours in the $\hat{m}_1$ - m_ψ plane for different values of $\hat{m}_2$, by setting $\kappa_1 = \kappa_2 = 1$ and $m_\rho = m_\eta = 700$ GeV; In Fig. (d), we set $\kappa_1 = \kappa_2 = 1$ and plot charged mediator versus neutral mediator masses for several dark matter masses.

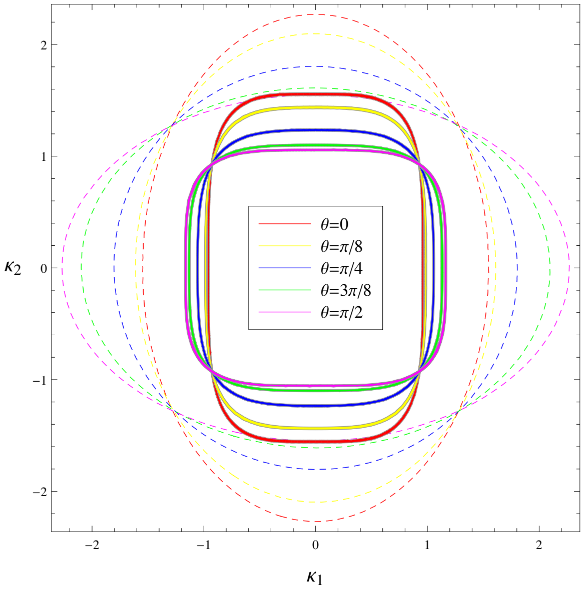

Figure 6.4: LUX limit as a dashed line for each solid relic density contour in the κ_1, κ_2 plane for different θ. Relic density contours are within two standard deviations of the Planck measured central value and regions outside the dashed lines are excluded at 95% C.L. by the LUX. The other parameters are fixed to be $m_\psi = 100$ GeV, $\hat{m}_1 = 400$ GeV, $\hat{m}_2 = 600$ GeV, $m_\rho = m_\eta = 700$ GeV and $\lambda_2 = \lambda_5 = 0$.

green and pink contours correspond to $\theta = 0,\ \pi/8,\ \pi/4,\ 3\pi/8$ and $\pi/2$ respectively. One has $\kappa_{1,2} \in [-1.5,\ 1.5]$ and κ_1, κ_2 can not both take small values to give rise to a correct dark matter relic density. By assuming $\kappa_1 = \kappa_2$ and degenerate mediator masses, we show in Fig. 6.3 (b) contours of the dark matter relic density, with the red, yellow, brown, blue, magenta, cyan and orange colored contours corresponding to $m_\psi = 5$ GeV, 10 GeV, 20 GeV, 50 GeV, 100 GeV, 200 GeV and 500 GeV respectively. It shows that the heavier the dark matter is, the larger the annihilation cross section will be, such that larger mediator masses or smaller couplings will be required to get a correct relic density. This can also be seen from Fig. 6.3 (c) and (d), where we show the correlation between the dark matter mass and the charged mediator masses (Fig. 6.3 (c)) as well as the correlation between the neutral mediator masses and charged mediator masses (Fig. 6.3 (d)). For the input of other parameters of Fig. 6.3 (c) and (d) see the caption for details.

6.2.2 Direct detection

Notice that flavored dark matter models may help to release the tension between the observed dark matter relic density and constraints from direct detections, which detect dark matter scattering from nuclei in underground laboratories. In our model, dark matter couples to nucleons at loop level through induced electromagnetic form factors of the dark matter as well as loop induced dark matter-Higgs interactions. The effective interactions of the dark matter with nucleon take the following form [74, 141, 145]

$$f_r\bar{\psi}\gamma^{\mu}\psi\bar{N}\gamma_{\mu}N + f_h\bar{\psi}\psi\bar{N}N + f_m^1\bar{\psi}i\sigma^{\mu\nu}\psi\frac{q_\nu}{q^2}\bar{N}K_{\mu}N + f_m^2\bar{\psi}i\sigma^{\alpha\mu}\psi\frac{q_\alpha q_\beta}{q^2}\bar{N}i\sigma^{\beta\mu}N \tag{6.12}$$

with q^μ being the momentum transfer from nucleon to dark matter and K^μ defined as the summation of momenta of incoming and outgoing nucleon. The Wilson coefficients are given by

$$f_r^N = eQ_N b_\psi\ , \quad f_h^N = f_\psi^h\frac{m_N}{m_h^2 v}\left(\sum_{q=u,d,s} f_{T_q}^N + \frac{2}{9}f_{TG}^N\right)\ , \quad f_m^1 = \frac{eQ_N\mu_\psi}{2m_N}\ , \quad f_m^2 = -\frac{e\tilde{\mu}_N\mu_\psi}{2m_N},$$

where Q_N is the charge of the nucleon, μ_ψ and b_ψ are the magnetic moment and charge radius of the dark matter respectively, $\tilde{\mu}_N$ is the nucleon magnetic moment, that is, $\tilde{\mu}_p \approx 2.80$ and $\tilde{\mu}_n \approx -1.91$. Finally f_ψ^h is the effective dark matter-Higgs coupling with the result given by

$$f_\psi^h = \sum_{ij=1}^{2}\frac{c_{ij}m_\psi}{32\pi^2}\int_0^1 dx\int_0^{1-x}dy\frac{1-x}{(1-x-y)\hat{m}_i^2 + y\hat{m}_j^2 + (x^2-x)m_\psi^2}, \tag{6.13}$$

where $c_{11} \approx \zeta_1 v(\lambda_2 c_\theta^2 + \lambda_5 s_\theta^2 + 2\Lambda s_\theta c_\theta/v)$, $c_{22} \approx \zeta_2 v[\lambda_2 s_\theta^2 + \lambda_5 c_\theta^2 - 2\Lambda s_\theta c_\theta/v)]$, $c_{12} = c_{21} = s_\theta c_\theta(\kappa_1^2 - \kappa_2^2)[v s_\theta c_\theta(\lambda_5 - \lambda_2) + \Lambda c_{2\theta}]$ and x, y are Feynman parameters. We have neglected the Z mediated interactions in Eq.(6.12) since it is subdominant compared with photon mediated processes.

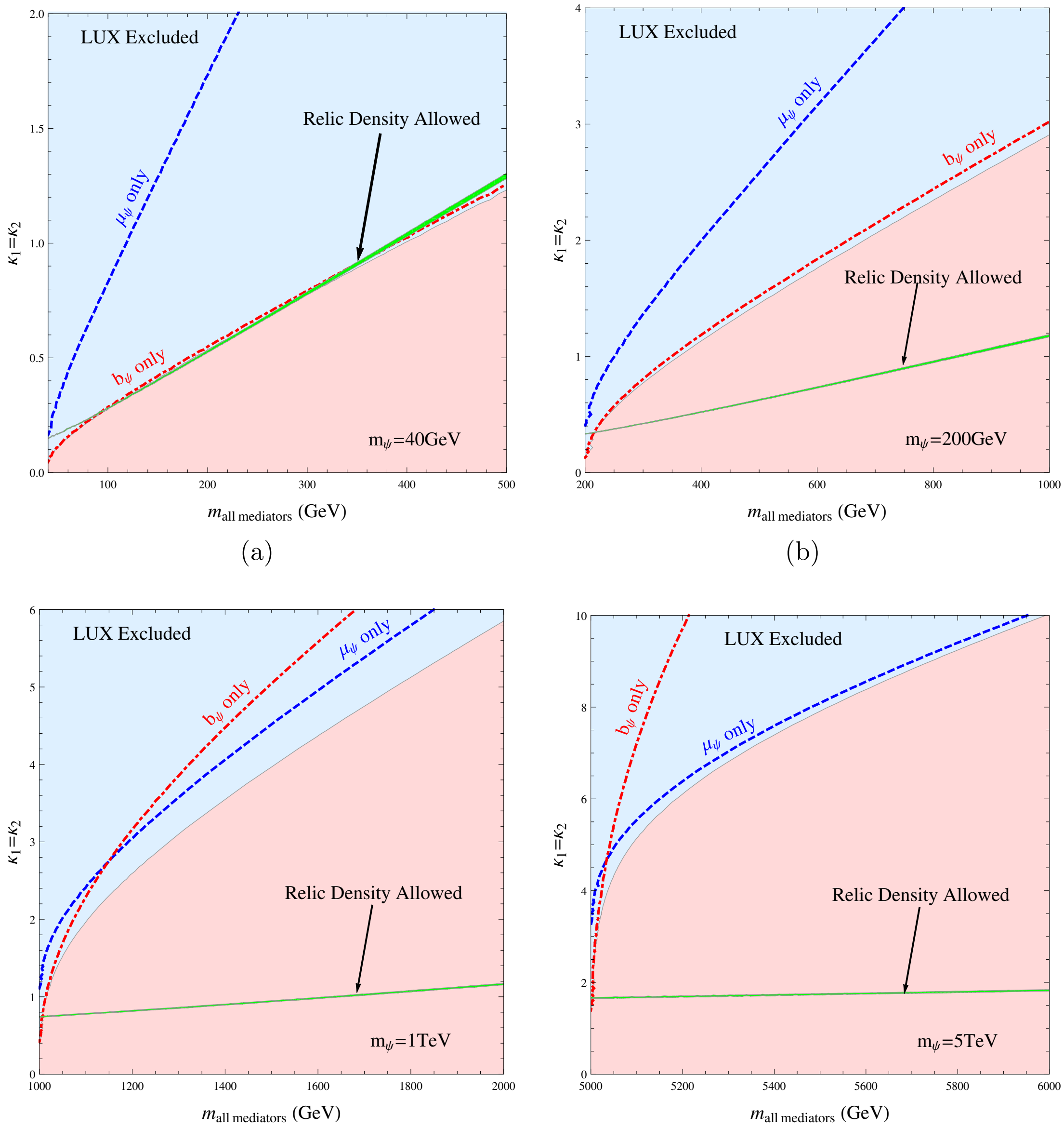

(a) (b)

(c) (d)

Figure 6.5: LUX excluded and relic density allowed regions for dark matter with different masses in the couplings versus mediator mass plane. LUX excluded regions at 95%C.L. are shown in light blue while light red regions are allowed. The "μ_ψ only" dashed line is the LUX limit retaining only the contribution of magnetic dipole moment while "b_ψ only" corresponds to including only charge radius contribution. The green contours are relic density allowed regions within two standard deviations of the Planck central value. In all plots we assume $\kappa_1 = \kappa_2$, equal mediator masses and $\lambda_2 = \lambda_5 = 0$.

The momentum dependence induced by the magnetic moment term makes it impossible to factorize the differential event rate into the product of the elastic cross section and momentum integration. We therefore need to calculate the differential rate numerically then translate the cross section into event rate in experiment. One more complexity arises since the operators shown above go beyond the traditional spin-independent and spin-dependent characterization of dark matter nucleus scattering and therefore more nuclear responses are involved [136]. The corresponding classification of the underlying non-relativistic operators responsible for dark matter nucleon scattering as well as the identification and calculation of nuclear responses for finite-sized nucleus have been performed systematically in an effective field theory framework in Ref. [120, 24] following earlier work in Ref. [115]. This framework has been implemented in the public code [89] together with statistical analysis for each experiment. We therefore use this code in our analysis and refer the reader to the above literatures for more details.

We add constraints of the dark matter direct detection to the relic density plot in Fig. 3 (a), and the new plot is shown in Fig. 6.4. For each relic density contour, we plot its corresponding limit from the LUX at the 95% C. L., which is shown as a dashed line with the same color as the relic density contour. We can see that the LUX allowed maximum magnitude of $\kappa_{1,2}$ is $1 \sim 2$ while the corresponding relic density allowed magnitudes are smaller and thus are allowed by the LUX. Notice that all direct detection limit lines intersect at four points when $|\kappa_1| = |\kappa_2|$ just like the case of the relic density contours. This is because μ_ψ and b_ψ are both independent on the mixing angle θ in this scenario and the contribution arising from the anapole moment is velocity suppressed and thus negligible.

We also show representative plots in Fig. 6.5 on the correlations between the coupling strength $\kappa_1 = \kappa_2$ and the totally degenerate mediator masses, where subfigures (a), (b), (c) and (d) correspond to taking the dark matter mass as 40 GeV, 200 GeV, 1 TeV and 5 TeV, respectively. The other parameters are fixed to be $\lambda_2 = \lambda_5 = 0$, and $\Lambda = 0$ as a result of the assumed degenerate charged scalars. So the effective dark matter-Higgs coupling is exactly zero in this scenario. Generally the Higgs mediated contribution is suppressed by the Higgs mass squared and thus subdominant compared with contributions of electromagnetic form factors [145]. In each plot, light blue(red) regions are excluded (allowed) by the LUX at the 95% C. L.; the green contours represent regions where the dark matter relic density is consistent with the measured value within 2σ level; the red dot-dashed (blue dashed) line is the LUX limit when considering only the contribution of charge radius (magnetic moment). One can see from these figures the roles played by the magnetic moment and the charge radius in the dark matter direct detections. For a relatively light dark matter, the charge radius dominates the contribution to the direct detection; while for the superheavy dark matter, the magnetic moment plays more important role. This is because the charge radius operator is dimension six while the magnetic moment operator is dimension five. It also shows that the dark matter should be around 50GeV or heavier to release the tension between the measured dark matter relic density and constraints from the LUX.

6.2.3 Higgs Couplings

Precision measurement of the Higgs couplings is one of the most important tasks in the future Higgs factory. The Yukawa coupling between the SM Higgs and tau lepton pairs was measured by the ATLAS and CMS collaborations, whose results are not so consistent with the SM prediction: $\mu_{\tau\tau} = 1.4 \pm 0.4$ by the ATLAS collaboration [7] and 0.78 ± 0.27 by the CMS collaboration [80]. In our model, the tau lepton mass arises from the Yukawa interaction induced term, i.e., $m_Y^\tau = y_\tau v/\sqrt{2}$, as well as loop corrections, m_τ^{loop}, mediated by the dark matter and two charged scalars. The mass can be written as

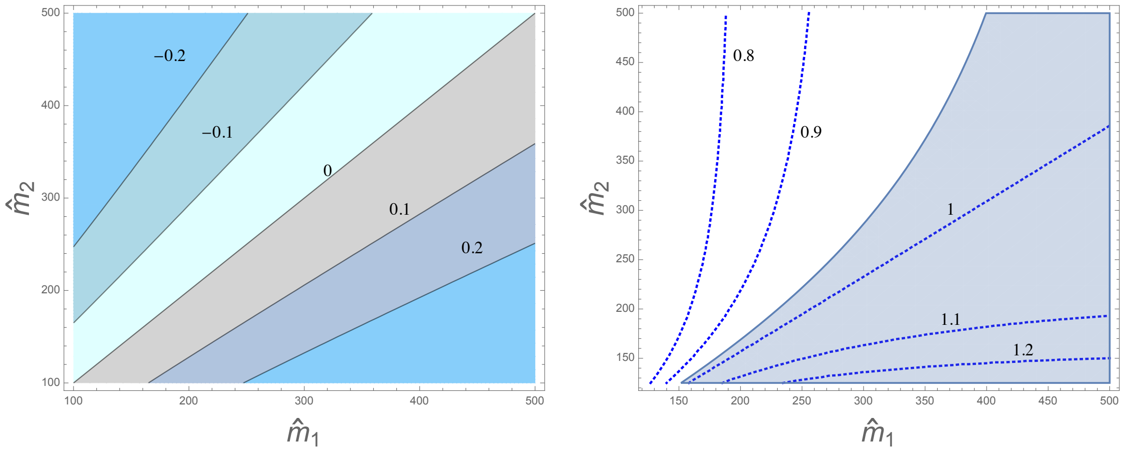

Figure 6.6: Left panel: Contours of $m_\tau^{\text{loop}}/m_\tau$ in the $\hat{m}_1 - \hat{m}_2$ plane; Right panel: Contours of $\mu_{\gamma\gamma}$ in the $\hat{m}_1 - \hat{m}_2$ plane, the cyan color marked region satisfy the combined constraint given by the ATLAS and CMS.

$$m_\tau \approx y_\tau v/\sqrt{2} + \frac{c_\theta s_\theta \kappa_1 \kappa_2 m_\psi}{16\pi^2}\left[\frac{\hat{m}_1^2}{\hat{m}_1^2 - m_\psi^2}\ln\left(\frac{\hat{m}_1^2}{m_\psi^2}\right) - \frac{\hat{m}_2^2}{\hat{m}_2^2 - m_\psi^2}\ln\left(\frac{\hat{m}_2^2}{m_\psi^2}\right)\right], \tag{6.14}$$

where we have neglected terms proportional to m_Y^τ in the calculation of m_τ^{loop}. We show in the left panel of Fig. 6.6 contours of $m_\tau^{\text{loop}}/m_\tau$ in the $\hat{m}_1 - \hat{m}_2$ plane by setting $\kappa_1 = \kappa_2 = 1$, $c_\theta = 0.6$ and $m_\psi = 100$ GeV which are consistent with dark matter constraints. It is clear that m_τ^{loop} can be $\mathcal{O}(10\%)$ of the total tau mass.

The branching ratio for the Higgs decaying into tau tau can be approximately written as

$$\text{BR}(h \to \tau\tau) \approx \frac{m_h}{16\pi\Gamma_{\text{tot}}}\left|y_\tau + \sqrt{2}\xi_\tau\right|^2 \tag{6.15}$$

where m_h is the SM Higgs mass, $\Gamma_{\text{tot}} = 4.1 \times 10^{-3}$ GeV is the SM Higgs decay width and the loop induced coupling can be written as

$$\xi_\tau = \sum_{ij=1}^{2} \frac{y_{ij} m_\psi}{16\pi^2} \int_0^1 dx \int_0^{1-x} dz \frac{1}{x m_\psi^2 + z\hat{m}_i^2 + (1-x-z)\hat{m}_j^2 - z(1-x-z)m_h^2}, \tag{6.16}$$

with $y_{11} = \kappa_1\kappa_2 c_\theta s_\theta[(\lambda_2 c_\theta^2 + \lambda_5 s_\theta^2)v + \Lambda s_{2\theta}]$, $y_{22} = -\kappa_1\kappa_2 c_\theta s_\theta[(\lambda_2 s_\theta^2 + \lambda_5 c_\theta^2)v - \Lambda s_{2\theta}]$ and $y_{12} = y_{21} = 1/2\kappa_1\kappa_2 c_{2\theta}[s_\theta c_\theta v(\lambda_5 - \lambda_2) + \Lambda c_{2\theta}]$. We plot in Fig. 6.7 the signal rate $\mu_{\tau\tau}$ associated with Higgs measurements, relative to the SM Higgs expectation, as a function of the dark matter mass by setting $c_\theta = 0.5$, $\lambda_2 = \lambda_5 = 0.1$, $\hat{m}_1 = 400$ GeV and $\hat{m}_2 = 600$ GeV as well as $\kappa_1 = -\kappa_2 = 1$ for the red solid curve and $\kappa_1 = \kappa_2 = 1$ for the blue dashed curve. The dashed and dotted horizontal lines represent central values given by the ATLAS and the CMS respectively with light blue and light yellow bands corresponding to uncertainties at the 1σ level. It should be mentioned that $\mu_{\tau\tau}$ can be significantly changed for some extreme scenarios and the modification can also be tiny for other cases (small $\kappa_{1,2}$, light dark matter and heavy degenerate charged scalars).

Due to the existence of charged scalars, the Higgs to diphoton decay width is slightly modified. The decay rate can be written in terms of couplings of the SM Higgs with new charged scalars:

$$\Gamma(h \to \gamma\gamma) = \frac{G_F \alpha^2 m_h^3}{128\sqrt{2}\pi^3} \left| -6.48 + \sum_{i=1}^{2} \frac{v c_{ii}}{2\zeta_i \hat{m}_i^2} A_0\left(\frac{4\hat{m}_i^2}{m_h^2}\right) \right|^2, \tag{6.17}$$

where -6.48 is the contribution of the W and top loops and the second term is the contribution of two new charged scalars with the definition of the loop integral function $A_0(x)$ following conventions of Ref [69]

$$A_0(x) = -x^2\left[\frac{1}{x} - f(x^{-1})\right] \quad \text{with} \quad f(x) \equiv \begin{cases} \arcsin^2(\sqrt{x}), & \text{for} \quad x > 1, \\ -\frac{1}{4}\left(\ln\frac{1+\sqrt{1-x^{-1}}}{1-\sqrt{1-x^{-1}}} - i\pi\right)^2, & \text{for} \quad x < 1. \end{cases} \tag{6.18}$$

We plot in the right panel of Fig. 6.6 contours of $\mu_{\gamma\gamma}$ in the $\hat{m}_1 - \hat{m}_2$ plane by setting $\lambda_2 = \lambda_5 = 0.5$ and $c_\theta = 0.8$. The green dashed lines from the left to the right correspond to $\mu_{\gamma\gamma} = 0.8,\ 0.9,\ 1.0,\ 1.1,\ 1.2$ respectively. The cyan color marked region satisfies the current combined bound given by the ATLAS and CMS collaborations,

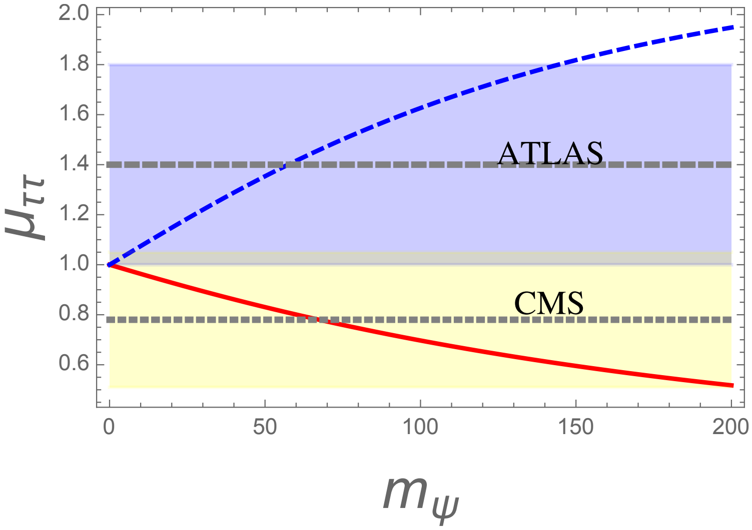

Figure 6.7: Signal rate of Higgs to tau tau relative to the SM expectation as a function of the dark matter mass.

$\mu_{\gamma\gamma} = 1.15 \pm 0.18$, where $\mu_{\gamma\gamma} = 1.17 \pm 0.27$ by the ATLAS [5] and $\mu_{\gamma\gamma} = 1.14^{+0.26}_{-0.23}$ by the CMS [161]. It should be mentioned that the future improved measurements of $\mu_{\gamma\gamma}$ may put more severe constraint on couplings of the Higgs to new charged scalars.

Finally, lets comment on the collider searches of this model. The collider signals of lepton portal dark matter models are events with charged lepton pairs and missing energy. It was showed in Ref. [17] that these models have clear signals above the SM background in certain parameter space at the LHC. Searches for signatures of our model at the LHC and lepton colliders such as CEPC or ILC, which are interesting but beyond the reach of this paper, will be shown in a future study.

6.3 Concluding remarks

Lepton-flavored dark matter is interesting and appealing for many aspects. In this paper we focused on the phenomenology of the tau-flavored Dirac dark matter model. The electromagnetic form factors of the dark matter which are crucial for the dark matter direct detections, were calculated in the case where there are two types of dark matter - third generation lepton Yukawa interactions. Our study shows that the tension between the observed dark matter relic density and constraints of dark matter direct detections are highly loosed. Besides, the charge radius dominates the contributions to the dark matter direct detection for the light dark matter case, while the magnetic moment plays more important role for heavy dark matter case. In addition the Yukawa coupling of $h\bar{\tau}\tau$ can be significantly changed in this model, since the one-loop induced tau mass can be $\mathcal{O}(10\%)$ of the total mass. As a result, the signal rate of $h\bar{\tau}\tau$, relative to the SM expectation, measured by the LHC, can be explained in this model. The Higgs to diphoton ratio is also slightly changed but is still consistent with the current LHC constraint.

CHAPTER 7

HIGGS PORTAL FERMIONIC DARK MATTER IN 2HDM

Including a dark matter can be done in a minimal way by considering an extended Higgs sector with dark matter - Higgs portal interactions. In this case the dark matter will annihilate into SM particles through these Higgs portal interactions. The simplest extention of the SM Higgs sector is to add a singlet dark matter scalar through operator $\alpha_S \Phi^\dagger \Phi S^2$ [117, 38] or a fermionic dark matter through $\frac{\alpha_F}{\Lambda} \Phi^\dagger \Phi \bar{\chi} \chi$ [116] where Φ is the SM Higgs doublet, S, χ are the scalar and fermionic dark matter respectively and Λ is a mass scale for the effective interaction. The constraints in the $(\alpha_{S/F}, m_{S,F})$ plane from relic dentiy and direct detection requirements are shown in Fig. 7.1 where the allowed regions from relic density are shown between the narrow red lines while the regions above the dashed lines are excluded by the according direct detection limits. Among the various direct detection limits, the LUX result [20] is the most stringent one and excluded most of the parameter space of the fermionic dark matter case except on the SM Higgs resonance when dark matter has mass ≈ 62.5GeV. For the scalar dark matter, aside from the resonance region, a heavier dark matter with mass $\gtrsim 100$GeV is still viable. In both cases, the resonant enhancement of the S channel dark matter annihilation cross section need a much smaller $\alpha_{S,F}$ and thus lead to a direct detection cross section compatible with the null search limits. For the fermionic extention, the exlucsion limit on the parameter space can be ameliorated by adding parity-violating interactions [177] since the these terms contribute much less to the direct detection cross section. To avoid including these parity-violating interactions, one can also consider models with an extended Higgs sector such as the

hhh :	$c_1 = -3m_h^2$
hA_0A_0 :	$c_2 = 2\tilde{\nu}v^2 - m_h^2 - 2m_A^2$
HA_0A_0 :	$c_3 = 2(m_H^2 - \tilde{\nu}v^2)/t_{2\beta}$
hHH :	$c_4 = 2\tilde{\nu}v^2 - 2m_H^2 - m_h^2$
HHH :	$c_5 = 6(m_H^2 - \tilde{\nu}v^2)/t_{2\beta}$
hH^+H^- :	$c_6 = 2\tilde{\nu}v^2 - m_h^2 - 2m_{H^\pm}^2$
HH^+H^- :	$c_7 = 2(m_H^2 - \tilde{\nu}v^2)/t_{2\beta}$

Table 7.1: Triple-Higgs Couplings in the alignment limit $\beta - \alpha = \pi/2$. Feynman rules are obtained by adding the factor i/v.

2HDM with two Higgs doublets and consider adding Higgs portal interactions of the type $\frac{\alpha_{ij}}{\Lambda}\bar{\chi}\chi\Phi_i^\dagger\Phi_j$ where i, j denote the two Higgs doublet indices. In this case, there will be additional annihilation channels with purely scalar final states and this kind of interactions do not contribute to direct detection cross section and might reduce the stringent limit as compared with the simple SM extension. Another way of looking at this clearly is to go to the Higgs basis with one Higgs doublet H_2 taking no vev. If only the interaction $\bar{\chi}\chi H_2^\dagger H_2$ is added, then it will contribute to dark matter annihilations but not to direct detection cross section at tree level while a loop level dark matter quark interactions are generally suppressed and can potentially lead to a viable dark matter model.

In the following, we will study this model in detail. In Sec. **??**, we will discuss the model to fix the conventions. In the following section 7.1, the Higgs potal interactions are introduced with the relic density and direct detection cross sections calculated where we discuss in detail the mechanism why this model is more viable compared with the SM case. In Sec. 7.2, we discuss the scenario with no tree level direct detection signals and study the one-loop induced direct detection signals. In the end, we make a summary.

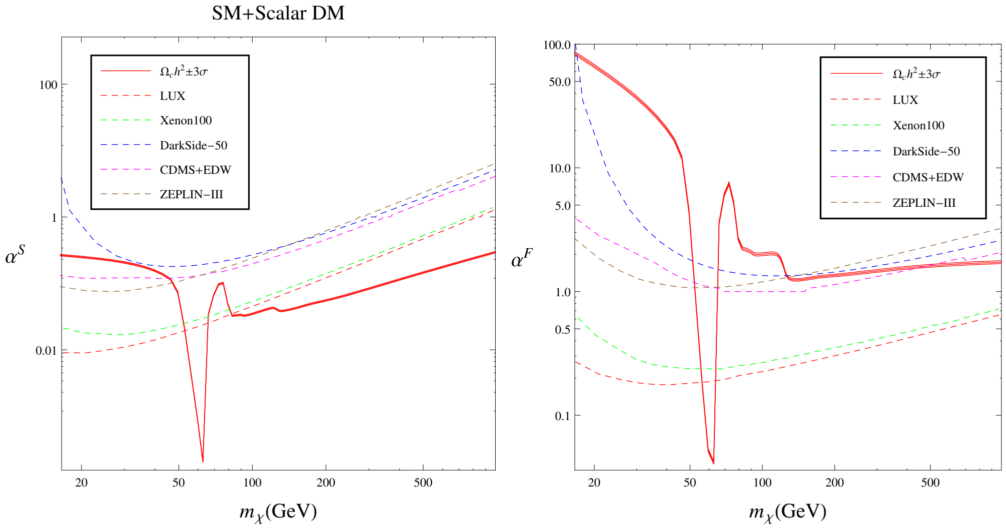

Figure 7.1: Parameter space of Higgs portal scalar(left) and fermionic(right, Λ = 1TeV) dark matter model in simple SM extention. Solid red lines(region) give observed dark matter relic density within three standard deviations. Dashed lines coorespond to direct detection upper limits and regioins above these lines are exluded. All points in above lines are obtained numerically from MicrOMEGAs. From now on we keep only limits from Xenon100 and LUX in our analysis.

7.1 DM Phenomenology (1): general analysis

Our goal is to study a model with two Higgs doublets and a fermionic DM χ, which is a gauge singlet and mainly couples to the Higgs bilinears. We work with the 2HDM with a Z_2 symmetry under which Φ_1 is odd and Φ_2 is even. We also include a soft-breaking term in the Higgs potential with m_{12}^2 non-zero to avoid the cosmological domain wall problem [219]. Thus the relevant interactions can be obtained directly from chpater 3 by setting $\lambda_6 = \lambda_7 = 0$. We will study its phenomenology in this section, assuming general scalar-type effective interactions of dark matter operator $\bar{\chi}\chi$ with the Higgs bilinears $\Phi_i^\dagger \Phi_j$, while implications of PV effective interactions are beyond the reach of this paper.

7.1.1 DM Interactions

Assuming the DM is a Dirac fermion χ and only couple to the Higgs doublets, the effective Lagrangian can be written as

Higgs Doublet Bilinear Decomposition in Physical Fields							
	h	H	h^2	H^2	A_0^2	hH	H^+H^-
$(t_\beta^2+1)\Phi_1^\dagger\Phi_1$	v	$t_\beta v$	$\frac{1}{2}$	$\frac{1}{2}t_\beta^2$	$\frac{1}{2}t_\beta^2$	t_β	t_β^2
$(t_\beta^2+1)(\Phi_1^\dagger\Phi_2+\Phi_2^\dagger\Phi_1)$	$2t_\beta v$	$(t_\beta^2-1)v$	t_β	$-t_\beta$	$-t_\beta$	t_β^2-1	$-2t_\beta$
$(t_\beta^2+1)\Phi_2^\dagger\Phi_2$	$t_\beta^2 v$	$-t_\beta v$	$\frac{1}{2}t_\beta^2$	$\frac{1}{2}$	$\frac{1}{2}$	$-t_\beta$	1

Table 7.2: Decomposition of the Higgs doublet bilinear $\Phi_i^\dagger\Phi_j$ in terms of physical fields in the SM limit $\alpha = \beta - \frac{\pi}{2}$. The only mixing angle left is β, such that above expansion coefficients are functions of t_β only. In the expansion of these bilinear, there is a common factor $\frac{1}{t_\beta^2+1}$ and that is the reason for multiplying the pre-factor (t_β^2+1) with the bilinear $\Phi_i^\dagger\Phi_j$ in the first column.

$$\mathcal{L} = \bar{\chi}(i\not{\partial} - M_0)\chi + \sum_i^2 \frac{\alpha_{ii}}{\Lambda}\bar{\chi}\chi(\Phi_i^\dagger\Phi_i) + \left\{\frac{\alpha_{12}}{\Lambda}\bar{\chi}\chi(\Phi_1^\dagger\Phi_2) + \frac{\alpha_{21}}{\Lambda}\bar{\chi}\chi(\Phi_2^\dagger\Phi_1)\right\} \ , \qquad (7.1)$$

where Λ is the cut-off scale and α_{ij} are the couplings with $\alpha_{12} = \alpha_{21}$. If the Z_2 symmetry, imposed on Φ_i is a good symmetry, terms like $\Phi_1^\dagger\Phi_2$ bilinear should not show up. Since the Z_2 symmetry is explicitly broken and adding them will not affect the physical scalar spectrum, these terms are included in the Lagrangian. We show in Table. 7.2 the decomposition of the Higgs doublet bilinear $\Phi_i^\dagger\Phi_j$ in terms of physical fields in the alignment limit. To summarize, we have the following set of free parameters, m_χ, Λ, α_{ij}, m_H, m_{A^0}, $m_{H^\pm}$, $\tilde{\nu}$, t_β, α.

7.1.2 Relic density

The DM in the early Universe was in the local thermodynamic equilibrium. When its interaction rate drops below the expansion rate of the Universe, the DM is said to be decoupled. The evolution of the DM number density n, is governed by the Boltzmann equation:

$$\dot{n} + 3Hn = -\langle\sigma v_{\mathrm{M\o ller}}\rangle(n^2 - n_{\mathrm{EQ}}^2) \ , \qquad (7.2)$$

where H is the Hubble constant, $\sigma v_{\text{M}\not{o}\text{ller}}$ is the total annihilation cross section multiplied by the M$\not{o}$ller velocity, $v_{\text{M}\not{o}\text{ller}} = (|v_1 - v_2|^2 - |v_1 \times v_2|^2)^{1/2}$, brackets denote thermal average and n_{EQ} is the DM number density at thermal equilibrium. It has been shown that $\langle \sigma v_{\text{M}\not{o}\text{ller}} \rangle = \langle \sigma v_{\text{lab}} \rangle = 1/2[1 + K_1^2(x)/K_2^2(x)]\langle \sigma v_{\text{cm}} \rangle$, where $x = m/T$ and K_i are the modified Bessel functions of the order ith.

The freeze-out of the cold DM occurred when it was non-relativistic. We can approximate $\langle \sigma v \rangle$ with the non-relativistic expansion $\langle \sigma v \rangle = a + b\langle v^2 \rangle + \mathcal{O}(\langle v^4 \rangle) \approx a + 6b/x$, where $v \equiv v_{\text{lab}}$. Thus one can calculate the thermal average analytically by expanding $s = 4M^2 + M^2 v^2 + 3/4 M^2 v^4$, in the laboratory frame. More accurately, $\langle \sigma v \rangle$ can be calculated numerically using the integral

$$\langle \sigma v_{\text{M}\not{o}\text{ller}} \rangle = \frac{1}{8m^4 T K_2^2(m/T)} \int_{4m^2}^{\infty} \sigma(s - 4m^2)\sqrt{s} K_1(\sqrt{s}/T) ds \ , \tag{7.3}$$

where m is the DM mass, $K_i(x)$ are the Bessel functions and T is the temperature.

The relic density of χ is

$$\Omega_\chi = \frac{m_\chi n_\chi}{\rho_c} = \frac{m_\chi s Y}{\rho_c}, \tag{7.4}$$

evaluated at present time or temperature $T_0 = 2.726K$, where $\rho_c = \frac{3H^2}{8\pi G}$ is the critical density with the Hubble constant being $H = 100h$ kms^{-1}Mpc^{-1}, $s = h_{eff}(T)\frac{2\pi^2}{45}T^3$ is the entropy density wherein $h_{eff}(T)$ is the effective number of degrees of freedom [210] and Y is the abundance to be calculated at T_0. A good approximation can be made to the solution of Y_0 following Ref[132, 42]

$$\frac{1}{Y_0} = \frac{1}{Y_f} + \sqrt{\frac{\pi}{45G}} \int_{T_0}^{T_f} g_*^{1/2}(T)\langle \sigma v \rangle dT, \tag{7.5}$$

where T_f is the freeze-out temperature defined such that $Y_f = Y_{T_f} = (1 + \delta)Y_{eq}(T_f)$ with δ being some small constant.

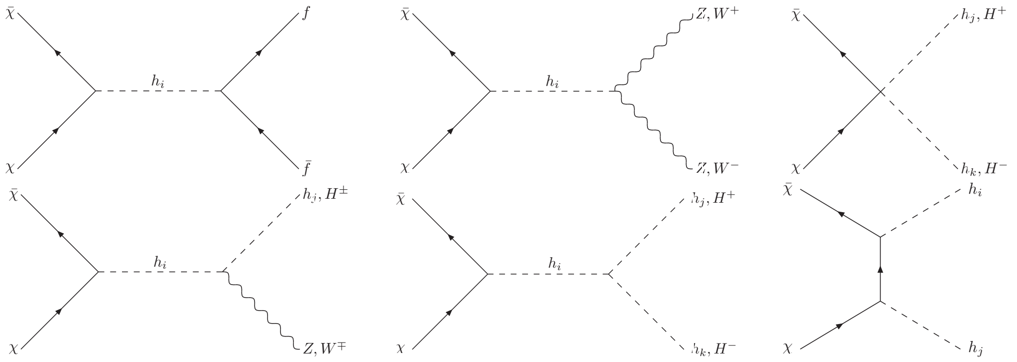

Figure 7.2: Representative feynman diagrams contributing to DM two body annihilations.

To derive the analytical expression of the DM relic density, one needs to calculate the thermal average of annihilation cross sections of $\bar{\chi}\chi$ into the matter fields in the 2HDM. It is straightforward to calculate the tree level cross section for the 2-body final states. The relevant Feynman diagrams for the annihilation of the DM are given in Fig. 7.2. The annihilation cross section of $\bar{\chi}\chi \to ab$ can be written as

$$\sigma(\bar{\chi}\chi \to ab) = \zeta_{ab}^{-1} \mathcal{F}(s, m_a^2, m_b^2) \overline{|\mathcal{M}|}^2 \,, \tag{7.6}$$

where s is the Mandelstam variable, m_i are masses of particles in the final states, $\zeta_{ab} = 2$ if final state particle are identical and $\zeta_{ab} = 1$ for any other cases, $F(s, m_a^2, m_b^2) \equiv 1/(16\pi s)\lambda^{1/2}(s, m_a^2, m_b^2) \times \lambda^{-1/2}(s, m_\chi^2, m_\chi^2)$ where $\lambda(x, y, z) \equiv x^2 + y^2 + z^2 - 2xy - 2xz - 2yz$, $\overline{|\mathcal{M}|}^2$ is the squared amplitude summed over the spin of the final states and averaged over the spin of the initial states. We list in the following the squared amplitude for various annihilation processes:

- $\bar{\chi}\chi \to \bar{f}f$:

$$\sum_{a,b=1}^{3} \kappa_a \kappa_b \frac{m_f^2}{v^2} \frac{s - 4m_\chi^2}{(s - m_a^2)(s - m_b^2)} \left[(\tilde{R}_{a1} + k_f \tilde{R}_{a2})(\tilde{R}_{b1} + k_f \tilde{R}_{b2})(s - 4m_f^2) + \tilde{R}_{a3}\tilde{R}_{b3} s \right] \tag{7.7}$$

where $\kappa_a = \sum_{ij} v_i \alpha_{ij} R_{aj}/\Lambda$. .

- $\bar{\chi}\chi \to WW/ZZ$:

$$\sum_{a,b=1}^{3} \kappa_a \kappa_b t_a t_b \left(3 + \frac{s^2}{4M_V^2} - \frac{s}{M_V^2}\right) \frac{s - 4m_\chi^2}{2(s - m_a^2)(s - m_b^2)} \tag{7.8}$$

where $t_a \equiv \sum_i g^2 v_i R_{ai}/2$ for WW final states and $t_a \equiv \sum_i g^2 v_i R_{ai}/2c_w^2$ for ZZ final states, wherein $c_W = \cos\theta_W$ with θ_W the weak mixing angle.

- $\bar{\chi}\chi \to h_a h_b$:

$$\frac{1}{2}(s - 4m_\chi^2) \left| \kappa_{ab} + \sum_c \kappa_c \tilde{\Gamma}_{cab} \frac{1}{s^2 - m_c^2} \right|^2 \tag{7.9}$$

where $\kappa_{ab} = \sum_{i,j=1}^{2} \frac{\alpha_{ij}}{\Lambda} R_{ai} R_{bj}$ for neutral Higgs final states, $\kappa_{ab} = \sum_{i,j=1}^{2} \frac{\alpha_{ij}}{\Lambda} U_{i2} U_{j2}$ for charged Higgs, U(as well as the following V) is a matrix defined analogously as in Ref. [137] and $\tilde{\Gamma}_{cab}$ is the coupling for trilinear Higgs interaction, which can be found in Table. 7.1. We have neglected t-channel contribution for simplicity.

- $\bar{\chi}\chi \to h_c Z$:

$$\frac{g^2}{8c_W^2} \sum_{a,b} \kappa_a \kappa_b \mathrm{Im}(V^+V)_{ac} \mathrm{Im}(V^+V)_{bc} \frac{(s - 4m_\chi^2)[(s - M_Z^2)^2 - 2m_c^2(s + M_Z^2) + m_c^4]}{M_Z^2 (s - m_a^2)(s - m_b^2)}. \tag{7.10}$$

- $\bar{\chi}\chi \to H^+W^-$:

$$\frac{g^2}{8} \sum_{a,b}^{4} \kappa_a \kappa_b (V^+U)_{ac} (V^+U)_{bc} \frac{(s - 4m_\chi^2)[(s - M_W^2)^2 - 2m_c^2(s + M_W^2) + m_c^4]}{(s - m_a^2)(s - m_b^2) M_W^2} \tag{7.11}$$

and U^+V should be used for H^-W^+ final states.

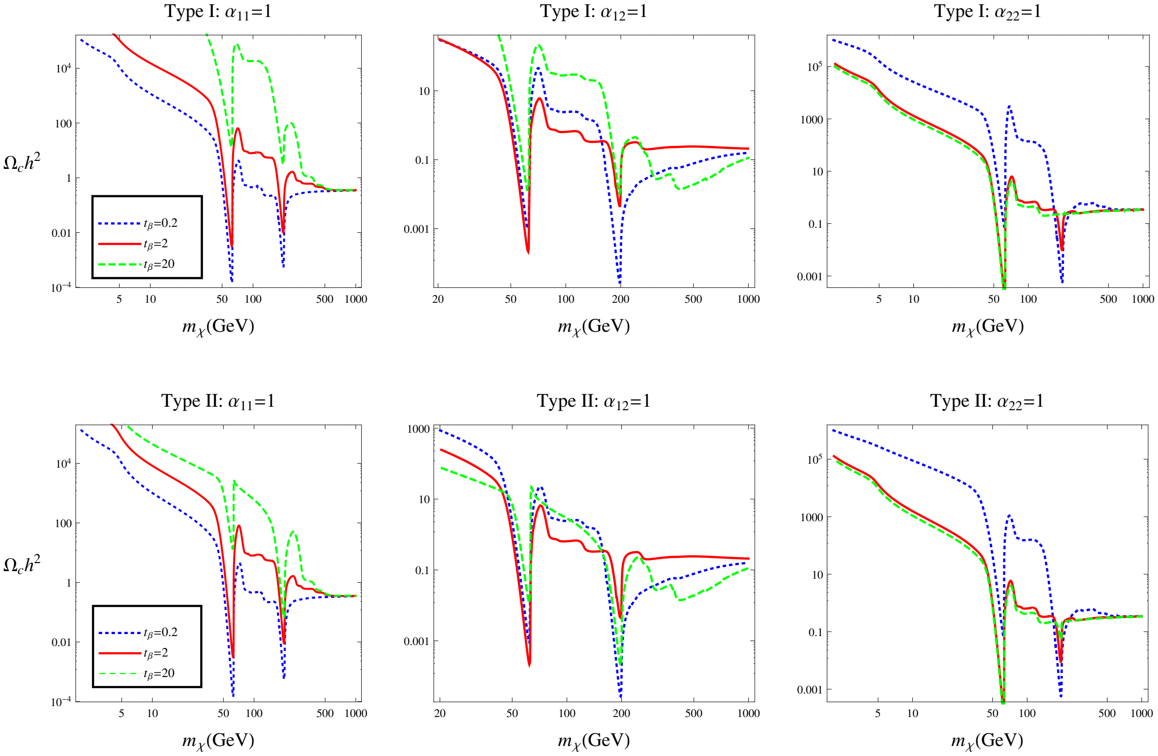

Figure 7.3: Relic density dependence on m_χ, t_β, α_{ij} for fermionic DM. First row is for type I and second row for type II. In each model, only one of α_{ij} is turned on and in each figure three different values of t_β are used for comparison. All other parameters are kept fixed, $m_H = 400$, $m_A = 300$, $m_{H^\pm} = 500$.

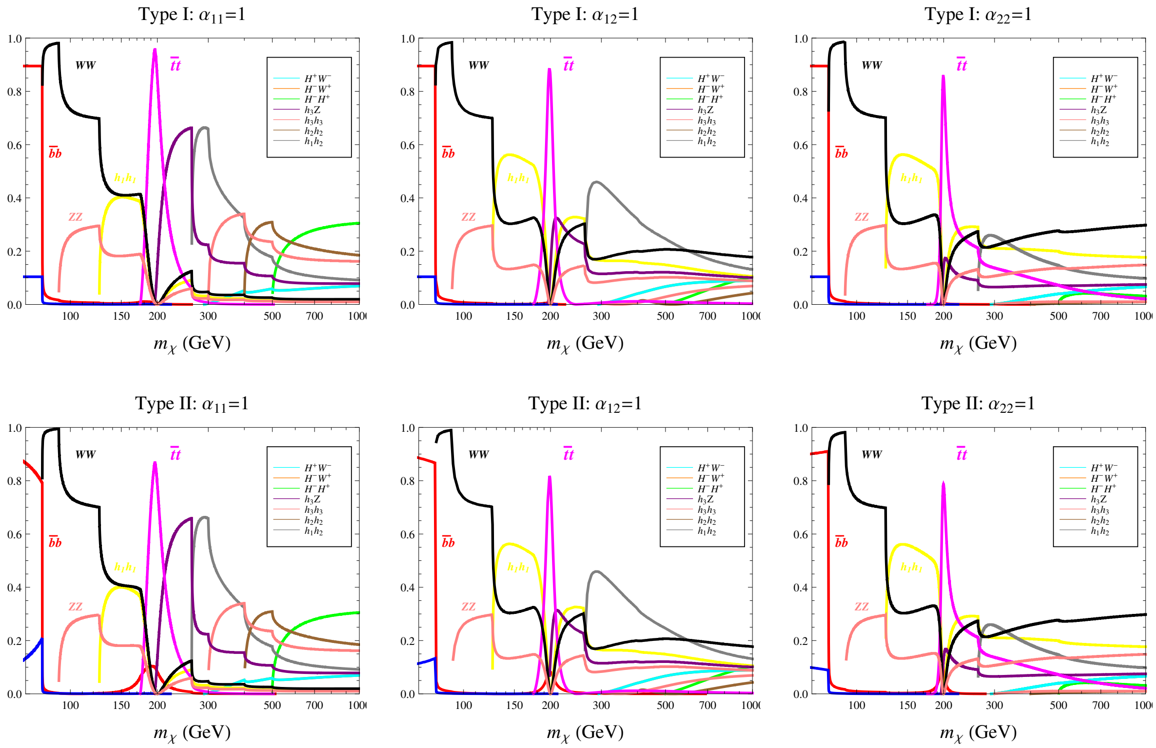

Type I: α_{11}=1

Type I: α_{12}=1

Type I: α_{22}=1

Type II: α_{11}=1

Type II: α_{12}=1

Type II: α_{22}=1

Figure 7.4: The fractions of various channels contributing to DM annihilations for type I and II 2HDM in the alignment limit. The parameters are fixed to be $t_\beta = 2$, $m_H = 400\text{GeV}$, $m_{A_0} = 300\text{GeV}$, $m_{H^\pm} = 500\text{GeV}$ and $m_{12}^2 = 0$.

Although the DM relic density can be calculated analytically, we carry out numerical simulation with the help of MicrOMEGAs [43, 44, 45], which solves the Boltzmann equation numerically and utilizes CalcHEP [48] to calculate the relevant cross sections. We implement the type-I and -II 2HDM models in LanHEP [206, 205] and use the generated model files in MicrOMEGAs to do numerical analysis. In both scenarios, we fix $\Lambda = 1000$ GeV to reduce one parameter .

Working in the alignment limit, we show in Fig. 7.3 the relic abundance as a function of DM mass for the type-I (first row) and -II (second row) 2HDM. For each model, we show three different plots where only one of the couplings α_{ij} is turned on and fixed to be 1, and for each plot three different choices of t_β are used corresponding to $t_\beta = 0.2$ (dotted line),2 (solid line), 20 (dashed line) respectively. The remaining parameters are fixed to be $m_H = 400$ GeV, $m_{A_0} = 300$ GeV and $m_{H^\pm} = 500$ GeV. We can see in each scenario, there are two obvious dips at $m_\chi \approx 62.5, 200$ GeV which are caused by the two resonantly enhanced annihilations mediated by the s-channel h, H. There is no resonance enhancement arising from A_0, which is due to the absence of CP violation in our scalar potential. In all cases, the relic density declines as m_χ increases since new channels will be opened up and more phase space is now available. In the aligment limit we are considering, there is no HWW, HZZ couplings and the differences between the type-I and -II 2HDMs largely come from how the heavy CP-even H couples to fermions. The trilinear interactions, which arise from the Higgs potential, are the same for type-I and -II 2HDM as given in Table. 7.1 and are generally much larger than Yukawa couplings. So that as m_χ becomes heavier than scalar masses, the DM will dominantly annihilate into diHiggs. The dependence of Ωh^2 on t_β will become inconspicuous and is model type independent. This type-independence behavior is obvious when comparing the contour plots in each column of Fig. 7.3.

We show in Fig. 7.4 the fraction of various annihilation channels as a function of the DM mass using the same inputs as these in Fig. 7.3 by fixing $t_\beta = 2$. For light χ, the main channels are $\bar{b}b, \bar{c}c$, and dibosons will dominate once these channels are kinematically allowed. For heavy χ, the diHiggs annihilation will generally take over and dominate. In this case there is little difference between two types of 2HDM since these interactions have the same couplings as shown in Table. 7.1.

7.1.3 Direct Detection

Should the cold DM exists, it can be detected through their scattering on atomic nuclei on Earth, by production at particle colliders or through detecting their annihilation products in our galaxy and its satellites. The direct detection registers the interactions of through-going DM particles. The basic methodology for direct detection experiments is to search for rare events that might be the signature of WIMP, namely the recoil energy of the atomic nuclei from the elastic scattering of a DM off a target nuclei. The calculation of the DM direct detection rate in terrestrial detectors depends on several factors including the local halo density, velocity distribution in Milky Way, the DM mass and the cross section on the target nuclei. The effective DM-quark interactions, mediated by the neutral Higgs, naturally induce the DM-nucleus interaction. The effective Hamiltonian in our model can be written as

$$H \equiv \sum_q \lambda_q \bar{\chi}\chi\bar{q}m_q q = \begin{cases} \sum_q \frac{\tilde{V}_{2a}\kappa_a}{v_2 m_a^2}(\bar{\chi}\chi)\bar{q}m_q q \ , & \text{Type-I 2HDM} \\ \sum_q \frac{\tilde{V}_{ka}\kappa_a}{v_k^q m_a^2}(\bar{\chi}\chi)\bar{q}m_q q \ , & \text{Type-II 2HDM} \end{cases} \tag{7.12}$$

where v_k^q equals to $v_2(v_1)$ for up(down)-type quarks, with v_k the VEV of the Φ_k, m_q is the mass of the quark q, and m_a is the mass of the CP-odd scalars. It should be mentioned that this effective Hamiltonian is closely correlated with the type of 2HDM.

Parameterizing the nucleonic matrix element as $\langle N|\sum_q m_q\bar{q}q|N\rangle = f_N m_N$, where m_N is the proton or neutron mass, and

$$f^{p,n} = \sum_q \lambda_q f_q^{p,n} \tag{7.13}$$

where the nucleon form factors are $f_u^p = 0.020 \pm 0.004$, $f_d^p = 0.0026 \pm 0.005$, $f_s^p = 0.118 \pm 0.062$, $f_d^u = 0.014 \pm 0.003$, $f_d^n = 0.036 \pm 0.008$ and $f_s^n = 0.118 \pm 0.062$ [45], the cross section for the DM scattering elastically from a nucleus into the momentum transfer limit is given by

$$\sigma^{\mathrm{SI}} = \frac{\mu^2}{\pi}\left[Z m_p f^p + (A-Z) m_n f^n\right]^2 \ , \tag{7.14}$$

where $\mu = m_\chi M_N/(m_\chi + M_N)$ being the reduced mass of the DM-nucleon system, with M_N the target nucleus mass, Z and $(A-Z)$ are the numbers of protons and neutrons in the nucleus. If dark matter is Majorana particle, the SI cross section in Eq. (7.14) should be multiplied by the factor 4.

To find out which scenario can loose the tension between the observed DM relic abundance and constraints of direct detections, we show in Fig. 7.5, 7.6 and 7.7 the exclusion limit given by the LUX 2015 [20] as well as the contours of DM relic abundance in the $\alpha_{ij} - m_\chi$ plane with t_β taking the value of 0.2, 2 and 20 respectively. Other inputs are the same as these in making Fig. 7.3. For each case, the first row is for the type-I 2HDM, the second row is for type-II 2HDM and the three plots in each row from the left to the right correspond to $\alpha_{11} \neq 0$, $\alpha_{12} \neq 0$ and $\alpha_{22} \neq 0$ respectively. In each plot, the region above the red dashed line is excluded by the LUX 2015 result and the blue contours give the correct relic density within three standard deviations of the Planck central value. From these figures, we can see in all cases, the behavior of the relic density contours for heavier dark matter with $m_\chi \gtrsim 400$GeV are similar and the couplings α_{ij} all converge to a value around 1, which follows from the previous

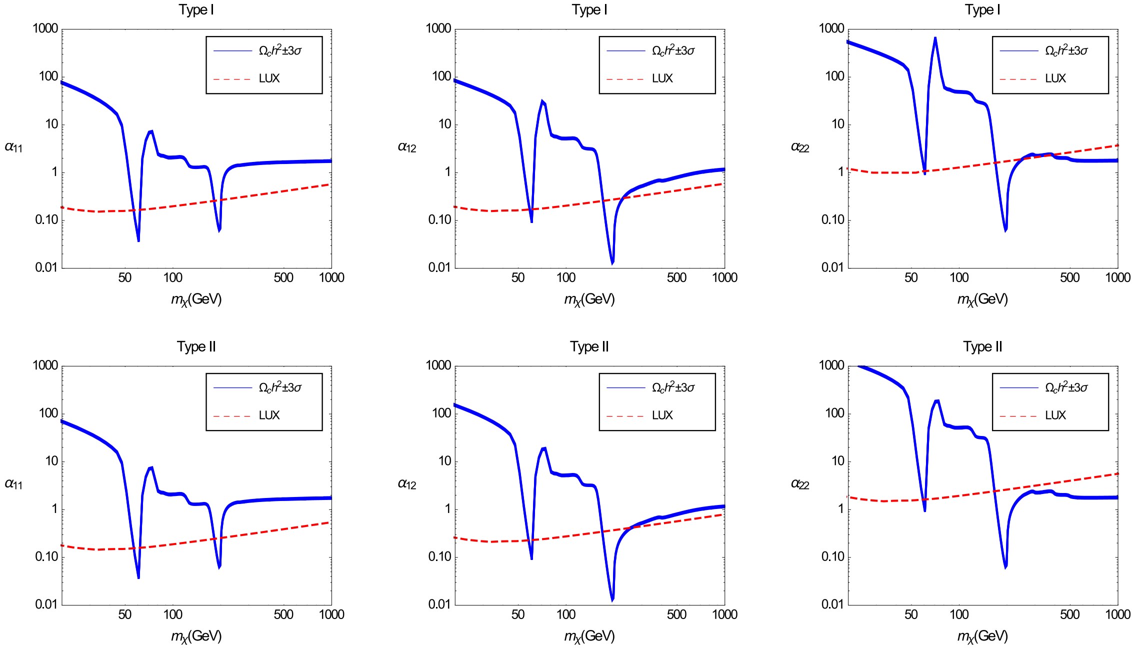

Figure 7.5: Constraints on the $\alpha_{ij} - m_\chi$ plane for type-I and type-II 2HDM in the SM limit with $t_\beta = 0.2$. The other parameters are fixed to be $m_H = 400$GeV, $m_A = 300$GeV, $m_{H^\pm} = 500$GeV and $m_{12}^2 = 0$. The green solid contours give correct relic density within three standard deviations and the regions above red dashed lines are excluded by the LUX 2015 limit.

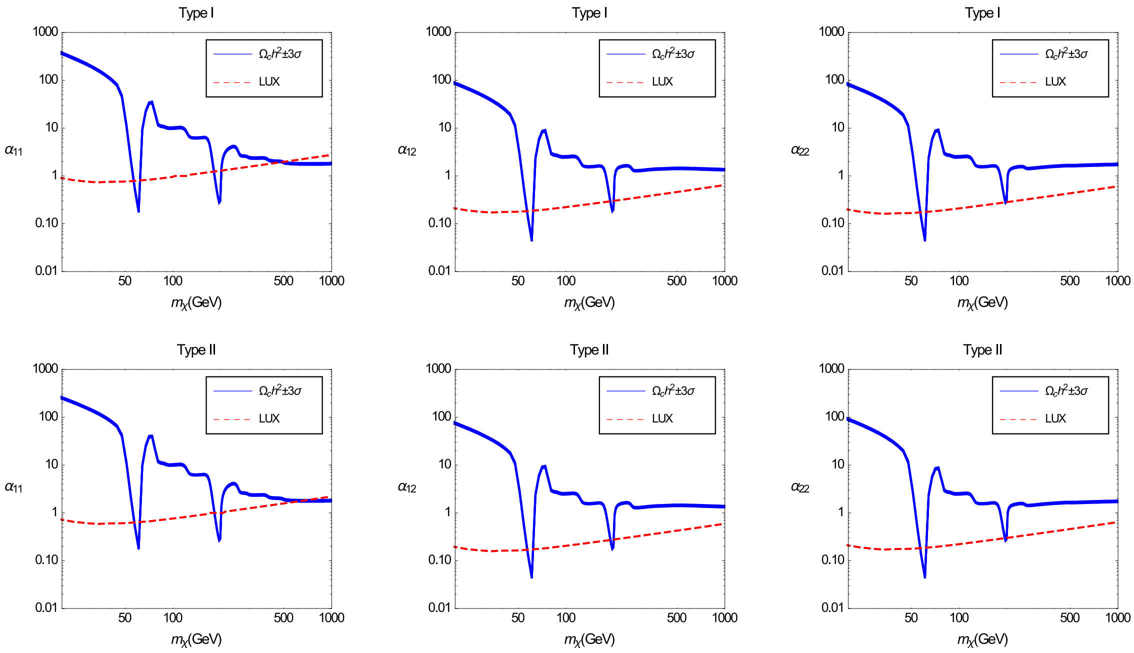

Figure 7.6: Constraints on the $\alpha_{ij} - m_\chi$ plane for type-I and type-II 2HDM in the SM limit with $t_\beta = 2$. The other parameters are fixed to be $m_H = 400$GeV, $m_A = 300$GeV, $m_{12}^2 = 0$ and $m_{H^\pm} = 500$GeV. The green solid contours give correct relic density within three standard deviations and the regions above red dashed lines are excluded by the LUX 2015 limit.

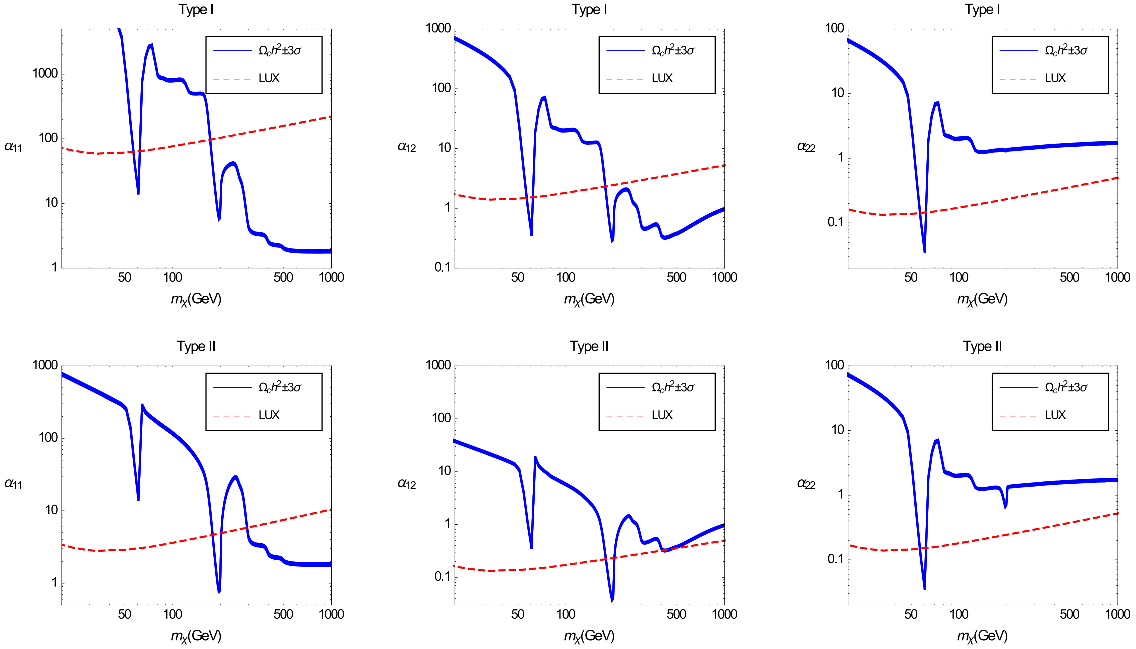

Figure 7.7: Constraints on the $\alpha_{ij} - m_\chi$ plane for type-I and type-II 2HDM in the SM limit with $t_\beta = 20$. The other parameters are fixed to be $m_H = 400$GeV, $m_A = 300$GeV, $m_{12}^2 = 0$ and $m_{H^\pm} = 500$GeV. The green solid contours give correct relic density within three standard deviations and the regions above red dashed lines are excluded by the LUX 2015 limit.

arguments on the 2HDM type and t_β independent behavior for the heavy DM. On the other hand, the LUX limit depends on the type of 2HDM, t_β as well as α_{ij}. Therefore a looser constraint from LUX for heavy DM can be found by adjusting t_β and the interaction form of DM with Higgs bilinears. On the contrary for light DM which mainly annihilates into fermionic final states, both DM annihilations and SI cross section are controlled by the same factors, such that the conflict between relic density and direct detection limits as observed in the simple SM extension remains to prevent a viable dark matter candidate except when $m_\chi \sim m_{h,H}$. This can be seen most clearly for type-I 2HDM with α_{11} turned on, which correspond to the top-left plot in Fig. 7.5, 7.6 and 7.7. The t_β dependent factor can be isolated from the d_q for the type-I 2DHM. By collecting the factors from Eq. (**??**), Eq. (**??**), Table. **??** and Table.7.2, we find

$$d_q \propto \frac{1}{t_\beta^2+1}\frac{1}{m_h^2} + \frac{t_\beta}{t_\beta^2+1}\frac{1}{m_H^2}(-\cot\beta), \qquad (\text{for } \alpha_{11} \neq 0) \tag{7.15}$$

where the first and second term are from h and H mediated diagrams respectively. This is a monotonically decreasing function as t_β increases. So as t_β increases, the direct detection cross section decrease monotonically. Keeping in mind that the annihilation cross section will only decreases as t_β increase in light DM regime, which leads to a lift of α_{11} so as to get the correct relic abundance, both the blue contours and red dashed exclusion limit are lifted higher at approximately the same steps for light DM as t_β increase. So for light mass regions, the conflict between relic density and LUX limit still exists. But for heavy mass regions, only LUX limit are lifted higher while relic density contours remains approximately the same position which then makes a dark matter viable. In the case when $t_\beta = 20$ as shown in the top-left plot of Fig. 7.7, a DM with mass $200 - 1000\ GeV$ is allowed.

Following the same logic as the above case, the behavior of the remaining plot can be understood. For the top-middle plot corresponding to type I 2HDM with α_{12}

turned on, going from $t_\beta = 0.2$ in Fig. 7.5 to $t_\beta = 2$ in Fig. 7.6 leads to no obvious change of the contours. This can be interpreted from inspecting the dependence of d_q on t_β, which is

$$d_q \propto \frac{2t_\beta}{t_\beta^2+1}\frac{1}{m_h^2} + \frac{t_\beta^2-1}{t_\beta^2+1}\frac{1}{m_H^2}(-\cot\beta), \qquad (\text{for } \alpha_{12} \neq 0)\ . \tag{7.16}$$

This function has about the same value at $t_\beta = 0.2$ and $t_\beta = 2$ since there is a local maximum at $t_\beta = 0.88$ after which d_q decreases monotonically. Then as t_β is changed from 2 in Fig. 7.6 into 20 in Fig. 7.7, both relic density at small mass regions and the LUX exclusion limit at the whole mass range are lifted higher by about an order of magnitude and a heavy dark matter with mass $200 - 1000$GeV becomes viable. Finally for type I 2HDM and when α_{22} is nonzero as shown in the top-right plot, the one with $t_\beta = 0.2$ is viable for heavy DM with mass $500 - 1000$GeV, while $t_\beta = 2$ and $t_\beta = 20$ cases have similar behavior and exclude all mass regions except near Higgs resonance. This behavior can be understood from collecting the relevant t_β dependence of d_q,

$$d_q \propto \frac{t_\beta^2}{t_\beta^2+1}\frac{1}{m_h^2} + \frac{t_\beta}{t_\beta^2+1}\frac{1}{m_H^2}(-\cot\beta), \qquad (\text{for } \alpha_{22} \neq 0) \tag{7.17}$$

which is a monotonically increasing function, and is negative when $t_\beta < 0.31$ and positive when $t_\beta > 0.31$ with the point $t_\beta = 0.31$ leading to a complete cancellation between contributions from h and H diagrams. Due to the closeness to this zero point, the $\sigma^{\rm SI}$ at $t_\beta = 0.2$ takes a much smaller value as comparing with cases at $t_\beta = 2, 20$, thus the DM with mass $200 - 1000$GeV is available in this case.

For the type-II 2HDM corresponding to the second row of the Figs 7.5, 7.6 and 7.7 , the effective coupling d_q is not universal for up- and down-type quarks, the dependence of $\sigma^{\rm SI}$ on t_β is of a consequence of all the associated competing factors. $\sigma^{\rm SI}$ is the monotonically decreasing (increasing) function of t_β for $\alpha_{11}(\alpha_{22}) \neq 0$ case.

The conclusion as can be seen from these plots is that when $t_\beta = 0.2$ with α_{22} turned on, there is a viable dark matter starting with mass as low as ≈ 200GeV and when $t_\beta = 2$ with α_{11} nonzero, a dark matter with mass starting at ≈ 300GeV is available. For $\alpha_{12} \neq 0$, σ^{SI} gets minimum at $t_\beta = 0.18$ and 6.15. It is difficult to get viable parameter space for this case.

Another ingredient that might potentially mitigate the constraints from direct detection for lighter DM is the $2 \to 4$ annihilations induced from the effective interactions $\bar{\chi}\chi h_i h_j$ and $\bar{\chi}\chi H^+ H^-$ via off-shell intermediate scalars. These processes are not included in MicrOMEGAs but their effects are suppressed by the phase space and thus negligible with respect to the $2 \to 2$ annihilations. For a systematic exploration of the 2HDM parameter space with more phenomenological constraints taken into account, we defer to a future work.

7.2 DM Phenomenology (2): a special scenario

The invariance of the Higgs kinetic term under the $U(2)$ rotation in the space (Φ_1, Φ_2) leaves one the freedom to rotate the two Higgs doublets into any basis suitable for the study of the problem with model parameters connected by this transformation. There are two kinds of basis in the Higgs sector: generic basis and Higgs basis. Interactions of DM with Higgs sector given in Eq. (7.1) are written in the generic basis. Sometimes it is more convenient and useful to write down the effective DM-Higgs interactions in the Higgs basis. Assuming $\widehat{H}_1$ and $\widehat{H}_2$ are Higgs doublets in the Higgs basis, where $\langle \widehat{H}_1 \rangle = v/\sqrt{2}$ and $\langle \widehat{H}_2 \rangle = 0$, the relation between the Higgs basis and generic basis can be written as

$$\begin{pmatrix} \widehat{H}_1 \\ \widehat{H}_2 \end{pmatrix} = \begin{pmatrix} c_\beta & s_\beta \\ -s_\beta & c_\beta \end{pmatrix} \begin{pmatrix} \Phi_1 \\ \Phi_2 \end{pmatrix} . \tag{7.18}$$

We are interested in the case of Higgs portal DM where the direct detection cross section lies below the current LUX exclusion limit. As was showed that, both the freeze-in [140] and the "stealth" [76] DM scenarios have negligible direct detection cross section. In this section, we point out another possibility that may evade constraints of direct detection.

We assume the DM only couple to the Higgs bilinear $\widehat{H}_2^\dagger \widehat{H}_2$, where $\widehat{H}_2$ is the Higgs doublet that gets no VEV in the Higgs basis. The interaction takes the following form

$$\mathcal{L} \ni \frac{\alpha_{22}^{\rm HB}}{\Lambda}\bar{\chi}\chi \widehat{H}_2^\dagger \widehat{H}_2 \; , \tag{7.19}$$

while the interaction $\bar{\chi}\chi\widehat{H}_1^\dagger\widehat{H}_1$ reduces to the simple SM extension in Eq. (**??**) except that there are more diboson channels where DM may annihilate into. This interaction collects all the $\bar{\chi}\chi S_i S_j$ type terms where S_i represent scalars H, A^0 and $H^\pm$ in Eq. (7.1) in the alignment limit. Its coupling $\alpha_{22}^{\rm HB}$ is a linear combination of couplings α_{ij} in the generic basis

$$\alpha_{22}^{\rm HB} = \alpha_{11}s_\beta^2 - \alpha_{12}s_{2\beta} + \alpha_{22}c_\beta^2. \tag{7.20}$$

This scenario evades direct detection constraints at the tree level completely and can serve as a completely viable model easily. We thus study the implication of this interaction on the relic density. Furthermore, we include one-loop corrections to the Yukawa couplings of DM operator $\bar{\chi}\chi$ with CP-even Higgs h, H to study their direct detection signals.

Written in physical fields, the interactions associated with $\alpha_{22}^{\rm HB}$ are

$$\mathcal{L} \ni \frac{\alpha_{22}^{\rm HB}}{\Lambda}\bar{\chi}\chi\left\{H^+H^- + \frac{1}{2}A_0^2 + \frac{1}{4}[1+\cos(2\delta)]h^2 + \frac{1}{4}[1-\cos(2\delta)]H^2 + \frac{1}{2}hH\sin(2\delta)\right\} \tag{7.21}$$

where $\delta \equiv \alpha - \beta$. The absence of terms like $\bar{\chi}\chi h(H)$ in this equation leads to

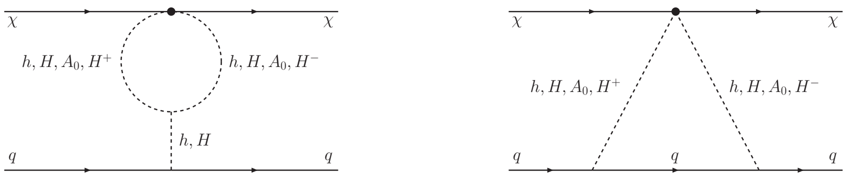

Figure 7.8: One loop Feynman diagrams contributing to DM-nucleon interactions.

a negligible $\sigma^{\rm SI}$ at tree level, and effective interactions of DM with quarks in the nucleon arise at the one-loop level. The relevant Feynman diagrams are given in Fig. 7.8, where the second one is doubley suppressed by the quark Yukwa couplings and is thus negligible. The first Feynman diagram generates effective operators $Y_h\bar{\chi}\chi h$ and $Y_H\bar{\chi}\chi H$ with

$$\begin{aligned} Y_h &= \frac{\alpha_{22}^{\rm HB}}{16\pi^2 v\Lambda}\left\{c_6 \ln\left(\frac{m_{H^\pm}^2}{\Lambda^2}\right) + c_2 \ln\left(\frac{m_A^2}{\Lambda^2}\right) + \frac{c_1}{2}(1+\cos 2\delta)\ln\left(\frac{m_h^2}{\Lambda^2}\right)\right. \\ &\left. +\frac{c_4}{2}(1-\cos 2\delta)\ln\left(\frac{m_H^2}{\Lambda^2}\right)\right\}, \end{aligned} \tag{7.22}$$

$$\begin{aligned} Y_H &= \frac{\alpha_{22}^{\rm HB}}{16\pi^2 v\Lambda}\left\{c_7 \ln\left(\frac{m_{H^\pm}^2}{\Lambda^2}\right) + c_3 \ln\left(\frac{m_A^2}{\Lambda^2}\right) + \frac{c_5}{2}(1-\cos 2\delta)\ln\left(\frac{m_H^2}{\Lambda^2}\right)\right. \\ &\left. + \frac{c_4}{2}\sin 2\delta\left[\ln\left(\frac{m_H^2}{\Lambda^2}\right) + \frac{m_h^2}{m_H^2-m_h^2}\ln\left(\frac{m_H^2}{m_h^2}\right) - 1\right]\right\}, \end{aligned} \tag{7.23}$$

So at one-loop level, we have only one scalar operator $\bar{\chi}\chi\bar{q}m_q q$ whose effective coupling d_q takes the following form,

$$\begin{aligned} d_q &= \frac{s_{\beta-\alpha}+k_q c_{\beta-\alpha}}{m_h^2 v}Y_h + \frac{c_{\beta-\alpha}-k_q s_{\beta-\alpha}}{m_H^2 v}Y_H \\ &\to \frac{1}{m_h^2 v}Y_h - \frac{k_q s_{\beta-\alpha}}{m_H^2 v}Y_H \end{aligned} \tag{7.24}$$

where we list in the second row the expression of d_q in the alignment limit. This d_q can be compared with the $d_q^{\rm SM}$. To that end, we show in Fig. 7.9 the ratio $d_q/d_q^{\rm SM}$ in the $t_\beta - \tilde{\nu}$ plane with $d_q^{\rm SM} \equiv \frac{\alpha^F}{\Lambda m_h^2}$ and $\alpha_{22}^{\rm HB} = \alpha^F$. Here the parameter $\tilde{\nu}$ controls the size of trilinear Higgs couplings in Table. 7.1. The plot in the left panel applies to all quarks in type-I 2HDM as well as up-type quarks in type-II 2HDM, while the plot in the right panel is for down-type quarks in type-II 2HDM. We can see for each plot, there is a contour where this ratio vanishes, that is, the one-loop SI cross section is exactly zero. This contour follows from the fact that both Y_H and Y_h are linear functions of $\tilde{\nu}$. For both cases this contour corresponds to $\tilde{\nu} \approx 2.5$. Away from this region, for the left plot, this ratio is not sensitive to t_β for $t_\beta > 1$, but sensitive to t_β for $t_\beta \lesssim 1$. This is because k_q is approaching to 0 for large t_β. The opposite situation happens for the second plot since now $k_q = -t_\beta$ and becomes dominant as t_β increases. The left plot shows relatively large one loop coupling around -0.34 for $t_\beta = 0.2$ while for $t_\beta = 2, 20$, they are both approximately -0.10. For the right plot, the ratio is around -0.10 for $t_\beta = 0.2$, -0.14 for $t_\beta = 2$ and -3.86 for $t_\beta = 20$. Due to the large values of loop corrections in certain parameter space of the model, these one loop diagrams might be important in DM direct detections even in the generic basis as given in the previous section. For the impact of these new ingredients and a full exploration of the 2HDM parameter space, we defer to a future analysis.

We show in Fig. 7.10 constraints from relic density and direct detection. The leftmost plot shows the allowed regions within three standard deviations of the Planck central value of $\Omega_c h^2$. It is done in the alignment limit then this contour applies to both type-I and -II 2HDM since only the invariant combination $\beta - \alpha$ appears in Eq. 7.21. Other inputs are set to be $t_\beta = 2$, $m_H = 400\text{GeV}$, $m_{A^0} = 300\text{GeV}$, $m_{H^\pm} = 500\text{GeV}$. In the middle and rightmost plots, we show the σ^{SI} with $\tilde{\nu} = 0$ and $\tilde{\nu} = 3$ respectively. The LUX exclusion regions are colored by light red and the relic density contours are colored by blue (green) for Type-I(II) 2HDM. We can see the $\tilde{\nu} = 0$ case has a fraction of parameter space excluded by LUX limits for relatively light dark matter while for $\tilde{\nu} = 3$, almost all of the parameter space evades the LUX exclusion limit. As discussed previously, as $\tilde{\nu} \approx 2.5$ one-loop cross section vanishes, resulting in null direct detection signals. It would be a completely viable scenario.

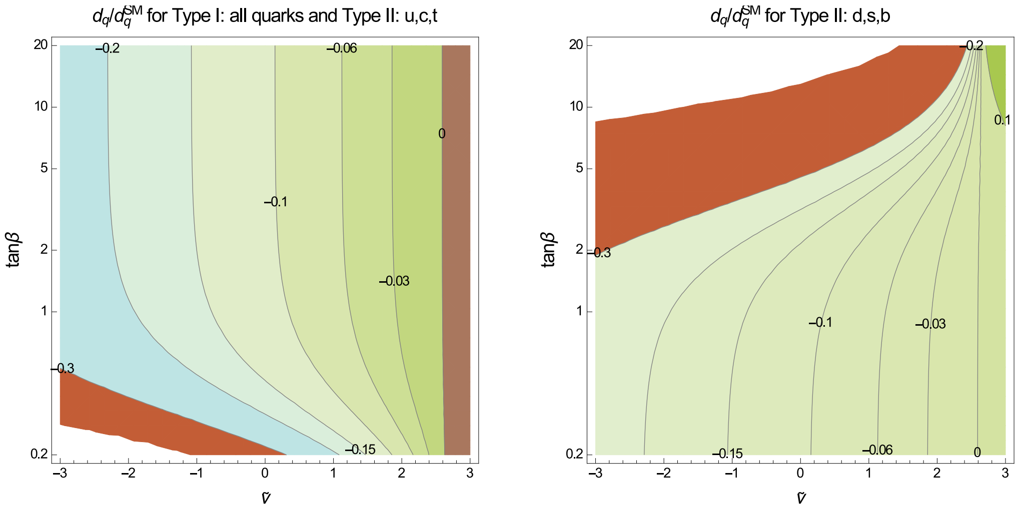

Figure 7.9: The ratio of the effective dark matter quark coupling in 2HDM to that in the SM $d_q/d_q^{\rm SM}$ for type I, II 2HDM in the $\tilde{\nu} - t_\beta$ plane in the alignment limit. The left plot applies to all quarks for type I 2HDM and to up type quarks in type II 2HDM since these Yukawa couplings have the same t_β dependence. The right plot applies to down type quarks for type II 2HDM. The other parameters are fixed to be $m_H = 400$GeV, $m_{A_0} = 300$GeV, $m_{H^\pm} = 500$GeV.

We finally comment on the DM phenomenology induced by deviations from the alignment limit and $2 \to 4$ annihilations. These effects are suppressed by $c_{\beta-\alpha}$ and limited phase space respectively, and would require quite large couplings to obtain the correct relic density. This however will lead to much larger direct detection cross section.

7.3 Summary

Accumulated evidences point to the existence of DM, which is claimed as one of the dark clouds in the sky of the particle physics in the twenty-first century. Since the discovery of the Higgs boson at the CERN LHC, the simplest Higgs portal fermionic DM model was almost excluded by the DM direct detection experiments. One needs extensions to the minimal model (with new interactions or new mediators) to accommodate the tension between the observed DM relic density and constraints of direct

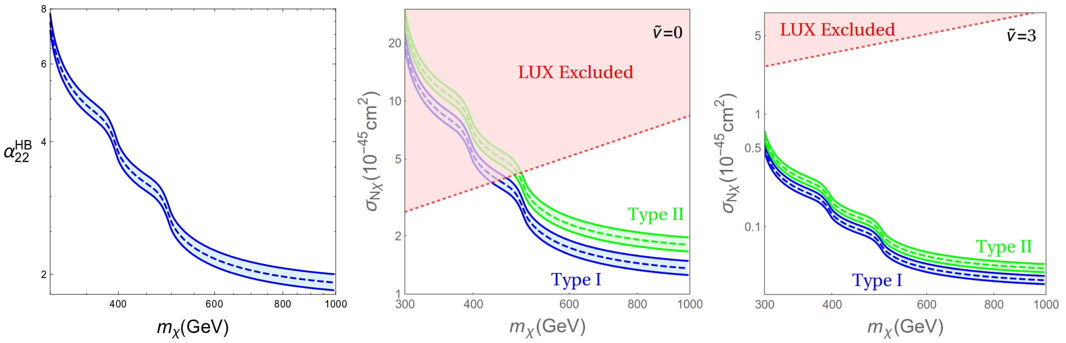

Figure 7.10: Relic density and LUX 2015 constraints in the SM limit. Left plot shows allowed regions in the $\alpha_{22}^{\rm HB} - m_\chi$ plane within three standard deviations of the relic density central value and applies to both type I and type II 2HDM. The middle and right plots shows dark matter nucleon spin-independent cross sections for type I and type II 2HDM with $\tilde{\nu} = 0$ and $\nu = 3$ respectively where the coupling $\alpha_{22}^{\rm HB}$ is fixed to satisfy the relic density requirements corresponding to the regions in the left plot. Also included in the middle and right plots are the LUX 2015 exclusion regions. The other parameters are fixed to be $t_\beta = 2$, $m_H = 400$GeV, $m_A = 300$GeV and $m_{H^\pm} = 500$GeV.

detections. In this paper we studied the phenomenology of the Higgs portal DM in the 2HDM model. In addition to the numerical simulations using the MciroMEGAs, the DM relic density and direct detection cross section were also calculated analytically for the benefit of generality. Our studies show that it is possible to get the observed Ωh^2, while satisfying constraints of $\sigma^{\rm SI}$ without introducing PV interactions in the both the Type-I and Type-II 2HDM. We studied the dependence of $\sigma^{\rm SI}$ on the t_β in detail, and pointed out the regime that satisfy the latest LUX bound for each scenario. We further pointed out an interesting scenario where there is no tree level contribution to the scattering of DM with nucleon. In this case it will be more promising to detect the DM resorting to the indirect detection or collider experiments, which, although interesting and important but beyond the reach of this paper, will be studied in another paper.

CHAPTER 8

CONCLUSION

The SM falls short in explaining the slight excess of ordinary baryonic matter over anti-matter as well as not providing a dark matter candidate. These are the two main reasons from the pragmatic point of view that motivate the studies in beyond SM explorations in this thesis.

To generate the baryon asymmetry, scenarios where there are new sources of CPV and where a strongly first order EWPT can be obtained are introduced within the framework of EWBG and are found to be able to generate the right baryon asymmetry while at the same time be compatible with other phenomenological constraints. In the years to come when many beyond SM theories would be subjected to stringent test from direct searches at the energy frontier and from precision measurements in the intensity frontier, the requirement as to properly account for the baryon asymmetry in the universe can be of significant guide on these searches and measurements. Current uncertainties in the BAU calculations is still relatively large and a systematic reduction of these uncertainties should be of even more priority as to complement the activities at the energy and precision frontier.

Dark matter as weakly interacting massive particles are also studied with the hope that future searches can shed light on this elusive particle people have been after for decades. Since current direct searches have push the dark matter scattering cross sections with nucleons to a much lower level without a positive signal, there might be some mechanism that these rates are indeed that small and we have studied here several examples with loop suppressed direct detection cross sections. Or it might be that our understanding of the micro-dynamics of dark matter interactions is not good enough. Especially, the the experimental limits on dark matter nucleon scattering were always limited to spin-independent or spin-dependent cases in the past. However it might be that the actual reactions have quite different nuclear responses and need us to reformulate the limits obtained. Effort torwards this direction is being made on the experimental side while on the theoretical side, this gives interesting new directions to study. Should new physics exists regarding these two long standing cosmological puzzles, we would some day have the chance to discover it.

APPENDIX

NUMERICAL ROUTINES

A.1 Introduction

In calculations of the EWBG framework, we need frequently to solve Sphaleron profiles, bounce solutions , transport equations, etc,. Fortunately these differential equations belong to the same class of problems, that is, the non-linear ordinary differential equations and their precise solutions can be obtained only using numerical solutions in most cases. Here we discuss the method used in solving these problems taking the transport equations as an example. Several specific cases are studied here and their numerical results are compared with those that can be obtained in Mathematica to check the correctness code developed.

We want to solve a set of coupled transport equations of the form

$$\partial_\mu J_r^\mu = -\sum_{s=0}^{N-1} \Gamma_{rs} n_s + S_r^{\mathrm{CPV}}, \qquad 0 \le r \le N-1,$$

with the following simplifying assumptions

$$\partial_\mu J_r^\mu \approx \frac{\partial n_r}{\partial t} + \vec{\nabla} \cdot \vec{J}_r \approx \frac{\partial n_r}{\partial t} - D_r \nabla^2 n_r \approx v_w \frac{dn_r}{dz} - D_r \frac{d^2 n_r}{dz^2}.$$

This type of second order ordinary differential equations(SODEs) can be solved analytically when the coefficients of n_r and its derivatives are z-independent. For transport equations, v_w and D_r are constants while Γ_r is z dependent. Then these equations need to be solved numerically.

These SODEs can be reduced trivially to a set of first order ODEs(FODEs),

$$n_r' = m_r, \tag{A.1}$$

$$m_r' - \frac{v_w}{D_r} m_r - \sum_s \frac{\Gamma_{rs}}{D_r} n_s + \frac{S_r^{\mathrm{CPV}}}{D_r} = 0, \tag{A.2}$$

with $0 \leq r \leq N-1$ and $n_r' \equiv \frac{dn_r}{dz}$. Thus numerical solutions to higher order ODEs are generally reduced to that of FODEs. There are other cases where these kinds of numerical routines are needed, such as solving Schrodinger equations, Sphaleron profiles etc,.

The numerical routines here is based on the "relaxation method" and two functions are developed in Mathematica. One function RelaxEWB is dedicated to above transport equations with specialized input format and the other one RelaxFODE solves generic coupled FODEs. To check the correctness of these two functions, we look at the cases where analytical solutions are available and those which can be solved by the Mathematica built-in function NDSolve for comparison. The examples are introduced by the simplest single equation with constant profiles and step by step more features are included with increasing complexities to approach solving a set of realistic transport equations. We also introduce the generally utilized "analytical approximation" in solving coupled transport equations and see how this approximation is approached by full numerical solutions.

A.2 Single Transport Equation with z-independent Profiles

A.2.1 $\bar{\Gamma}_H(z<0) = \bar{\Gamma}_H(z>0) =$ const

Most analytical approximation use the fact that coupled transport equations can be reduced to a single equation about H under various assumptions

$$\bar{D}_H H'' - v_w H' - \bar{\Gamma}_H H + \bar{S}_H = 0, \tag{A.3}$$

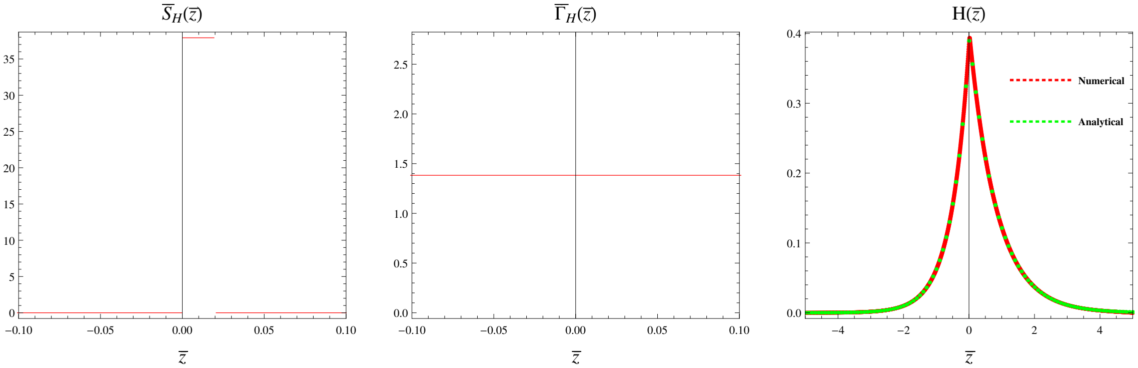

Figure A.1: Comparing numerical solutions of Eq. A.3 using functions RelaxEWB with exact analytical in Eq. A.4. Left and middle plots are input source and relaxation profiles. Right plot shows analytical and numerical solutions.

with boundary conditions $H(\pm\infty) = 0$. Now consider the case when this equation can be solved analytically corresponding to constant $\bar{\Gamma}_H$ for both $z > 0$ and $z < 0$. Analytically, this equation has an exact solution,

$$\begin{aligned} H(z) \; &= \; \left[c_+(0) - \frac{1}{\lambda_+ - \lambda_-} \frac{1}{\bar{D}_H} \int_0^z \bar{S}_H(u) e^{-\lambda_+ u} du \right] e^{\lambda_+ z}, \\ &+ \; \left[c_-(0) + \frac{1}{\lambda_+ - \lambda_-} \frac{1}{\bar{D}_H} \int_0^z \bar{S}_H(u) e^{-\lambda_- u} du \right] e^{\lambda_- z}, \end{aligned} \tag{A.4}$$

where $\lambda_\pm = \frac{v_w \pm \sqrt{v_w^2 + 4\bar{D}_H \bar{\Gamma}_H}}{2\bar{D}_H}$ with $\lambda_+ > 0$ and $\lambda_- < 0$. The two integration constants $c_\pm$ are determined by the boundary conditions $H(\pm\infty) = 0$,

$$c_+(0) = \frac{1}{\lambda_+ - \lambda_-} \frac{1}{\bar{D}_H} \int_0^\infty \bar{S}_H(u) e^{-\lambda_+ u} du, \tag{A.5}$$

$$c_-(0) = \frac{-1}{\lambda_+ - \lambda_-} \frac{1}{\bar{D}_H} \int_0^{-\infty} \bar{S}_H(u) e^{-\lambda_- u} du. \tag{A.6}$$

This analytical solution can be compared with numerical solutions using function RelaxEWB or RelaxFODE with the comparison shown in Fig. A.1 where the left and middle plots are input profiles for source and relaxation terms and the right plot shows solved H profiles both analytically(green) and numerically(red). We can see the numerical solution matches the anaytical solution very well.

A.2.2 $0 = \bar{\Gamma}_H(z < 0) \neq \bar{\Gamma}_H(z > 0) > 0$

In this case, we consider a more reliastic relaxation profile which is a step-function centered at $z = 0$ with $\bar{\Gamma}_H = 0$ in the symmetric phase($z < 0$) and a non-zero yet constant $\bar{\Gamma}_H$ in the broken phase($z > 0$). It follows that one need to solve Eq. A.3 separately in these two regions and match the solutions at $z = 0$ using continuity conditions.

Firstly for $z < 0$, we have $\bar{\lambda}_+ = \frac{v_w}{\bar{D}_H} > 0$ and $\bar{\lambda}_- = 0$, then

$$H(z)|_{z<0} = \left[c_+(0) - \frac{1}{\lambda_+}\frac{1}{\bar{D}_H}\int_0^z \bar{S}_H(u)e^{-\lambda_+ u}du\right]e^{\lambda_+ z} + \left[c_-(0) + \frac{1}{\lambda_+}\frac{1}{\bar{D}_H}\int_0^z \bar{S}_H(u)du\right], \tag{A.7}$$

with here $c_\pm(0)$ the two integration constants to be determined. Since $\bar{S}_H(z < 0) = 0$ in the symmetric phase, the above expression is simplified to

$$H(z)|_{z<0} = c_+(0)e^{\bar{\lambda}_+ z} + c_-(0). \tag{A.8}$$

Furthermore the boundary condition $H(-\infty) = 0$ requires that $c_-(0) = 0$, then we have the solution in the symmetric phase,

$$H(z)|_{z<0} = c_+(0)e^{\bar{\lambda}_+ z}, \tag{A.9}$$

with $c_+(0)$ now still undetermined.

In the broken phase corresponding to $z > 0$, the generic solution is

$$\begin{aligned} H(z)|_{z>0} = \quad & \left[B_+(0) - \frac{1}{\lambda_+ - \lambda_-}\frac{1}{\bar{D}_H}\int_0^z \bar{S}_H(u)e^{-\lambda_+ u}du\right]e^{\lambda_+ z}, \\ & + \left[B_-(0) + \frac{1}{\lambda_+ - \lambda_-}\frac{1}{\bar{D}_H}\int_0^z \bar{S}_H(u)e^{-\lambda_- u}du\right]e^{\lambda_- z}, \end{aligned} \tag{A.10}$$

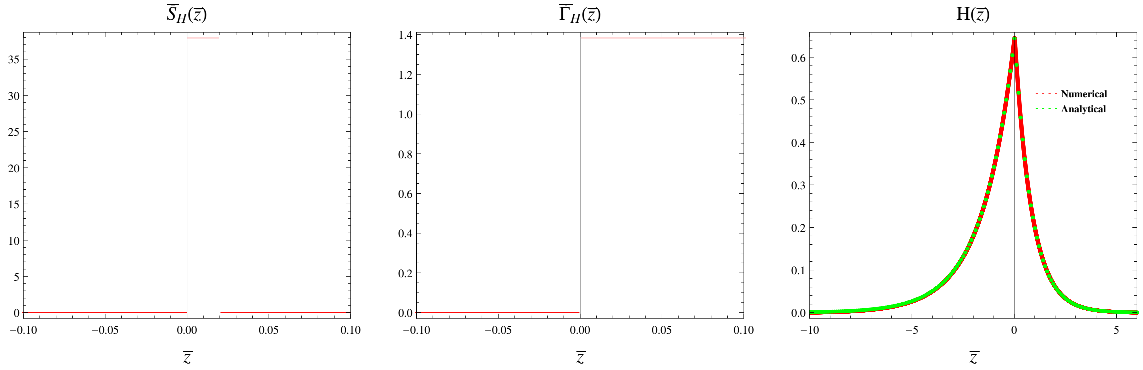

Figure A.2: Comparing numerical solution of Eq. A.3 with analytical solution relaxation profiles with $0 = \bar{\Gamma}_H(z < 0) \neq \bar{\Gamma}_H(z > 0) > 0$. Left and middle plots show source and relaxation profiles and the right plot shows numerical solution as well as exact analytical solution.

with here $\lambda_\pm$ defined similarly as previous case and where $B_+(0)$ is determined through the boundary condition at $+\infty$,

$$H(+\infty) = 0 \quad \Longrightarrow \quad B_+(0) = \frac{1}{\lambda_+ - \lambda_-}\frac{1}{\bar{D}_H}\int_0^\infty \bar{S}_H(u)e^{-\lambda_+ u}du, \tag{A.11}$$

leaving two remaining integration constants $c_+(0)$ and $B_-(0)$ which are now readily solved from the continuity conditions for the two set of solutions for $H(z)$ at $z = 0$,

$$\begin{array}{lcl} H(0)|_{z<0} = H(0)|_{z>0}, & \Longrightarrow & c_+(0) = \frac{\lambda_+ - \lambda_-}{\lambda_+}B_+(0), \\ \dot{H}(0)|_{z<0} = \dot{H}(0)|_{z>0} & & B_-(0) = -\frac{\lambda_-}{\lambda_+}B_+(0). \end{array} \tag{A.12}$$

The comparison of numerical solutions from RelaxEWB with above analytical solutions is shown in Fig. A.2 and again very good agreement is observed.

A.3 Single Transport Equation with Generic Profiles

Using generic z-dependent profiles for source and relaxation terms in Eq. A.3, we show numerical solutions from the dedicated RelaxEWB and the generic FODE function RelaxFODE with that from the Mathematica built-in NDSolve in Fig. A.3.

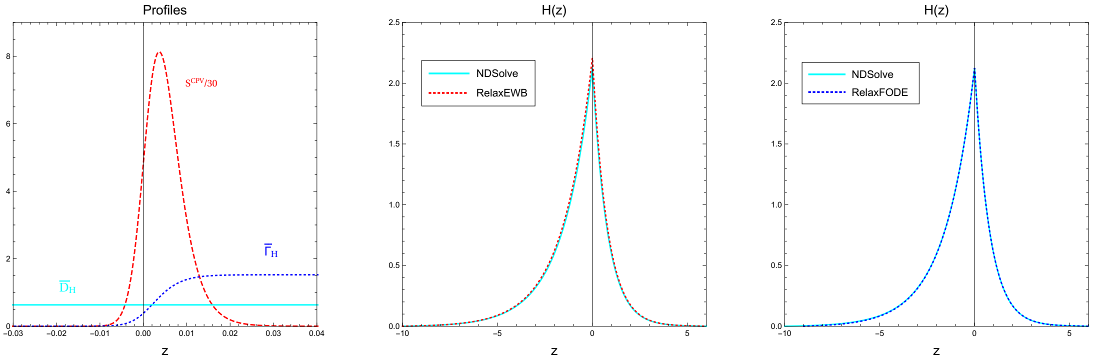

Figure A.3: Comparing numerical solutions of Eq. A.3 using RelaxEWB and RelaxFODE for generic z-depenent profiles respectively with the numerical solution from Mathematica built-in NDSolve. Left plot shows source(red dashed), diffusion constant(blue solid) and relaxation(blue dotted) profiles. The middle plot shows numerically solved $H(z)$ profiles from RelaxEWB(red dashed) and NDSolve(cyan). The middle plot shows numerically solved $H(z)$ profiles from RelaxFODE(blue dashed) and NDSolve(cyan).

The input profiles are shown in the left plot, the numerical solution from RelaxEWB as compared with that from NDSolve are shown in the middle plot and the numerical solutions from RelaxFODE as well as that from NDSolve are shown in the right plot. We can see the results from RelaxEWB and RelaxFODE agree with that from NDSolve.

A.4 Two Un-Coupled Transport Equations with Different Relaxation Profiles

To further test the correctness of the numerical routine RelaxEWB and RelaxFODE, we go beyond solving the single equation as in Eq. A.3 and study the following two uncoupled equations with different profiles,

$$\begin{aligned}\bar{D}_H H_1'' - v_w H_1' - \bar{\Gamma}_H H_1 + \bar{S}_H = 0,\\ \bar{D}_H H_2'' - v_w H_2' - 3\bar{\Gamma}_H H_2 + \bar{S}_H = 0,\end{aligned} \tag{A.13}$$

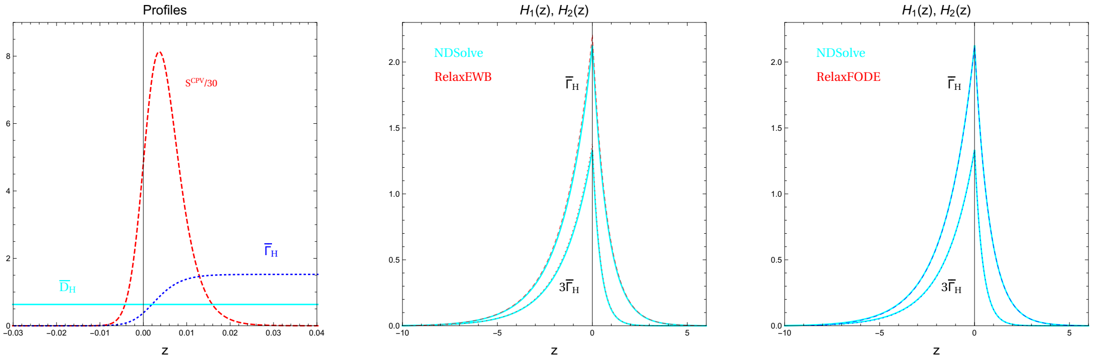

Figure A.4: Numerical solutions of two un-coupled transport equations A.13 with different relaxation profiles using RelaxEWB and RelaxFODE as compared with that of NDSolve in the middle(for RelaxEWB) and right(for RelaxFODE) plots respectively. The left plot shows the input profiles.

where the two equations differ by their relaxation profiles with $\bar{\Gamma}_{H_2} = 3\bar{\Gamma}_{H_1}$. The numerical results for $H_1(z)$, $H_2(z)$ from RelaxEWB and RelaxFODE are compared with that from NDSolve in Fig. A.4. From the middle plot we can see the results of RelaxEWB(red dotted) matches that from NDSolve(cyan) and from the right plot, it is clear the result from RelaxFODE(red dotted) also mathes that from NDSolve(cyan).

A.5 Two Coupled Transport Equations with Reduced Mixing

Now we move one step forward and consider the two coupled transport equations with reduced mixing relaxation profiles,

$$\begin{aligned} \bar{D}_H H_1'' - v_w H_1' - \bar{\Gamma}_H H_1 - 0.7\bar{\Gamma}_H H_2 + \bar{S}_H &= 0, \\ \bar{D}_H H_2'' - v_w H_2' - 3\bar{\Gamma}_H H_2 - 0.7\bar{\Gamma}_H H_1 + \bar{S}_H &= 0. \end{aligned} \tag{A.14}$$

The only difference with previous Eq. A.13 is that we added a mixing relaxation profile for each of two equations but with reduced strength. This different types of

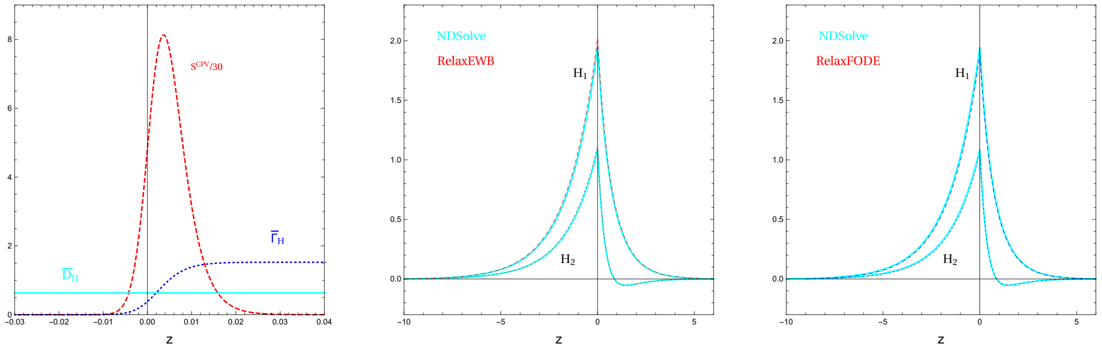

Figure A.5: Two coupled equations with reduced off-diagonal relaxation rates. As with previous figures, the left one shows the input profiles of the transport equations while the middle and the right one give the obtained results using different methods.

equations can further test the correctness of the numerical routine RelaxEWB and RelaxFODE.

Before showing the numerical results, we study the asymptotic behavior around $z \to \pm\infty$ and see if both H_1 and H_2 admit a solution with vanishing strength. More precisely we seek the following solutions for H_1, H_2 at $z \to \pm\infty$,

$$H_i(\pm\infty) = \sum_{n=0}^{\infty} \frac{a_{in}}{|z|^n} \quad \text{with} \quad i = 1, 2,$$

which when plugged into Eq. A.14 gives at leading order of $|z|^{-1}$,

$$\bar{\Gamma}_H \begin{bmatrix} 1 & 0.7 \\ 0.7 & 3 \end{bmatrix} \begin{bmatrix} H_1 \\ H_2 \end{bmatrix} = \begin{bmatrix} \bar{S}_H \\ \bar{S}_H \end{bmatrix} = \begin{bmatrix} 0 \\ 0 \end{bmatrix} \quad \Rightarrow \quad \begin{cases} H_1(\pm\infty) = 0 \\ H_2(\pm\infty) = 0 \end{cases}$$

So we are guaranteed that there are solutions of the type we want. Now we show the numerical results from RelaxEWB and RelaxFODE and compare with result using NDSolve in Fig. A.5. There the left plot shows input profiles, the middle plot compares result from RelaxEWB with that of NDSolve and the right plot compares result from RelaxFODE with NDSolve. We can see both RelaxEWB and RelaxFODE agree with NDSolve.

From these above examples we should be pretty confident that the numerical solutions from RelaxEWB and RelaxFODE are correct.

BIBLIOGRAPHY

[1] Search for New Phenomena in Monojet plus Missing Transverse Momentum Final States using 10fb-1 of pp Collisions at sqrts=8 TeV with the ATLAS detector at the LHC. Tech. Rep. ATLAS-CONF-2012-147, CERN, Geneva, Nov 2012.

[2] Aad, Georges, et al. Search for new phenomena with the monojet and missing transverse momentum signature using the ATLAS detector in $\sqrt{s} = 7$ TeV proton-proton collisions. *Phys.Lett. B705* (2011), 294–312.

[3] Aad, Georges, et al. Observation of a new particle in the search for the Standard Model Higgs boson with the ATLAS detector at the LHC. *Phys. Lett. B716* (2012), 1–29.

[4] Aad, Georges, et al. Search for dark matter candidates and large extra dimensions in events with a jet and missing transverse momentum with the ATLAS detector. *JHEP 1304* (2013), 075.

[5] Aad, Georges, et al. Measurement of Higgs boson production in the diphoton decay channel in pp collisions at center-of-mass energies of 7 and 8 TeV with the ATLAS detector. *Phys. Rev. D90*, 11 (2014), 112015.

[6] Aad, Georges, et al. Combined Measurement of the Higgs Boson Mass in pp Collisions at $\sqrt{s} = 7$ and 8 TeV with the ATLAS and CMS Experiments. *Phys. Rev. Lett. 114* (2015), 191803.

[7] Aad, Georges, et al. Evidence for the Higgs-boson Yukawa coupling to tau leptons with the ATLAS detector. *JHEP 04* (2015), 117.

[8] Aad, Georges, et al. Search for lepton-flavour-violating $H \to \mu\tau$ decays of the Higgs boson with the ATLAS detector.

[9] Aad, Georges, et al. Search for lepton-flavour-violating decays of the Higgs and Z bosons with the ATLAS detector.

[10] Abdallah, Jalal, Ashkenazi, Adi, Boveia, Antonio, Busoni, Giorgio, De Simone, Andrea, et al. Simplified Models for Dark Matter and Missing Energy Searches at the LHC.

[11] Abe, Tomohiro, Hisano, Junji, Kitahara, Teppei, and Tobioka, Kohsaku. Gauge invariant Barr-Zee type contributions to fermionic EDMs in the two-Higgs doublet models. *JHEP 01* (2014), 106.

[12] Ackermann, M., et al. Measurement of separate cosmic-ray electron and positron spectra with the Fermi Large Area Telescope. *Phys. Rev. Lett. 108* (2012), 011103.

[13] Adam, R., et al. Planck 2015 results. I. Overview of products and scientific results.

[14] Ade, P. A. R., et al. Planck 2015 results. XIII. Cosmological parameters.

[15] Affleck, Ian, and Dine, Michael. A New Mechanism for Baryogenesis. *Nucl. Phys. B249* (1985), 361–380.

[16] Agrawal, Prateek, Batell, Brian, Hooper, Dan, and Lin, Tongyan. Flavored Dark Matter and the Galactic Center Gamma-Ray Excess.

[17] Agrawal, Prateek, Blanchet, Steve, Chacko, Zackaria, and Kilic, Can. Flavored Dark Matter, and Its Implications for Direct Detection and Colliders. *Phys. Rev. D86* (2012), 055002.

[18] Agrawal, Prateek, Blanke, Monika, and Gemmler, Katrin. Flavored dark matter beyond Minimal Flavor Violation. *JHEP 10* (2014), 72.

[19] Agrawal, Prateek, Chacko, Zackaria, Kilic, Can, and Verhaaren, Christopher B. A Couplet from Flavored Dark Matter. *JHEP 08* (2015), 072.

[20] Akerib, D. S., et al. Improved WIMP scattering limits from the LUX experiment.

[21] Akiba, T., Kikuchi, H., and Yanagida, T. Static Minimum Energy Path From a Vacuum to a Sphaleron in the Weinberg-Salam Model. *Phys. Rev. D38* (1988), 1937–1941.

[22] Alves, Daniele, et al. Simplified Models for LHC New Physics Searches. *J.Phys. G39* (2012), 105005.

[23] Amhis, Y., et al. Averages of B-Hadron, C-Hadron, and tau-lepton properties as of early 2012.

[24] Anand, Nikhil, Fitzpatrick, A. Liam, and Haxton, W. C. Weakly interacting massive particle-nucleus elastic scattering response. *Phys. Rev. C89*, 6 (2014), 065501.

[25] Aoki, Mayumi, Kanemura, Shinya, Tsumura, Koji, and Yagyu, Kei. Models of Yukawa interaction in the two Higgs doublet model, and their collider phenomenology. *Phys.Rev. D80* (2009), 015017.

[26] Arina, Chiara, Hamann, Jan, and Wong, Yvonne Y. Y. A Bayesian view of the current status of dark matter direct searches. *JCAP 1109* (2011), 022.

[27] Arnold, Peter Brockway, and McLerran, Larry D. Sphalerons, Small Fluctuations and Baryon Number Violation in Electroweak Theory. *Phys. Rev. D36* (1987), 581.

[28] Arnold, Peter Brockway, and McLerran, Larry D. The Sphaleron Strikes Back. *Phys. Rev. D37* (1988), 1020.

[29] Aubert, Bernard, et al. Searches for Lepton Flavor Violation in the Decays $\tau^+ \to e^+\gamma$ and $\tau^+ \to \mu^+\gamma$. *Phys. Rev. Lett. 104* (2010), 021802.

[30] Bachas, Constantin, and Tomaras, Theodore. Band Structure in Yang-Mills Theories. *JHEP 05* (2016), 143.

[31] Bai, Yang, and Berger, Joshua. Fermion Portal Dark Matter. *JHEP 11* (2013), 171.

[32] Bai, Yang, and Berger, Joshua. Lepton Portal Dark Matter. *JHEP 08* (2014), 153.

[33] Bai, Yang, Fox, Patrick J., and Harnik, Roni. The Tevatron at the Frontier of Dark Matter Direct Detection. *JHEP 1012* (2010), 048.

[34] Bakshi, Pradip M., and Mahanthappa, Kalyana T. Expectation value formalism in quantum field theory. 1. *J. Math. Phys. 4* (1963), 1–11.

[35] Bakshi, Pradip M., and Mahanthappa, Kalyana T. Expectation value formalism in quantum field theory. 2. *J. Math. Phys. 4* (1963), 12–16.

[36] Baltz, E. A., and Bergstrom, L. Detection of leptonic dark matter. *Phys. Rev. D67* (2003), 043516.

[37] Barger, Vernon D., Hewett, J.L., and Phillips, R.J.N. New Constraints on the Charged Higgs Sector in Two Higgs Doublet Models. *Phys.Rev. D41* (1990), 3421–3441.

[38] Barger, Vernon, Langacker, Paul, McCaskey, Mathew, Ramsey-Musolf, Michael J., and Shaughnessy, Gabe. LHC Phenomenology of an Extended Standard Model with a Real Scalar Singlet. *Phys.Rev. D77* (2008), 035005.

[39] Baron, Jacob, et al. Order of Magnitude Smaller Limit on the Electric Dipole Moment of the Electron. *Science 343* (2014), 269–272.

[40] Barr, Stephen M., and Zee, A. Electric Dipole Moment of the Electron and of the Neutron. *Phys. Rev. Lett. 65* (1990), 21–24. [Erratum: Phys. Rev. Lett.65,2920(1990)].

[41] Batell, Brian, Lin, Tongyan, and Wang, Lian-Tao. Flavored Dark Matter and R-Parity Violation. *JHEP 01* (2014), 075.

[42] Belanger, G., Boudjema, F., Pukhov, A., and Semenov, A. MicrOMEGAs: A Program for calculating the relic density in the MSSM. *Comput.Phys.Commun. 149* (2002), 103–120.

[43] Belanger, G., Boudjema, F., Pukhov, A., and Semenov, A. MicrOMEGAs 2.0: A Program to calculate the relic density of dark matter in a generic model. *Comput. Phys. Commun. 176* (2007), 367–382.

[44] Belanger, G., Boudjema, F., Pukhov, A., and Semenov, A. Dark matter direct detection rate in a generic model with micrOMEGAs 2.2. *Comput. Phys. Commun. 180* (2009), 747–767.

[45] Belanger, G., Boudjema, F., Pukhov, A., and Semenov, A. micrOMEGAs 3: A program for calculating dark matter observables. *Comput.Phys.Commun. 185* (2014), 960–985.

[46] Belavin, A. A., Polyakov, Alexander M., Schwartz, A. S., and Tyupkin, Yu. S. Pseudoparticle Solutions of the Yang-Mills Equations. *Phys. Lett. B59* (1975), 85–87.

[47] Beltran, Maria, Hooper, Dan, Kolb, Edward W., Krusberg, Zosia A.C., and Tait, Tim M.P. Maverick dark matter at colliders. *JHEP 1009* (2010), 037.

[48] Belyaev, Alexander, Christensen, Neil D., and Pukhov, Alexander. CalcHEP 3.4 for collider physics within and beyond the Standard Model. *Comput. Phys. Commun. 184* (2013), 1729–1769.

[49] Berge, Stefan, Bernreuther, Werner, and Kirchner, Sebastian. Prospects of constraining the Higgs bosons CP nature in the tau decay channel at the LHC. *Phys. Rev. D92*, 9 (2015), 096012.

[50] Bernstein, Jeremy, Brown, Lowell S., and Feinberg, Gerald. The Cosmological Heavy Neutrino Problem Revisited. *Phys.Rev. D32* (1985), 3261.

[51] Bertone, Gianfranco, Hooper, Dan, and Silk, Joseph. Particle dark matter: Evidence, candidates and constraints. *Phys. Rept. 405* (2005), 279–390.

[52] Blanke, Monika, Buras, Andrzej J., Gemmler, Katrin, and Heidsieck, Tillmann. Delta F = 2 observables and $B \to X_q\gamma$ decays in the Left-Right Model: Higgs particles striking back. *JHEP 1203* (2012), 024.

[53] Blanke, Monika, Shakya, Bibhushan, Tanedo, Philip, and Tsai, Yuhsin. The Birds and the Bs in RS: The $btos\gamma$ penguin in a warped extra dimension. *JHEP 1208* (2012), 038.

[54] Bochkarev, A. I., and Shaposhnikov, M. E. Electroweak Production of Baryon Asymmetry and Upper Bounds on the Higgs and Top Masses. *Mod. Phys. Lett. A2* (1987), 417.

[55] Bodeker, D., Moore, Guy D., and Rummukainen, K. Chern-Simons number diffusion and hard thermal loops on the lattice. *Phys. Rev. D61* (2000), 056003.

[56] Botella, F.J., Branco, G.C., Carmona, Adrian, Nebot, M., Pedro, Leonardo, et al. Physical Constraints on a Class of Two-Higgs Doublet Models with FCNC at tree level.

[57] Botella, F.J., and Silva, Joao P. Jarlskog - like invariants for theories with scalars and fermions. *Phys.Rev. D51* (1995), 3870–3875.

[58] Bowser-Chao, David, Chang, Darwin, and Keung, Wai-Yee. Electron electric dipole moment from CP violation in the charged Higgs sector. *Phys. Rev. Lett. 79* (1997), 1988–1991.

[59] Branco, G.C., Ferreira, P.M., Lavoura, L., Rebelo, M.N., Sher, Marc, et al. Theory and phenomenology of two-Higgs-doublet models. *Phys.Rept. 516* (2012), 1–102.

[60] Branco, Gustavo C., Lavoura, Luis, and Silva, Joao P. CP Violation. *Int. Ser. Monogr. Phys. 103* (1999), 1–536.

[61] Buchmueller, Oliver, Dolan, Matthew J., Malik, Sarah A., and McCabe, Christopher. Characterising dark matter searches at colliders and direct detection experiments: Vector mediators. *JHEP 1501* (2015), 037.

[62] Buchmuller, W., Peccei, R. D., and Yanagida, T. Leptogenesis as the origin of matter. *Ann. Rev. Nucl. Part. Sci. 55* (2005), 311–355.

[63] Buras, Andrzej J. Weak Hamiltonian, CP violation and rare decays. 281–539.

[64] Buras, Andrzej J., Jager, Sebastian, and Urban, Jorg. Master formulae for Delta F=2 NLO QCD factors in the standard model and beyond. *Nucl.Phys. B605* (2001), 600–624.

[65] Buras, Andrzej J., Merlo, Luca, and Stamou, Emmanuel. The Impact of Flavour Changing Neutral Gauge Bosons on $\bar{B}X_s\gamma$. *JHEP 1108* (2011), 124.

[66] Cai, Yi, and Chao, Wei. The Higgs Seesaw Induced Neutrino Masses and Dark Matter. *Phys. Lett. B749* (2015), 458–463.

[67] Calibbi, Lorenzo, Crivellin, Andreas, and Zaldvar, Bryan. Flavor portal to dark matter. *Phys. Rev. D92*, 1 (2015), 016004.

[68] Cao, Qing-Hong, Chen, Chuan-Ren, Li, Chong Sheng, and Zhang, Hao. Effective Dark Matter Model: Relic density, CDMS II, Fermi LAT and LHC. *JHEP 1108* (2011), 018.

[69] Carena, Marcela, Low, Ian, and Wagner, Carlos E. M. Implications of a Modified Higgs to Diphoton Decay Width. *JHEP 08* (2012), 060.

[70] Carena, Marcela S., Moreno, J.M., Quiros, M., Seco, M., and Wagner, C.E.M. Supersymmetric CP violating currents and electroweak baryogenesis. *Nucl.Phys. B599* (2001), 158–184.

[71] Carena, Marcela S., Quiros, M., Seco, M., and Wagner, C.E.M. Improved results in supersymmetric electroweak baryogenesis. *Nucl.Phys. B650* (2003), 24–42.

[72] Catena, Riccardo, and Gondolo, Paolo. Global fits of the dark matter-nucleon effective interactions. *JCAP 1409*, 09 (2014), 045.

[73] Chang, D., Hou, W. S., and Keung, Wai-Yee. Two loop contributions of flavor changing neutral Higgs bosons to mu —¿ e gamma. *Phys. Rev. D48* (1993), 217–224.

[74] Chang, Spencer, Edezhath, Ralph, Hutchinson, Jeffrey, and Luty, Markus. Leptophilic Effective WIMPs. *Phys. Rev. D90*, 1 (2014), 015011.

[75] Chao, Wei. Pure Leptonic Gauge Symmetry, Neutrino Masses and Dark Matter. *Phys. Lett. B695* (2011), 157–161.

[76] Chao, Wei. Hiding Scalar Higgs Portal Dark Matter.

[77] Chatrchyan, Serguei, et al. Search for New Physics with a Mono-Jet and Missing Transverse Energy in pp Collisions at $\sqrt{s} = 7$ TeV. *Phys.Rev.Lett. 107* (2011), 201804.

[78] Chatrchyan, Serguei, et al. Observation of a new boson at a mass of 125 GeV with the CMS experiment at the LHC. *Phys. Lett. B716* (2012), 30–61.

[79] Chatrchyan, Serguei, et al. Search for dark matter and large extra dimensions in monojet events in pp collisions at $\sqrt{s} = 7$ TeV. *JHEP 1209* (2012), 094.

[80] Chatrchyan, Serguei, et al. Evidence for the 125 GeV Higgs boson decaying to a pair of τ leptons. *JHEP 05* (2014), 104.

[81] Chen, Mu-Chun, Huang, Jinrui, and Takhistov, Volodymyr. Beyond Minimal Lepton Flavored Dark Matter. *JHEP 02* (2016), 060.

[82] Cheung, Clifford, and Sanford, David. Simplified Models of Mixed Dark Matter. *JCAP 1402* (2014), 011.

[83] Cheung, Kingman, Tseng, Po-Yan, Tsai, Yue-Lin S., and Yuan, Tzu-Chiang. Global Constraints on Effective Dark Matter Interactions: Relic Density, Direct Detection, Indirect Detection, and Collider. *JCAP 1205* (2012), 001.

[84] Cheung, Kingman, Tseng, Po-Yan, and Yuan, Tzu-Chiang. Cosmic Antiproton Constraints on Effective Interactions of the Dark Matter. *JCAP 1101* (2011), 004.

[85] Cheung, Kingman, Tseng, Po-Yan, and Yuan, Tzu-Chiang. Gamma-ray Constraints on Effective Interactions of the Dark Matter. *JCAP 1106* (2011), 023.

[86] Chou, Kuang-chao, Su, Zhao-bin, Hao, Bai-lin, and Yu, Lu. Equilibrium and Nonequilibrium Formalisms Made Unified. *Phys. Rept. 118* (1985), 1.

[87] Chung, Daniel J. H., Garbrecht, Bjorn, Ramsey-Musolf, Michael J., and Tulin, Sean. Yukawa Interactions and Supersymmetric Electroweak Baryogenesis. *Phys. Rev. Lett. 102* (2009), 061301.

[88] Chung, Daniel J.H., Garbrecht, Bjorn, Ramsey-Musolf, Michael J., and Tulin, Sean. Lepton-mediated electroweak baryogenesis. *Phys.Rev. D81* (2010), 063506.

[89] Cirelli, Marco, Del Nobile, Eugenio, and Panci, Paolo. Tools for model-independent bounds in direct dark matter searches. *JCAP 1310* (2013), 019.

[90] Cirigliano, Vincenzo, Lee, Christopher, Ramsey-Musolf, Michael J., and Tulin, Sean. Flavored Quantum Boltzmann Equations. *Phys. Rev. D81* (2010), 103503.

[91] Cirigliano, Vincenzo, Lee, Christopher, and Tulin, Sean. Resonant Flavor Oscillations in Electroweak Baryogenesis. *Phys. Rev. D84* (2011), 056006.

[92] Cirigliano, Vincenzo, Ramsey-Musolf, Michael J., Tulin, Sean, and Lee, Christopher. Yukawa and tri-scalar processes in electroweak baryogenesis. *Phys. Rev. D73* (2006), 115009.

[93] Cline, James M. Baryogenesis. In *Les Houches Summer School - Session 86: Particle Physics and Cosmology: The Fabric of Spacetime Les Houches, France, July 31-August 25, 2006* (2006).

[94] Cline, James M., Joyce, Michael, and Kainulainen, Kimmo. Supersymmetric electroweak baryogenesis. *JHEP 0007* (2000), 018.

[95] Cline, James M., Kainulainen, Kimmo, and Trott, Michael. Electroweak Baryogenesis in Two Higgs Doublet Models and B meson anomalies. *JHEP 11* (2011), 089.

[96] Cohen, Andrew G., Kaplan, David B., and Nelson, Ann E. WEAK SCALE BARYOGENESIS. *Phys. Lett. B245* (1990), 561–564.

[97] Cohen, Andrew G., Kaplan, David B., and Nelson, Ann E. Baryogenesis at the weak phase transition. *Nucl. Phys. B349* (1991), 727–742.

[98] Cohen, Andrew G., Kaplan, D.B., and Nelson, A.E. Diffusion enhances spontaneous electroweak baryogenesis. *Phys.Lett. B336* (1994), 41–47.

[99] Cohen, Timothy, and Zurek, Kathryn M. Leptophilic Dark Matter from the Lepton Asymmetry. *Phys. Rev. Lett. 104* (2010), 101301.

[100] Csikor, F., Fodor, Z., Hegedus, P., Jakovac, A., Katz, S. D., and Piroth, A. Electroweak phase transition in the MSSM: 4-Dimensional lattice simulations. *Phys. Rev. Lett. 85* (2000), 932–935.

[101] D'Ambrosio, G., Giudice, G.F., Isidori, G., and Strumia, A. Minimal flavor violation: An Effective field theory approach. *Nucl.Phys. B645* (2002), 155–187.

[102] Das, Ashok K. *Finite Temperature Field Theory.* World Scientific, New York, 1997.

[103] DiFranzo, Anthony, Nagao, Keiko I., Rajaraman, Arvind, and Tait, Tim M. P. Simplified Models for Dark Matter Interacting with Quarks. *JHEP 11* (2013), 014. [Erratum: JHEP01,162(2014)].

[104] Dine, Michael, Randall, Lisa, and Thomas, Scott D. Supersymmetry breaking in the early universe. *Phys. Rev. Lett. 75* (1995), 398–401.

[105] Dine, Michael, Randall, Lisa, and Thomas, Scott D. Baryogenesis from flat directions of the supersymmetric standard model. *Nucl. Phys. B458* (1996), 291–326.

[106] D'Onofrio, Michela, Rummukainen, Kari, and Tranberg, Anders. The Sphaleron Rate through the Electroweak Cross-over. *JHEP 08* (2012), 123.

[107] D'Onofrio, Michela, Rummukainen, Kari, and Tranberg, Anders. Sphaleron Rate in the Minimal Standard Model. *Phys. Rev. Lett. 113*, 14 (2014), 141602.

[108] Donoghue, J. F., Golowich, E., and Holstein, Barry R. Dynamics of the standard model. *Camb. Monogr. Part. Phys. Nucl. Phys. Cosmol. 2* (1992), 1–540.

[109] Dorsch, G. C., Huber, S. J., Mimasu, K., and No, J. M. Echoes of the Electroweak Phase Transition: Discovering a second Higgs doublet through $A_0 \to ZH_0$. *Phys. Rev. Lett. 113*, 21 (2014), 211802.

[110] Dorsch, G. C., Huber, S. J., and No, J. M. A strong electroweak phase transition in the 2HDM after LHC8. *JHEP 10* (2013), 029.

[111] Dunietz, I., Greenberg, O.W., and Wu, Dan-di. A Priori Definition of Maximal CP Violation. *Phys.Rev.Lett. 55* (1985), 2935.

[112] Dunne, Gerald V., and Min, Hyunsoo. Beyond the thin-wall approximation: Precise numerical computation of prefactors in false vacuum decay. *Phys. Rev. D72* (2005), 125004.

[113] Ellis, John, Sakurai, Kazuki, and Spannowsky, Michael. Search for Sphalerons: IceCube vs. LHC. *JHEP 05* (2016), 085.

[114] Eriksson, David, Rathsman, Johan, and Stal, Oscar. 2HDMC: Two-Higgs-Doublet Model Calculator Physics and Manual. *Comput.Phys.Commun. 181* (2010), 189–205.

[115] Fan, JiJi, Reece, Matthew, and Wang, Lian-Tao. Non-relativistic effective theory of dark matter direct detection. *JCAP 1011* (2010), 042.

[116] Fedderke, Michael A., Chen, Jing-Yuan, Kolb, Edward W., and Wang, Lian-Tao. The Fermionic Dark Matter Higgs Portal: an effective field theory approach. *JHEP 08* (2014), 122.

[117] Feng, Lei, Profumo, Stefano, and Ubaldi, Lorenzo. Closing in on singlet scalar dark matter: LUX, invisible Higgs decays and gamma-ray lines. *JHEP 03* (2015), 045.

[118] Fidler, Christian, Herranen, Matti, Kainulainen, Kimmo, and Rahkila, Pyry Matti. Flavoured quantum Boltzmann equations from cQPA. *JHEP 02* (2012), 065.

[119] Fitzpatrick, A. Liam, Haxton, Wick, Katz, Emanuel, Lubbers, Nicholas, and Xu, Yiming. Model Independent Direct Detection Analyses.

[120] Fitzpatrick, A. Liam, Haxton, Wick, Katz, Emanuel, Lubbers, Nicholas, and Xu, Yiming. The Effective Field Theory of Dark Matter Direct Detection. *JCAP 1302* (2013), 004.

[121] Fox, Patrick J., Harnik, Roni, Kopp, Joachim, and Tsai, Yuhsin. Missing Energy Signatures of Dark Matter at the LHC. *Phys.Rev. D85* (2012), 056011.

[122] Freitas, Ayres, and Westhoff, Susanne. Leptophilic Dark Matter in Lepton Interactions at LEP and ILC. *JHEP 10* (2014), 116.

[123] Fromme, Lars, Huber, Stephan J., and Seniuch, Michael. Baryogenesis in the two-Higgs doublet model. *JHEP 0611* (2006), 038.

[124] Fukugita, M., and Yanagida, T. Baryogenesis Without Grand Unification. *Phys. Lett. B174* (1986), 45–47.

[125] Funakubo, Koichi, and Senaha, Eibun. Electroweak phase transition, critical bubbles and sphaleron decoupling condition in the MSSM. *Phys. Rev. D79* (2009), 115024.

[126] Fuyuto, Kaori, and Senaha, Eibun. Sphaleron and critical bubble in the scale invariant two Higgs doublet model. *Phys. Lett. B747* (2015), 152–157.

[127] Gavela, M. B., Hernandez, P., Orloff, J., and Pene, O. Standard model CP violation and baryon asymmetry. *Mod. Phys. Lett. A9* (1994), 795–810.

[128] Gavela, M.B., Hernandez, P., Orloff, J., Pene, O., and Quimbay, C. Standard model CP violation and baryon asymmetry. Part 2: Finite temperature. *Nucl.Phys. B430* (1994), 382–426.

[129] Gibbons, Gary W., Gielen, Steffen, Pope, C.N., and Turok, Neil. Measures on Mixing Angles. *Phys.Rev. D79* (2009), 013009.

[130] Giudice, G. F., and Shaposhnikov, Mikhail E. Strong sphalerons and electroweak baryogenesis. *Phys. Lett. B326* (1994), 118–124.

[131] Glashow, Sheldon L., and Weinberg, Steven. Natural Conservation Laws for Neutral Currents. *Phys.Rev. D15* (1977), 1958.

[132] Gondolo, Paolo, and Gelmini, Graciela. Cosmic abundances of stable particles: Improved analysis. *Nucl.Phys. B360* (1991), 145–179.

[133] Goodman, Jessica, Ibe, Masahiro, Rajaraman, Arvind, Shepherd, William, Tait, Tim M.P., et al. Constraints on Dark Matter from Colliders. *Phys.Rev. D82* (2010), 116010.

[134] Goodman, Jessica, Ibe, Masahiro, Rajaraman, Arvind, Shepherd, William, Tait, Tim M.P., et al. Constraints on Light Majorana dark Matter from Colliders. *Phys.Lett. B695* (2011), 185–188.

[135] Graham, Peter W., Rajendran, Surjeet, Van Tilburg, Ken, and Wiser, Timothy D. Towards a Bullet-proof test for indirect signals of dark matter.

[136] Gresham, Moira I., and Zurek, Kathryn M. Effect of nuclear response functions in dark matter direct detection. *Phys. Rev. D89*, 12 (2014), 123521.

[137] Grimus, W., Lavoura, L., Ogreid, O.M., and Osland, P. A Precision constraint on multi-Higgs-doublet models. *J.Phys. G35* (2008), 075001.

[138] Gunion, John F., and Haber, Howard E. The CP conserving two Higgs doublet model: The Approach to the decoupling limit. *Phys.Rev. D67* (2003), 075019.

[139] Gunion, John F., and Haber, Howard E. Conditions for CP-violation in the general two-Higgs-doublet model. *Phys. Rev. D72* (2005), 095002.

[140] Hall, Lawrence J., Jedamzik, Karsten, March-Russell, John, and West, Stephen M. Freeze-In Production of FIMP Dark Matter. *JHEP 03* (2010), 080.

[141] Hamze, Ali, Kilic, Can, Koeller, Jason, Trendafilova, Cynthia, and Yu, Jiang-Hao. Lepton-Flavored Asymmetric Dark Matter and Interference in Direct Detection. *Phys. Rev. D91*, 3 (2015), 035009.

[142] Harnik, Roni, Martin, Adam, Okui, Takemichi, Primulando, Reinard, and Yu, Felix. Measuring CP violation in $h \to \tau^+\tau^-$ at colliders. *Phys. Rev. D88*, 7 (2013), 076009.

[143] Harris, Philip, Khoze, Valentin V., Spannowsky, Michael, and Williams, Ciaran. Constraining Dark Sectors at Colliders: Beyond the Effective Theory Approach.

[144] Huet, Patrick, and Sather, Eric. Electroweak baryogenesis and standard model CP violation. *Phys.Rev. D51* (1995), 379–394.

[145] Ibarra, Alejandro, and Wild, Sebastian. Dirac dark matter with a charged mediator: a comprehensive one-loop analysis of the direct detection phenomenology. *JCAP 1505*, 05 (2015), 047.

[146] Ilisie, Victor. New Barr-Zee contributions to $(\mathbf{g-2})_\mu$ in two-Higgs-doublet models. *JHEP 04* (2015), 077.

[147] Inoue, Satoru, Ramsey-Musolf, Michael J., and Zhang, Yue. CPV Phenomenology of Flavor Conserving Two Higgs Doublet Models. *Phys.Rev. D89* (2014), 115023.

[148] Iocco, Fabio, Pato, Miguel, and Bertone, Gianfranco. Evidence for dark matter in the inner Milky Way.

[149] Jackiw, R., and Rebbi, C. Vacuum Periodicity in a Yang-Mills Quantum Theory. *Phys. Rev. Lett. 37* (1976), 172–175.

[150] Jacques, Thomas, and Nordstrm, Karl. Mapping monojet constraints onto Simplified Dark Matter Models.

[151] Jarlskog, C. Commutator of the Quark Mass Matrices in the Standard Electroweak Model and a Measure of Maximal CP Violation. *Phys.Rev.Lett. 55* (1985), 1039.

[152] Joyce, M., Prokopec, T., and Turok, N. Constraints and transport in electroweak baryogenesis. *Phys. Lett. B339* (1994), 312–316.

[153] Joyce, Michael. Electroweak Baryogenesis and the Expansion Rate of the Universe. *Phys. Rev. D55* (1997), 1875–1878.

[154] Joyce, Michael, and Prokopec, Tomislav. Turning around the sphaleron bound: Electroweak baryogenesis in an alternative postinflationary cosmology. *Phys. Rev. D57* (1998), 6022–6049.

[155] Joyce, Michael, Prokopec, Tomislav, and Turok, Neil. Electroweak baryogenesis from a classical force. *Phys. Rev. Lett. 75* (1995), 1695–1698. [Erratum: Phys. Rev. Lett.75,3375(1995)].

[156] Joyce, Michael, Prokopec, Tomislav, and Turok, Neil. Nonlocal electroweak baryogenesis. Part 1: Thin wall regime. *Phys. Rev. D53* (1996), 2930–2957.

[157] Joyce, Michael, Prokopec, Tomislav, and Turok, Neil. Nonlocal electroweak baryogenesis. Part 2: The Classical regime. *Phys. Rev. D53* (1996), 2958–2980.

[158] Kajantie, K., Laine, M., Rummukainen, K., and Shaposhnikov, Mikhail E. The Electroweak phase transition: A Nonperturbative analysis. *Nucl. Phys. B466* (1996), 189–258.

[159] Kaplan, David E., Luty, Markus A., and Zurek, Kathryn M. Asymmetric Dark Matter. *Phys.Rev. D79* (2009), 115016.

[160] Keldysh, L. V. Diagram technique for nonequilibrium processes. *Zh. Eksp. Teor. Fiz. 47* (1964), 1515–1527. [Sov. Phys. JETP20,1018(1965)].

[161] Khachatryan, Vardan, et al. Observation of the diphoton decay of the Higgs boson and measurement of its properties. *Eur. Phys. J. C74*, 10 (2014), 3076.

[162] Khachatryan, Vardan, et al. Search for dark matter, extra dimensions, and unparticles in monojet events in proton-proton collisions at $\sqrt{s} = 8$ TeV.

[163] Khachatryan, Vardan, et al. Search for Lepton-Flavour-Violating Decays of the Higgs Boson. *Phys. Lett. B749* (2015), 337–362.

[164] Khater, Wafaa, and Osland, Per. CP violation in top quark production at the LHC and two Higgs doublet models. *Nucl.Phys. B661* (2003), 209–234.

[165] Kile, Jennifer. Flavored Dark Matter: A Review. *Mod. Phys. Lett. A28* (2013), 1330031.

[166] Kile, Jennifer, and Soni, Amarjit. Flavored Dark Matter in Direct Detection Experiments and at LHC. *Phys. Rev. D84* (2011), 035016.

[167] Kilic, Can, Klimek, Matthew D., and Yu, Jiang-Hao. Signatures of Top Flavored Dark Matter. *Phys. Rev. D91*, 5 (2015), 054036.

[168] Klinkhamer, Frans R., and Manton, N. S. A Saddle Point Solution in the Weinberg-Salam Theory. *Phys. Rev. D30* (1984), 2212.

[169] Konstandin, Thomas, Prokopec, Tomislav, Schmidt, Michael G., and Seco, Marcos. MSSM electroweak baryogenesis and flavor mixing in transport equations. *Nucl. Phys. B738* (2006), 1–22.

[170] Kumar, Abhishek, and Tulin, Sean. Top-flavored dark matter and the forward-backward asymmetry. *Phys. Rev. D87*, 9 (2013), 095006.

[171] Kuzmin, V. A., Rubakov, V. A., and Shaposhnikov, M. E. On the Anomalous Electroweak Baryon Number Nonconservation in the Early Universe. *Phys. Lett. B155* (1985), 36.

[172] Lee, Benjamin W., and Weinberg, Steven. Cosmological Lower Bound on Heavy Neutrino Masses. *Phys.Rev.Lett. 39* (1977), 165–168.

[173] Lee, Chao-Jung, and Tandean, Jusak. Lepton-Flavored Scalar Dark Matter with Minimal Flavor Violation. *JHEP 04* (2015), 174.

[174] Lee, Christopher, Cirigliano, Vincenzo, and Ramsey-Musolf, Michael J. Resonant relaxation in electroweak baryogenesis. *Phys.Rev. D71* (2005), 075010.

[175] Lee, T. D. A Theory of Spontaneous T Violation. *Phys. Rev. D8* (1973), 1226–1239. [,516(1973)].

[176] Liu, Tao, Ramsey-Musolf, Michael J., and Shu, Jing. Electroweak Beautygenesis: From b → s CP-violation to the Cosmic Baryon Asymmetry. *Phys. Rev. Lett. 108* (2012), 221301.

[177] Lopez-Honorez, Laura, Schwetz, Thomas, and Zupan, Jure. Higgs portal, fermionic dark matter, and a Standard Model like Higgs at 125 GeV. *Phys.Lett. B716* (2012), 179–185.

[178] Lowette, Steven. Search for Dark Matter at CMS.

[179] Mahanthappa, Kalyana T. Multiple production of photons in quantum electrodynamics. *Phys. Rev. 126* (1962), 329–340.

[180] Mahmoudi, F. SuperIso v2.3: A Program for calculating flavor physics observables in Supersymmetry. *Comput.Phys.Commun. 180* (2009), 1579–1613.

[181] Malik, Sarah, McCabe, Christopher, Araujo, Henrique, Belyaev, A., Boehm, Celine, et al. Interplay and Characterization of Dark Matter Searches at Colliders and in Direct Detection Experiments.

[182] Manton, N. S. Topology in the Weinberg-Salam Theory. *Phys. Rev. D28* (1983), 2019.

[183] Manton, N. S., and Sutcliffe, P. *Topological solitons.* Cambridge University Press, 2007.

[184] Megevand, Ariel, and Sanchez, Alejandro D. Velocity of electroweak bubble walls. *Nucl.Phys. B825* (2010), 151–176.

[185] Misiak, Mikolaj, and Steinhauser, Matthias. NNLO QCD corrections to the anti-B X(s) gamma matrix elements using interpolation in m(c). *Nucl.Phys. B764* (2007), 62–82.

[186] Moore, Guy D. Computing the strong sphaleron rate. *Phys.Lett. B412* (1997), 359–370.

[187] Moore, Guy D. Sphaleron rate in the symmetric electroweak phase. *Phys. Rev. D62* (2000), 085011.

[188] Moore, Guy D., and Prokopec, Tomislav. Bubble wall velocity in a first order electroweak phase transition. *Phys. Rev. Lett. 75* (1995), 777–780.

[189] Moore, Guy D., and Prokopec, Tomislav. How fast can the wall move? A Study of the electroweak phase transition dynamics. *Phys. Rev. D52* (1995), 7182–7204.

[190] Moore, Guy D., and Rummukainen, Kari. Classical sphaleron rate on fine lattices. *Phys.Rev. D61* (2000), 105008.

[191] Moreno, J.M., Quiros, M., and Seco, M. Bubbles in the supersymmetric standard model. *Nucl.Phys. B526* (1998), 489–500.

[192] Morrissey, David E., and Ramsey-Musolf, Michael J. Electroweak baryogenesis. *New J.Phys. 14* (2012), 125003.

[193] Olive, K.A., et al. Review of Particle Physics. *Chin.Phys. C38* (2014), 090001.

[194] Paschos, E.A. Diagonal Neutral Currents. *Phys.Rev. D15* (1977), 1966.

[195] Patel, Hiren H., and Ramsey-Musolf, Michael J. Baryon Washout, Electroweak Phase Transition, and Perturbation Theory. *JHEP 07* (2011), 029.

[196] Petraki, Kalliopi, and Volkas, Raymond R. Review of asymmetric dark matter. *Int.J.Mod.Phys. A28* (2013), 1330028.

[197] Prokopec, Tomislav, Schmidt, Michael G., and Weinstock, Steffen. Transport equations for chiral fermions to order h bar and electroweak baryogenesis. Part 1. *Annals Phys. 314* (2004), 208–265.

[198] Prokopec, Tomislav, Schmidt, Michael G., and Weinstock, Steffen. Transport equations for chiral fermions to order h-bar and electroweak baryogenesis. Part II. *Annals Phys. 314* (2004), 267–320.

[199] Rajaraman, Arvind, Shepherd, William, Tait, Tim M.P., and Wijangco, Alexander M. LHC Bounds on Interactions of Dark Matter. *Phys.Rev. D84* (2011), 095013.

[200] Riotto, A. The More relaxed supersymmetric electroweak baryogenesis. *Phys.Rev. D58* (1998), 095009.

[201] Sakharov, A.D. Violation of CP Invariance, c Asymmetry, and Baryon Asymmetry of the Universe. *Pisma Zh.Eksp.Teor.Fiz. 5* (1967), 32–35.

[202] Schmidt, Daniel, Schwetz, Thomas, and Toma, Takashi. Direct Detection of Leptophilic Dark Matter in a Model with Radiative Neutrino Masses. *Phys. Rev. D85* (2012), 073009.

[203] Schneck, K., et al. Dark matter effective field theory scattering in direct detection experiments. *Phys. Rev. D91*, 9 (2015), 092004.

[204] Schwinger, Julian S. Brownian motion of a quantum oscillator. *J. Math. Phys. 2* (1961), 407–432.

[205] Semenov, A. LanHEP - a package for automatic generation of Feynman rules from the Lagrangian. Updated version 3.1.

[206] Semenov, A.V. LanHEP: A Package for automatic generation of Feynman rules in gauge models.

[207] Shaposhnikov, M. E. Possible Appearance of the Baryon Asymmetry of the Universe in an Electroweak Theory. *JETP Lett. 44* (1986), 465–468. [Pisma Zh. Eksp. Teor. Fiz.44,364(1986)].

[208] Shaposhnikov, M. E. Baryon Asymmetry of the Universe in Standard Electroweak Theory. *Nucl. Phys. B287* (1987), 757–775.

[209] Silk, J., et al. *Particle Dark Matter: Observations, Models and Searches.* 2010.

[210] Srednicki, Mark, Watkins, Richard, and Olive, Keith A. Calculations of Relic Densities in the Early Universe. *Nucl.Phys. B310* (1988), 693.

[211] 't Hooft, Gerard. Computation of the Quantum Effects Due to a Four-Dimensional Pseudoparticle. *Phys. Rev. D14* (1976), 3432–3450. [Erratum: Phys. Rev.D18,2199(1978)].

[212] 't Hooft, Gerard. Symmetry Breaking Through Bell-Jackiw Anomalies. *Phys.Rev.Lett. 37* (1976), 8–11.

[213] Tulin, Sean, and Winslow, Peter. Anomalous B meson mixing and baryogenesis. *Phys. Rev. D84* (2011), 034013.

[214] Tye, S. H. Henry, and Wong, Sam S. C. Bloch Wave Function for the Periodic Sphaleron Potential and Unsuppressed Baryon and Lepton Number Violating Processes. *Phys. Rev. D92*, 4 (2015), 045005.

[215] Wahab El Kaffas, Abdul, Osland, Per, and Ogreid, Odd Magne. Constraining the Two-Higgs-Doublet-Model parameter space. *Phys.Rev. D76* (2007), 095001.

[216] Weinberg, Steven. *The quantum theory of fields. Vol. 2: Modern applications.* Cambridge University Press, 2013.

[217] Yu, Zhao-Huan, Bi, Xiao-Jun, Yan, Qi-Shu, and Yin, Peng-Fei. Tau Portal Dark Matter models at the LHC. *Phys. Rev. D91*, 3 (2015), 035008.

[218] Yu, Zhao-Huan, Zheng, Jia-Ming, Bi, Xiao-Jun, Li, Zhibing, Yao, Dao-Xin, et al. Constraining the interaction strength between dark matter and visible matter: II. scalar, vector and spin-3/2 dark matter. *Nucl.Phys. B860* (2012), 115–151.

[219] Zeldovich, Ya. B., Kobzarev, I. Yu., and Okun, L. B. Cosmological Consequences of the Spontaneous Breakdown of Discrete Symmetry. *Zh. Eksp. Teor. Fiz. 67* (1974), 3–11. [Sov. Phys. JETP40,1(1974)].

[220] Zheng, Jia-Ming, Yu, Zhao-Huan, Shao, Jun-Wen, Bi, Xiao-Jun, Li, Zhibing, et al. Constraining the interaction strength between dark matter and visible matter: I. fermionic dark matter. *Nucl.Phys. B854* (2012), 350–374.

[221] Zurek, Kathryn M. Asymmetric Dark Matter: Theories, Signatures, and Constraints. *Phys.Rept. 537* (2014), 91–121.